

FILTRATION EFFICIENCY MEASUREMENTS ON
FLAT SHEET FILTERS

By

SACHIN ANAND

Bachelor of Engineering

Delhi College of Engineering

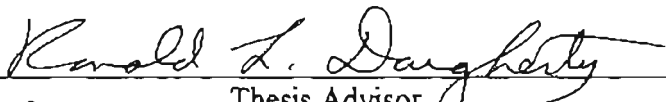
Delhi, India

1994

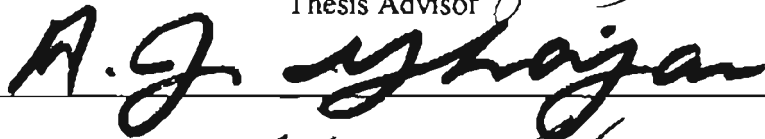
Submitted to the faculty of the
Graduate College of the
Oklahoma State University
in partial fulfillment of
the requirements for
the Degree of
MASTER OF SCIENCE
May, 1997

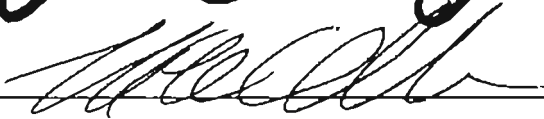
FILTRATION EFFICIENCY MEASUREMENTS ON
FLAT SHEET FILTERS

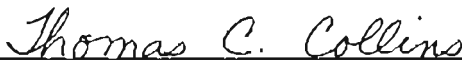
Thesis Approved:



Thesis Advisor







Dean of the Graduate College

ACKNOWLEDGMENTS

I would like to express my sincere appreciation to my major advisor Dr. R. L. Dougherty for his continued guidance, advice and encouragement during the course of this study and throughout my two years as a graduate student at the Oklahoma State University. My sincere appreciation extends to my other committee members Dr. F. W. Chambers and Dr. A. J. Ghajar for their valuable suggestions and help.

A special appreciation is due to my colleague, F. M. Jadbabaei for his support and cooperation. Our team effort gave me an opportunity to learn more during the course of this study. I would like to offer my sincere thanks to my other colleagues, S. H. Yao, Wayne Gimlin and A. Al-Sarkhi for their help and cooperation. I would also like to show my sincere appreciation to James Davis and the other MAE North Lab personnel for their help and cooperation.

I would like to give my special appreciation to my parents Sharda and Vijay Kumar Anand for their support and encouragement throughout my life and especially during the course of my college education.

Finally, I extend my gratitude to Purolator Products, Inc., and the Oklahoma Center for the Advancement of Science and Technology (OCAST) for financially supporting this study.

TABLE OF CONTENTS

Chapter	Page
I. INTRODUCTION.....	1
II. LITERATURE REVIEW.....	4
2.1 Overview	4
2.2 Mechanism of Filtration	5
2.3 Pressure Drop Across Filter Media	11
2.4 Standard Tests	14
2.4.1 SAE J726 Air Cleaner Test Code	16
2.4.2 SAE J1669 Passenger Compartment Air Filter Test Code	18
2.4.3 ASTM F1215-89 Standard Test	19
2.5 Experimental Studies	20
2.6 Recent Developments	33
2.7 Present Work	40
III. LDV INSTRUMENTATION AND THE FLOW SETUP	41
3.1 Overview	41
3.2 Laser Doppler Velocimetry System	43
3.2.1 Optics of the LDV System	43
3.2.1.1 Factors Influencing the Optical Setup.....	48
3.2.2 Signal Processing Setup	55
3.2.2.1 DSA Parameters	57
3.3 Flow Setup	66
3.3.1 Seeding Mechanism	67
3.3.2 Housing	68
3.3.3 Filter Mounting	73
3.3.4 Flow Generation and Measurement	74
IV. CONSISTENCY MEASUREMENTS	75
4.1 Open Flow Tests	76
4.2 Particle Tests Inside the Housing	80
4.3 Complete Filter Mesh Tests	86

4.3.1 Detailed Experimental Procedure	86
4.3.2 Filter Mesh Results	88
V. RESULTS AND DISCUSSION	92
5.1 Overview	92
5.2 Flat Filter Results	95
5.2.1 Measured Velocities	95
5.2.2 Measured Number Densities	102
5.2.3 Pressure Drop Measurements	106
5.2.4 Filter Efficiency and the Influence of Pressure Drop Change	107
5.3 Stokes Number Analysis	113
5.4 Comparison of Results	115
VI. SUMMARY, CONCLUSIONS AND RECOMMENDATIONS	120
6.1 Summary of Results	120
6.2 Conclusions	122
6.3 Recommendations for Future Work	123
REFERENCES	126
APPENDIXES	131
APPENDIX A - LIST OF EQUIPMENT	132
APPENDIX B - SWEEP VOLUME TECHNIQUE	134
APPENDIX C - TSI FLOW METER CALIBRATION	136
APPENDIX D - OTHER RESULTS	139
APPENDIX E - ERROR ANALYSIS	148
APPENDIX F - PRESSURE DROP AND EFFICIENCY PLOTS	150

LIST OF TABLES

Table		Page
2.1	Summary of Current International Air-Cleaner Test Standards [Ensor et al., 1994]	15
2.2	True Efficiencies for 1 μm Particles [Lee, 1977]	24
2.3	Cabin Filter Tested at 340 m^3/hr , Used in Three Cars under Normal Conditions [Gustavsson, 1996]	35
5.1	Complete Test Results	97
5.2	Stokes Number Analysis	98
5.3	Percentage of Pressure Drop Change for Present Study	113

LIST OF FIGURES

Figure		Page
2.1	Collision and Secondary Mechanisms in Aerosol Filtration [Jaroszczyk and Wake, 1991].	5
2.2	Packing Density versus the Pressure Drop Coefficient [Rodman and Lessmann, 1988].	14
2.3	Historical Development of Particle Sizing and Counting Instruments [Ensor et al., 1994].	16
2.4	Local Efficiency over Filter Face in SAE Housing (204 m ³ /hr, 0.966 μm Particles) [Natarajan, 1995].	18
2.5	Comparison of Theoretical and Experimental Filter Efficiencies as a Function of Particle Size (r_p) for a Dacron Filter with $d_f = 11.3 \mu\text{m}$, $\alpha = 0.0493$ and $U = 3.96 \text{ cm/s}$ [Yeh, 1972].	22
2.6	Comparison of Theoretical and Experimental Filter Efficiencies as a Function of Particle Diameter (d_p) for a Glass Fiber Filter with $d_f = 10 \mu\text{m}$, $\alpha = 0.03$ and $U = 21.34 \text{ cm/s}$ [Yeh, 1972].	22
2.7	True Efficiencies for 1 μm Particles [Lee, 1977].	25
2.8	Performance of Filter Media for 0-10 μm Test Dust [Jaroszczyk et al., 1993].	28
2.9	Dependence of Fractional Efficiency on Flow Rate [Ptak et al., 1994].	28
2.10	Dependence of Fractional Efficiency on Temperature [Ptak et al., 1994].	29
2.11	Dependence of Fractional Efficiency on Humidity [Ptak et al., 1994].	29
2.12	Axial Velocity and Particle Concentration Upstream of the Filter (42.5 m ³ /hr, Diffuser, 0.966 μm Particles) [Williams, 1996].	31

2.13	Axial Velocity Downstream of Filter (42.5 m ³ /hr, Diffuser, 0.966 μm Particles) [Williams, 1996].	31
2.14	Number Density Downstream of Filter (42.5 m ³ /hr, Diffuser, 0.966 μm Particles) [Williams, 1996].	31
2.15	Overall Efficiency Measurements for Pleated Filter over Complete 5 x 7 Grid (Diffuser, 0.966 μm Particles) [Jadbabaei, 1997].	32
2.16	Overall Efficiency Measurements for Pleated Filter Using Three Point Averages (Diffuser, 0.966 μm Particles) [Jadbabaei, 1997].	32
2.17	Schematic of the Performance of a Typical Electret vs. Time [Hseih et al., 1996].	34
2.18	Influence of Loading with Different Dusts on Efficiency [Walker and Ptak, 1996].	35
2.19	Dependence of Pressure Drop on Type of Dust [Walker and Ptak, 1996].	35
2.20	Dependence of Pressure Drop on Type of Dust [Walker and Ptak, 1996].	36
2.21	Pressure Drop vs. Dust Loading for Non-Woven Filters (340 m ³ /hr) [Lee, 1996].	37
2.22	Fractional Efficiencies at Various Dust Loadings (Alaska, 340 m ³ /hr) [Lee, 1996].	37
2.23	Fractional Efficiencies at Various Dust Loadings (California, 340 m ³ /hr) [Lee, 1996].	38
2.24	Overall Vehicle Particle Removal Efficiencies on Freeways (Different Blower Settings and Vehicle Speeds) [Lee, 1996].	38
2.25	Typical Pressure Drop vs. Pleat Number Curve [Chen et al., 1996].	39
3.1	Measurement Grid over the Filter.	42
3.2	Schematic of the Laser Doppler Velocimetry System.	44
3.3	A Typical Laser Doppler Signal.	46

3.4	Mounting Base for the Optical Setup.	48
3.5	Influence of Temperature on Beam Power (Green Unshifted Beam).	52
3.6	Beam Power Variation at Constant Temperature.	53
3.7	Minimum Polarized Beam Intensity Variation.	55
3.8	Sample Oscilloscope Screen.	57
3.9	Influence of High Voltage on Data Acquisition.	61
3.10	Influence of Threshold on Data Acquisition.	62
3.11	Flow Setup for the Small Angle Diffuser Housing.	66
3.12	Schematic Assembly of Housing	70
3.13	Small Angle Diffuser Housing.	71
3.14	Schematic of SAE J726 Housing.	72
3.15	Filter Mounting Setup.	73
4.1	Particle Number Density at Center of Housing as a Function of Laser Power [Williams, 1996].	76
4.2	Atomizer Consistency as a Function of Laser Power (Open Flow).	78
4.3	Influence of Nominal Laser Power on Sample Rate (Open Flow).	78
4.4	Influence of Nominal Laser Power on Validity (Open Flow).	79
4.5	Consistency as a Function of High Voltage (Open Flow).	79
4.6	Consistency as a Function of Threshold (Open Flow).	80
4.7	Consistency as a Function of Laser Power (Inside Housing).	81
4.8	Consistency as a Function of High Voltage (Inside Housing).	82
4.9	Consistency as a Function of Threshold (Inside Housing).	82
4.10	Time Consistency Measurement (Inside Housing).	83

4.11	Filtration Efficiency at Center Line for No Filter (Worst Case).	84
4.12	Filtration Efficiency at Center Line for No Filter (Best Case).	85
4.13	Number Density for Different Solution Concentrations.	85
4.14	Local Efficiency Plot with No Filter (Test MESH32).	89
4.15	Local Upstream Number Density Plot with No Filter (Test MESH32).	89
4.16	Local Downstream Number Density Plot with No Filter (Test MESH32).	90
4.17	Local Efficiency Plot with No Filter (Test MESH33).	90
4.18	Local Upstream Number Density Plot with No Filter (Test MESH33).	91
4.19	Local Downstream Number Density Plot with No Filter (Test MESH33).	91
5.1	Grid Points on the Filter with the Measurement Grid Sequence.	93
5.2	Local Upstream Velocity for Flat Filter (5.68 m ³ /hr).	99
5.3	Local Upstream Velocity for Flat Filter (21.54 m ³ /hr).	99
5.4	Local Upstream Velocity for Flat Filter (92.93 m ³ /hr).	100
5.5	Local Upstream Three-Dimensional Velocity for Flat Filter (92.93 m ³ /hr).	100
5.6	Local Downstream Velocity for Flat Filter (5.68 m ³ /hr).	101
5.7	Local Downstream Velocity for Flat Filter (21.54 m ³ /hr).	101
5.8	Local Downstream Velocity for Flat Filter (92.93 m ³ /hr).	102
5.9	Local Upstream Number Densities for Flat Filter (5.68 m ³ /hr).	103
5.10	Local Upstream Number Densities for Flat Filter (21.54 m ³ /hr).	103
5.11	Local Upstream Number Densities for Flat Filter (92.93 m ³ /hr).	104
5.12	Local Downstream Number Densities for Flat Filter (5.68 m ³ /hr).	104
5.13	Local Downstream Number Densities for Flat Filter (21.54 m ³ /hr).	105
5.14	Local Downstream Number Densities for Flat Filter (92.93 m ³ /hr).	105

5.15	Pressure Drop Variation with Flow Rate.	107
5.16	Local Efficiency for Flat Filter (5.68 m ³ /hr).	108
5.17	Local Efficiency for Flat Filter (21.54 m ³ /hr).	108
5.18	Local Efficiency for Flat Filter (92.93 m ³ /hr).	109
5.19	Overall Efficiency versus Flow Rate.	112
5.20	Overall Efficiency versus Stokes Number.	114
5.21	Comparison of Present Data with the Data of Williams [1996] and the Theory of Duran [1995].	115
5.22	Comparison of Present Data with Lee [1977].	116
5.23	Comparison of Present Data with Pleated Filter Results of Jadbabaei [1997].	118
6.1	Possible Housing Design for Efficiency Measurements.	125
B-1	Swept Volume Technique [Liang, 1997].	135
C-1	Results of the TSI Flow Meter Calibration.	138
D-1	Local Upstream Velocity (2.51 m ³ /hr, FLT22)	140
D-2	Local Upstream Velocity (5.68 m ³ /hr, FLT16)	140
D-3	Local Upstream Velocity (13.61 m ³ /hr, FLT14)	140
D-4	Local Upstream Velocity (13.61 m ³ /hr, FLT15)	140
D-5	Local Upstream Velocity (21.54 m ³ /hr, FLT18)	140
D-6	Local Upstream Velocity (21.54 m ³ /hr, FLT20 and FLT21)	140
D-7	Local Upstream Velocity (29.48 m ³ /hr, FLT02)	140
D-8	Local Upstream Velocity (29.48 m ³ /hr, FLT03)	140
D-9	Local Upstream Velocity (45.34 m ³ /hr, FLT11)	140

D-10	Local Upstream Velocity (45.34 m ³ /hr, FLT12 and FLT13)	141
D-11	Local Upstream Velocity (61.20 m ³ /hr, FLT04)	141
D-12	Local Upstream Velocity (61.20 m ³ /hr, FLT05)	141
D-13	Local Upstream Velocity (92.93 m ³ /hr, FLT10)	141
D-14	Local Downstream Velocity (2.51 m ³ /hr, FLT22)	141
D-15	Local Downstream Velocity (5.68 m ³ /hr, FLT16)	141
D-16	Local Downstream Velocity (13.61 m ³ /hr, FLT14)	141
D-17	Local Downstream Velocity (13.61 m ³ /hr, FLT15)	141
D-18	Local Downstream Velocity (21.54 m ³ /hr, FLT18)	141
D-19	Local Downstream Velocity (21.54 m ³ /hr, FLT20)	142
D-20	Local Downstream Velocity (21.54 m ³ /hr, FLT21).	142
D-21	Local Downstream Velocity (29.48 m ³ /hr, FLT02).	142
D-22	Local Downstream Velocity (29.48 m ³ /hr, FLT03).	142
D-23	Local Downstream Velocity (45.34 m ³ /hr, FLT11).	142
D-24	Local Downstream Velocity (45.34 m ³ /hr, FLT12).	142
D-25	Local Downstream Velocity (45.34 m ³ /hr, FLT13).	142
D-26	Local Downstream Velocity (61.20 m ³ /hr, FLT04).	142
D-27	Local Downstream Velocity (61.20 m ³ /hr, FLT05).	142
D-28	Local Downstream Velocity (92.93 m ³ /hr, FLT10).	143
D-29	Local Upstream Number Density (2.51 m ³ /hr, FLT22).	143
D-30	Local Upstream Number Density (5.68 m ³ /hr, FLT16).	143
D-31	Local Upstream Number Density (13.61 m ³ /hr, FLT14).	143
D-32	Local Upstream Number Density (13.61 m ³ /hr, FLT15).	143

D-33	Local Upstream Number Density (21.54 m ³ /hr, FLT18).	143
D-34	Local Upstream Number Density (21.54 m ³ /hr, FLT20 and FLT21).	143
D-35	Local Upstream Number Density (29.48 m ³ /hr, FLT02).	143
D-36	Local Upstream Number Density (29.48 m ³ /hr, FLT03).	143
D-37	Local Upstream Number Density (45.34 m ³ /hr, FLT11).	144
D-38	Local Upstream Number Density (45.34 m ³ /hr, FLT12 and FLT13).	144
D-39	Local Upstream Number Density (61.20 m ³ /hr, FLT04).	144
D-40	Local Upstream Number Density (61.20 m ³ /hr, FLT05).	144
D-41	Local Upstream Number Density (92.93 m ³ /hr, FLT10).	144
D-42	Local Downstream Number Density (2.51 m ³ /hr, FLT22).	144
D-43	Local Downstream Number Density (5.68 m ³ /hr, FLT16).	144
D-44	Local Downstream Number Density (13.61 m ³ /hr, FLT14).	144
D-45	Local Downstream Number Density (13.61 m ³ /hr, FLT15).	144
D-46	Local Downstream Number Density (21.54 m ³ /hr, FLT18).	145
D-47	Local Downstream Number Density (21.54 m ³ /hr, FLT20).	145
D-48	Local Downstream Number Density (21.54 m ³ /hr, FLT21).	145
D-49	Local Downstream Number Density (29.48 m ³ /hr, FLT02).	145
D-50	Local Downstream Number Density (29.48 m ³ /hr, FLT03).	145
D-51	Local Downstream Number Density (45.34 m ³ /hr, FLT11).	145
D-52	Local Downstream Number Density (45.34 m ³ /hr, FLT12).	145
D-53	Local Downstream Number Density (45.34 m ³ /hr, FLT13).	145
D-54	Local Downstream Number Density (61.20 m ³ /hr, FLT04).	145

D-55	Local Downstream Number Density (61.20 m ³ /hr, FLT05).	146
D-56	Local Downstream Number Density (92.93 m ³ /hr, FLT10).	146
D-57	Local Filtration Efficiency (2.51 m ³ /hr, FLT22).	146
D-58	Local Filtration Efficiency (5.68 m ³ /hr, FLT16).	146
D-59	Local Filtration Efficiency (13.61 m ³ /hr, FLT14).	146
D-60	Local Filtration Efficiency (13.61 m ³ /hr, FLT15).	146
D-61	Local Filtration Efficiency (21.54 m ³ /hr, FLT18).	146
D-62	Local Filtration Efficiency (21.54 m ³ /hr, FLT20).	146
D-63	Local Filtration Efficiency (21.54 m ³ /hr, FLT21).	146
D-64	Local Filtration Efficiency (29.48 m ³ /hr, FLT02).	147
D-65	Local Filtration Efficiency (29.48 m ³ /hr, FLT03).	147
D-66	Local Filtration Efficiency (45.34 m ³ /hr, FLT11).	147
D-67	Local Filtration Efficiency (45.34 m ³ /hr, FLT12).	147
D-68	Local Filtration Efficiency (45.34 m ³ /hr, FLT13).	147
D-69	Local Filtration Efficiency (61.20 m ³ /hr, FLT04).	147
D-70	Local Filtration Efficiency (61.20 m ³ /hr, FLT05).	147
D-71	Local Filtration Efficiency (92.93 m ³ /hr, FLT10).	147
F-1	Comparison of Pressure Drop with Tebbutt [1995].	151
F-2	Local Efficiency vs. Local Velocity Plot.	152

NOMENCLATURE

A	cross-sectional area of the probe volume (m^2)
A_2	throat area of nozzle (m^2)
B_{o1}	permeability of a clean filter (m^2)
B_{o2}	permeability of dust cake (m^2)
c	dust concentration (kg/m^3)
C	Cunningham slip correction factor
C_d	discharge coefficient for flow nozzle
d_f	diameter of fiber (m)
d_p	diameter of particle (m)
D_i	particle diffusivity (seconds)
e_u, e_d	variations in upstream and downstream number densities (m^{-3})
E	overall collision efficiency for a filter
E_C	single fiber efficiency due to interception
E_D	single fiber efficiency due to diffusion
E_G	single fiber efficiency due to gravitational forces
E_I	single fiber efficiency due to inertial impaction
g	acceleration due to gravity (m/s^2)
k	Kuwabara hydrodynamic factor

L	filter thickness (m)
L_s	swept volume length (m)
\dot{m}_{ideal}	ideal mass flow rate (kg/s)
n_i	particle number density at grid location i (m^{-3})
n	particle number density (m^{-3})
n_u, n_d	upstream and downstream number densities (m^{-3})
N_i	number of particles counted at grid location i
$N_{Q,q}$	dimensionless parameter for Coulombic forces
p_t	total pressure (Pa)
p_2	throat static pressure (Pa)
Pe	Peclet's number ($=U D_i/d_p$)
Q	flow rate (m^3/hr or cfm)
Q'	charge on a fiber per unit length (Coulomb/m)
q	charge on a particle (Coulomb)
r_p, R_p	particle radius (m)
R	gas constant (J/kg K)
Re	Reynolds number ($=\frac{\rho U d_p}{\mu}$)
R_f	radius of fiber (m)
R_{nd}	ratio of downstream to upstream number density
St	Stokes number ($=\frac{C \rho_p d_p^2 U}{18 \mu d_f}$)
t	time (seconds)

t_i	run time (seconds)
t_{sol}	time taken for consumption of particle solution (seconds)
T_t	total temperature (Kelvin)
u	measured upstream velocity (m/s)
u_o	velocity near filter pleats (m/s)
u_∞	velocity inside filter media (m/s)
U	average flow velocity (m/s)
v_i	local average measured velocity (m/s)
V	velocity of particle (m/s)
V_{at}	volume of solution used from atomizer (ml)
X	axis along the center-line of the transceiver
Y	axis perpendicular to the center-line of the transceiver
Z	vertical axis along the center-line of the housing
α	filter solidity or packing density (= volume of fibers/total volume of filter)
β	porosity of filter media
ε	dust cake porosity
γ	ratio of specific heats
Δp	total pressure drop across a filter (mm of water or Pa)
Δp_1	pressure drop across a clean filter (mm of water or Pa)
Δp_2	change in pressure drop across a filter due to deposition (mm of water or Pa)

- η_1, η_2 independent collection efficiencies
- η overall collision efficiency
- η_e elemental efficiency
- η_i local efficiency
- η_{overall} overall efficiency averaged over all of the grid points
- η_s single fiber efficiency
- λ wavelength of light (m)
- μ dynamic viscosity of air (Pa s)
- ϕ separation efficiency of clean filter
- ρ density of air (kg/m^3)
- ρ_p density of seeding particles (kg/m^3)

CHAPTER I

INTRODUCTION

Air filters find a variety of applications in the industry. One of their oldest uses is in the intake stream of combustion engines. Recently, they have also been used as cabin air filters in automobiles to control air quality inside a vehicle cabin. This study was aimed at investigating the characteristics of the non-woven type filter media used in the manufacture of pleated type automotive air filters.

The function of an intake air filter, or for that matter any air filter, is to remove the particulate contaminants and sometimes odors from the air stream. This allows for enhanced engine performance by reducing engine wear and improving efficiency. This improvement in air quality comes at a price, which is the flow restriction caused by the presence of the filter in the intake stream. The flow restriction or pressure drop assumes significance when the filter becomes loaded with contaminants. This study also examined these pressure drop changes over the initial life of the filter and their impact on the efficiency of the filter.

Efficiency measurements on air filters are done using various methods. Earlier methods were based on gravimetric measurements of the filter before and after the test. This was used to determine the contaminant retained by the filter and hence, its efficiency. Recently, optical particle counters have been employed to measure particle concentrations

in the test aerosols. The study described herein involved the use of a Laser Doppler Velocimetry based optical setup coupled to a micro-computer based digital data acquisition system. This method enables the measurement of filter efficiencies in local regions of the filter rather than a composite 'overall efficiency' obtained in most of the earlier studies. Overall efficiency values give no indication of the actual efficiency distribution over a filter face. Local measurements can prove useful for filter housing design in automobiles. Improved designs could mean more uniform use of the filter area thereby increasing filter life.

The reliability of the experimental results presented herein would remain questionable until certain tests were conducted on the setup to prove their reliability and consistency. Earlier studies using the current setup had experienced difficulties in test repeatability. The author conducted an investigation into the factors, both external and internal, affecting the acquisition of data as a part of this study. Some improvements were made in the setup, followed by tests to check data consistency, before the actual data was collected.

Flow velocity over the filter face has a big impact on the efficiency values as shown by numerous theoretical and experimental studies in the past. Most automotive filters in current use are of the pleated type. The average flow velocity at the filter media surface is calculated by evenly distributing the flow over the entire surface of the unfolded filter. This assumption is then used for predicting the filtration efficiency of pleated filters. The author aimed to measure filter efficiencies for a wide range of flow rates for flat filter media and compare them with efficiencies for pleated filters (made from the same

material) determined by other researchers. This would allow for the development of a correlation for the efficiency values of flat and pleated filter media for a range of flow rates (or Stokes Number).

The filter efficiency test is carried out in a housing specified under the SAE J726 code [SAE, 1987]. This housing has been shown to have re-circulation zones [Natarajan, 1995] along its edges causing an uneven velocity profile over the filter face which sometimes results in negative efficiency values. To obtain a uniform velocity profile over the filter face, the measurements were carried out in a 'small angle diffuser' housing similar to that specified in the SAE J1669 cabin air filtration code [SAE, 1993]. Most computational modeling for filter efficiency prediction has been done with the assumption of a uniform flow field [Lee et al., 1982b]. Therefore, the author's experimental results can be compared with computational predictions.

CHAPTER II

LITERATURE REVIEW

2.1 Overview

The main aim of this study was to investigate the filtration characteristics of flat sheet filter media used in the manufacture of pleated automotive filters, specifically the A13192 Purolator filter, and determine a correlation for filtration efficiency between flat media and pleated media. The most important aspect of this correlation is the comparison of filter face velocities, i.e., to determine the relationship between effective face velocities for flat media and pleated media that yield the same filtration efficiency. Currently, face velocities for pleated filters are estimated by distributing the flow over the open filter, but the author will show in later sections of this report that the relationship is more complex.

This literature review will attempt to review past work in the related fields of filtration. First, a brief description of the theoretical aspects of filtration will be provided to better understand the mechanisms of filtration. This will also include a review of the concept of pressure drop across a filter and its significance in filtration. Next a review of the existing standardized tests like the SAE J726 and the ASTM standards will be performed. Finally, the actual experimental research in the area of filtration will be targeted. The majority of the literature in this area can be subdivided into two broad categories - research involving the use of aerosols along with particle counting devices,

and research involving the use of actual (standardized) test dusts to obtain filtration efficiencies. Both of these categories will be examined by the author.

2.2 Mechanism of Filtration

Collection of particles by filters is due to two processes - collision and adhesion [Jaroszcyk, et al., 1993a]. Collision for a single fiber is the sum of six basic filtration mechanisms shown in Fig. 2.1 [Jaroszcyk and Wake, 1991]. Classical filtration theory is based on simplifying the filter geometry and accounting for various particle collision mechanisms for a single fiber. The basic mechanisms include sieving (not shown in Fig. 2.1), diffusive deposition, interception, inertial impaction, gravitational settling and electrostatic attraction or repulsion.

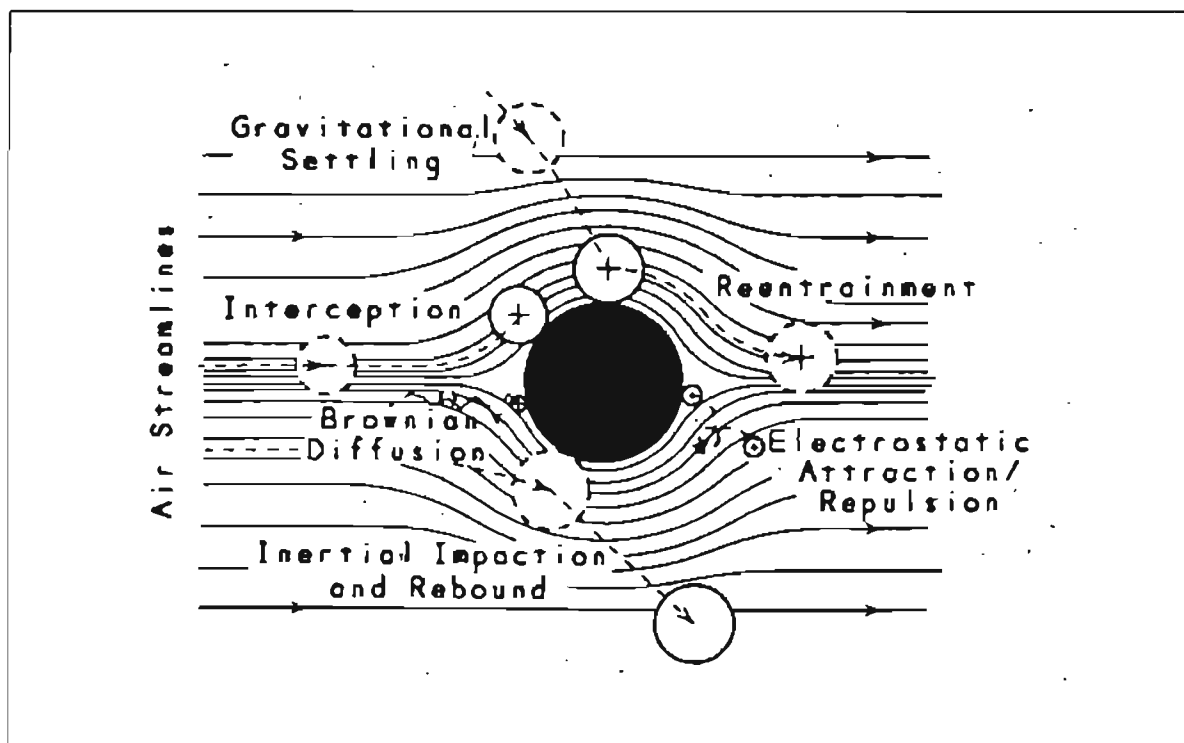


Figure 2.1 Collision and Secondary Mechanisms in Aerosol Filtration [Jaroszcyk and Wake, 1991].

Sieving involves trapping of particles in the void spaces between the fibers in the filter and requires particle dimensions to be greater than the void dimensions. This is not the principle mode of filtration, as in most cases, the particle diameter is smaller than the void space in size.

Diffusive deposition of aerosols on fibers occurs when Brownian diffusion of the particles will bring them in contact with the fiber. Diffusion is more important when particle sizes are small and flow rates are low. Brownian diffusion of particles decreases with an increase in size while an increase in flow velocity reduces the time of residence of the particle in the filter medium [Jaroszczyk and Wake, 1991]. Both of these reduce the probability of the particle reaching the filter fibers, thereby preventing capture by diffusion. A mathematical equation predicting the single fiber efficiency due to diffusion has been developed by Lee and Liu [1982] as

$$E_D = 2.6 \left(\frac{1-\alpha}{k} \right)^{\frac{1}{3}} Pe^{-\frac{2}{3}} \quad (2-1)$$

where α is the filter solidity (ratio of volume of fibers to total volume)

k is Kuwabara's hydrodynamic factor $\left(= -\frac{1}{2} \ln \alpha - \frac{3}{4} + \alpha - \frac{1}{4} \alpha^2 \right)$

Pe is Peclet Number $\left(= \frac{UD_i}{d_p} \right)$

U is the free stream flow velocity towards the fiber

D_i is the particle diffusivity

d_p is the particle diameter

Interception or direct capture of particles takes place when a particle in the flow field around a fiber is at a distance of at most $d_p/2$ from the fiber. Interception assumes

massless particles having only size. This causes the particles to attach to the fiber and interception occurs. The single fiber efficiency due to interception as given by Lee and Liu [1982] is

$$E_c = \frac{1 - \alpha}{k} \frac{\left(\frac{d_p}{d_f}\right)^2}{1 + \frac{d_p}{d_f}} \quad (2-2)$$

where d_f is the fiber diameter and the other symbols are the same as Eq. (2-1). The larger the particle diameter, the greater is its probability of coming within a distance of $d_p/2$ of the fiber. Thus, E_c increases with increasing particle size. The flow field determines the streamline followed by the particle around the fiber and hence, its probability of coming in contact with the fiber.

Inertial impaction is a direct result of the inertia of the particle which causes it to deviate from the streamlines of the flow and finally strike the fiber, getting deposited on it. It depends on the Stokes number (St) which is a non-dimensional number reflecting the measure of the kinetic energy of the particle ratioed to the work done against viscous drag. Inertia involves both size and velocity. The inertial impaction efficiency as reported by Jaroszczyk and Wake [1991] is

$$E_I = \frac{St^3}{St^3 + 0.77 St^2 + 0.22} \quad (2-3)$$

This is an empirical relation obtained by Landhal and Herman [1949] for $Re = 10$. Davies [1973] suggests that a minimum value of Stokes number is required for inertial impaction to occur and various researchers have tried to obtain this value. Stokes number has been defined in two ways in the literature. Stenhouse [1975], McLaughlin et al. [1986] and Yeh and Liu [1974] define Stokes number as

$$St = \frac{C \rho_p d_p^2 U}{9\mu d_f} \quad (2-4)$$

where C is the Cunningham slip correction factor (=1 for $d_p > 1 \mu\text{m}$), μ is the air dynamic viscosity, ρ_p is the particle density and the other symbols are as defined in the previous equations. Liang et al. [1994] and Jaroszczyk and Wake [1991] replace the 9 with an 18 in Eq. (2-4). The author is unable to explain the reason for this difference; however, a derivation of the Stokes number from first principles [Brown, 1993] confirms the value of 18 in Eq. (2-4). The basic equation for this derivation is

$$m \frac{dV}{dt} = -3\pi\mu d_p V \quad (2-5)$$

where m is the mass of the particle, V is the velocity of the particle at time t and the other symbols are as defined previously.

Gravitational forces take part in filtration of large particles at low velocities (not typically found in automotive filtration examined in this study). An expression reported by Jaroszczyk and Wake [1991] is

$$E_G = K_2 \frac{1}{U} \frac{d_p^2 g \rho_p}{18\mu} \quad (2-6)$$

where K_2 is a constant and g is the acceleration due to gravity.

Particles and fibers often carry electrostatic charge [Davies, 1973] which may play a role in filtration. Particles may be attracted to (or repulsed by) the fiber surface from a distance or “stick” (attach) to the fiber surface due to electrical charges on them or on the fiber surface. The dimensionless parameter describing Coulombic forces is given as [Davies, 1973]

$$N_{Q,q} = \frac{4Q'q}{3\pi\mu d_p d_f U} \quad (2-7)$$

where, Q' and q are the charge on the fiber per unit length and the charge on the particle respectively. Depending on whether the charge is on the fiber or the particle, a number of expressions for efficiency have been reported by Davies [1973]. Equation (2-7) shows that the efficiency due to this mechanism is directly proportional to the charge and inversely related to the aerosol velocity.

The size ranges in which some of the mechanisms are important are [Davies, 1973]

- Inertial Impaction: $>1 \mu\text{m}$.
- Interception: $>1 \mu\text{m}$.
- Diffusion: $<0.5 \mu\text{m}$.
- Electrostatic Attraction: 0.01 to $5 \mu\text{m}$.

If $\eta_1, \eta_2, \dots, \eta_n$ are the collision efficiencies due to n different mechanisms, then the composite efficiency is given by [Davies, 1973]

$$\eta = 1 - (1 - \eta_1)(1 - \eta_2) \dots (1 - \eta_n) \quad (2-8)$$

Since different mechanisms dominate in different particle size and flow velocity ranges, researchers often take the composite efficiency as the sum of the independent efficiencies due to each of the mechanisms. The overall efficiency for the filter media is calculated from the single fiber efficiency due to all the mechanisms as [Yeh and Liu, 1974]

$$E = 1 - \exp\left[\frac{-4\eta_s \alpha L}{\pi(1-\alpha)d_f}\right] \quad (2-9)$$

where L is the filter thickness, η_s is the single fiber efficiency calculated from Eq. (2-8) and

α is the filter solidity.

Most of the theories assume that any particle coming in contact with a fiber is captured by the fiber, i.e., the retention (or actual filtration) efficiency of the fiber is 1. This is not true in actual practice where, retention efficiency is smaller than collision efficiency (filtration efficiency calculated from Eq. (2-8)) in the inertial region of filtration [Wake and Jaroszczyk, 1991]. A factor called the adhesion probability factor can be estimated for aerosols for idealized test conditions to correct for aerosol adhesion in theory. However, actual field conditions to calculate this are unknown. Adhesion can be divided into three basic mechanisms - adhesion due to van der Waals forces, electrostatic charge and capillary action [Jaroszczyk et al., 1993]. A particle is collected by a filter fiber if its kinetic energy is less than the energy of adhesion. In cases where the particle's kinetic energy is higher, the adhesion probability factor is less than 1 and the particle can bounce off the fiber. Therefore, collision efficiency is modified by the adhesion probability factor to give the collection efficiency of a single fiber (retention efficiency \approx adhesion probability factor \times collision efficiency).

Sabnis [1993] developed a model to calculate the single fiber efficiency and Duran [1993] improved upon it. The model accounted for non-perfect particle adhesion and retention. They used the model for adhesion probability factor developed by Ptak and Jaroszczyk [1990] as

$$\eta_{adh} = \frac{190}{(\text{Re } St)^{0.68} + 190} \quad (2-10)$$

The model also accounted for reentrainment of particles while assuming diffusion mechanisms to be negligible, monodisperse aerosols, uniform fiber diameter, uniform

packing density and a clean filter media.

The single fiber efficiency model of Eq. (2-9) does not take into account the effect of neighboring fibers on each other. To account for this effect, parallel cylinder models were introduced to model fibers in proximity to each other. The most important work in this area was by Kuwabara [1959] which enabled calculation of filtration efficiency and pressure drop by computer simulation. Extensions and improvements on this model have been provided by Yeh and Liu [1974] and McLaughlin et al. [1986].

Another model in this area was the pore theory model [Lessmann, 1986] which modeled the geometry of the filter media more closely than any of the other parallel cylinder models. However, this model idealized the structure with an ordered system of round pores [Rodman and Lessmann, 1988]. A more recent model called the offset screen theory [Rodman and Lessmann, 1988] accounts for the anisotropy of the filter media, the inhomogeneity of the fiber dispersion and an assumption of three-dimensional flow inside the filter media. This complicates the calculation procedure but Rodman and Lessmann [1988] proposed to use the numerical results from this model to obtain simple polynomial expressions (curve fits for the results) which can be used to make the theory conveniently applicable.

2.3 Pressure Drop Across Filter Media

Collection efficiency and pressure drop across a filter are the two most important quantities to describe the properties of the given filtration material [Davies, 1973]. A high pressure drop in a filter media, in spite of a high efficiency, would make any practical use

of the filter impossible. The most basic equation giving the pressure drop across a filter is the Darcy equation which can be written as [Loffler, 1970]

$$\Delta p = \frac{\mu}{B_{o1}} L U \quad (2-11)$$

where B_{o1} is the permeability of the clean filter and the other symbols are as used earlier in this chapter.

The permeability of the filter media changes during the process of filtration due to deposition of particles on the media which results in clogging of the filter pores. The initial filtration is surface type while after deposition depth type filtration due to the dust cake is prevalent. Loffler [1970] defines the pressure drop across a filter at any time t after the beginning of filtration as the sum of the initial pressure drop on a clean filter (Δp_1) and the change in pressure drop during filtration due to deposition (Δp_2). This can be written as

$$\Delta p = \Delta p_1 + \Delta p_2 \quad (2-12)$$

and

$$\Delta p_2 = \frac{\mu}{B_{o2}} \frac{\phi}{\rho_s(1-\varepsilon)} U^2 c t \quad (2-13)$$

where B_{o2} is the permeability of the dust cake and depends on its structure, the particle size and distribution, and the porosity (ε) of the cake. In actual field conditions, it is difficult to estimate this parameter. ϕ is the separation (or filtration) efficiency, c is the dust concentration and ρ_s is the density of the dust. Since the cake structure keeps changing during the process of deposition, B_{o2} is not constant, and hence, Δp_2 cannot be said to have a linear relationship with time. Δp_2 in Eq. (2-12) usually has a higher value than Δp_1 when Reynolds number is greater than approximately 2 to 5 or at velocities

higher than 2 to 3 m/s [Jaroszczyk and Wake, 1991]. Reynolds number is defined as

$$\text{Re} = \frac{U d_p}{\nu} \quad (2-14)$$

where the symbols are as defined earlier.

Another form of Eq. (2-11) was reported by Davies [1973], where the value of B_{o1} was estimated as

$$B_{o1} = d_f^2 \frac{\left(-\frac{1}{2} \ln \beta - C\right)}{16\beta} \quad (2-15)$$

where β is the porosity of the media and $C = 0.75$ for Kuwabara's flow. A comparison of this equation with the experiments of Davies [1973] and others indicated that the experimental values were 20-30% smaller than predictions [Davies, 1973]. Similar observations of comparison of theoretical pressure drop models with experimental data have been made by Rodman and Lessmann [1988]. They [did not give an expression for pressure drop in their paper but] attempted to calculate the pressure drop on the basis of their offset screen theory (mentioned in section 2.2) and their results are shown in Fig. 2.2. Pressure drop coefficient is a non-dimensional number representing pressure drop while packing density is the same as filter solidity. Their results show lower pressure drops than earlier theories but these values are lower than those given by the empirical relationships of Davies [1973] as they did not account for the anisotropy of the media. They point to this anomaly but do not show any changes in their model to correct for it.

Most of these models can predict some values of pressure drops for filter media but are unable to predict its influence on the efficiency of the media. Experimental work in this area has shown some of this dependence and will be reviewed in section 2.5 in this

chapter.

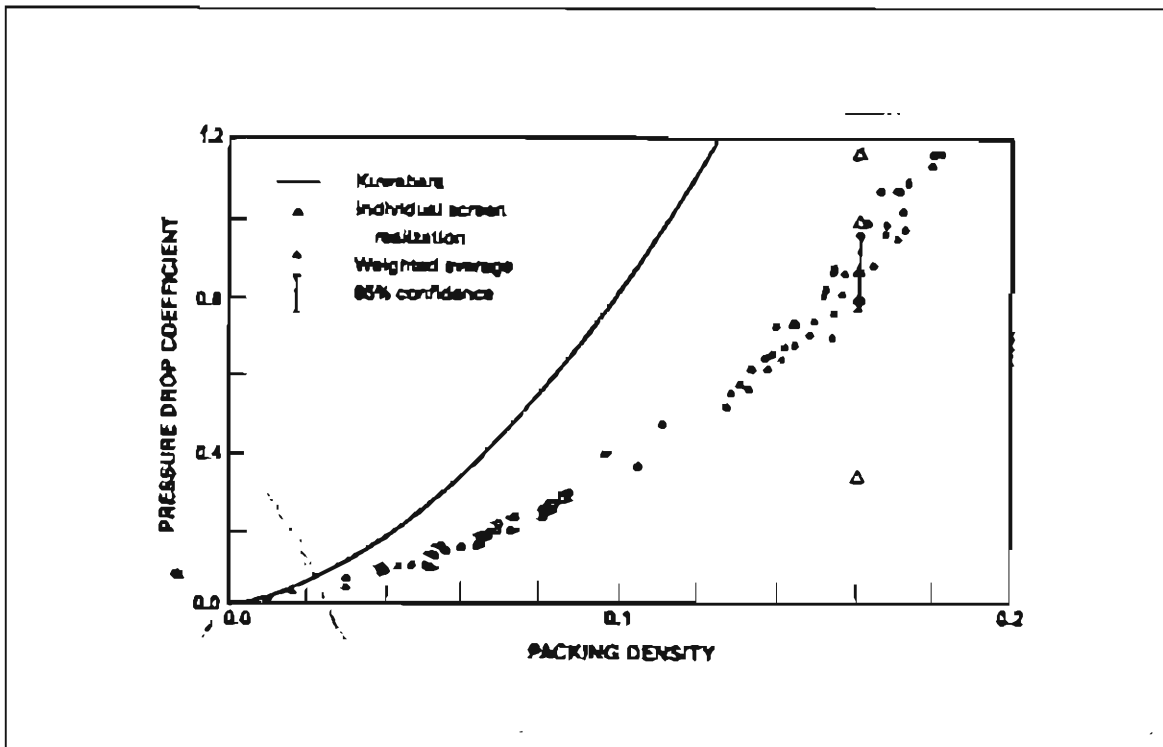


Figure 2.2 Packing Density versus the Pressure Drop Coefficient [Rodman and Lessmann, 1988].

2.4 Standard Tests.

There are a number of standardized tests world-wide to check the performance characteristics of air filters as listed in Table 2.1 [Ensor et al., 1994]. None of these tests is able to provide information regarding all four parameters - pressure drop, dust capacity, effect of dust and size dependent (or fractional) efficiency. The fifth parameter, ozone generation, is typical of cabin or indoor air filters in the HVAC system. Two notable omissions from Table 2.1 are the SAE J1669 cabin air filter test code and the ASTM F1215-89 test for flat sheet filter media. Both of these tests do not predict the effect of dust on the filtration efficiency, i.e. the effect of loading.

Table 2.1 Summary of Current International Air-Cleaner Test Standards [Ensor et al., 1994]

Standard	Pressure drop	Ozone generation	Dust capacity	Effect of dust	Size-dependent filtration efficiency
ASHRAE 52-76	yes	no	yes	yes	no
AHAM AC-1-1988	no	no	no	no	no
IES Rec. Prac. 007	yes	no	no	no	no
ML-STD-282	yes	no	no	no	no
ARI-850-84	yes	yes	yes	yes	no
ARI 680	yes	yes	yes	yes	no
British Standard 2831	yes	no	yes	yes	no
British Standard 4400	no	no	no	no	no
British Standard 3928	no	no	no	no	no
French Standard AFNOR NF44-011	no	no	no	no	no
French Standard AFNOR NF44-013	no	no	no	no	no
European Standard EN 1822-4/5	yes	no	yes	yes	no
Japanese Standard JIS C 9615-1976	no	no	yes	yes	no
Japanese Standard JACA 10C 1979	yes	yes	yes	yes	no
German Standard DIN 24184	yes	no	no	no	no
German Standard DIN 24185	yes	no	yes	yes	no
Australian Standard 1132	yes	no	yes	yes	no
SAE Air Cleaner Elements 1987	yes	no	yes	yes	no

A variety of instruments can be used for particle counting and sizing measurements. A historical development of various instrumentation is shown in Fig. 2.3 [Ensor et al., 1994]. Currently, the most common particle counting instruments are the optical particle counters using laser light scattering. They can make non-intrusive measurements of both particle size and count along with particle (or flow) velocity (LDV based systems). The reliability of any test standard depends on how rapidly the filter efficiency can be determined. Time is critical, as dust loading over time causes a change in filtration efficiency. Also, a fast system can determine the effect of filter loading by making time dependent measurements. The next few sections will give a brief review of the SAE J726, the SAE J1669 and the ASTM F1215-89 test standards.

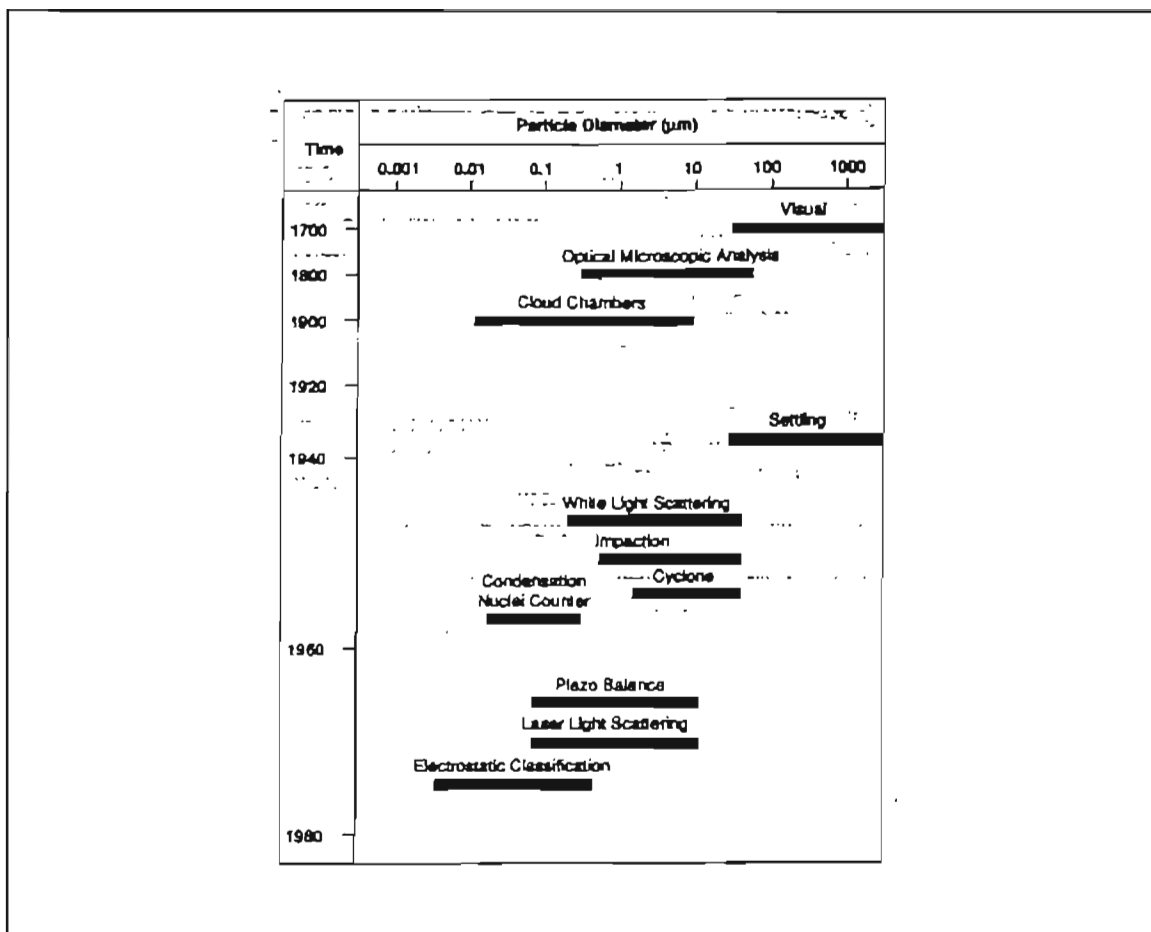


Figure 2.3 Historical Development of Particle Sizing and Counting Instruments [Ensor et al., 1994].

2.4.1 SAE J726 Air Cleaner Test Code

The SAE J726 air cleaner test code, revised last in 1987, provides a uniform means of evaluating automotive intake air filters on bench test equipment. The test determines overall filter efficiency by gravimetric measurements under controlled conditions so that repeatability is high. Controlled conditions include a standard housing, uniform dust dispersion, temperature, pressure, humidity and standardized test dusts. The test also determines dust holding capacity and corresponding pressure drops at the filter

manufacturer's rated flow rate. Typical ranges for air cleaner flow rates, efficiencies and pressure drops measured in this standard [Nicholson and Weisert, 1986] are :

- Air Flow: 0.2 to 300 m³/hr
- Efficiencies: 10 to 99.99%
- Pressure Drop: 100 to 7500 Pa

The test is oriented toward steady state efficiency which is adequate for quality control product specification but inadequate for air cleaner development [Nicholson and Weisert, 1986]. For filter media development and modeling, initial efficiency under conditions of low dust concentration is the primary interest, as it provides critical information about media structure and avoids the unpredictability of particle interaction under heavy loading. These efficiency measurements require on-line sample extraction or non-intrusive measurements to minimize large errors in weighing and handling. A test system using optical particle counters has been developed by the Donaldson Co., Inc. [Nicholson and Weisert, 1986] to evaluate the complete air cleaner system performance. Field testing using this system has allowed environment characterization (particle size, its distribution and concentration), determination of optimum inlet locations and development of a correlation between particle size and specific engine wear.

The SAE J726 test standard is unable to simulate application environments like vibration excitation in use, performance under wet or humid conditions, efficiency with special contaminants (required for certain off-road vehicles), pressure pulsations or flow oscillations and others. Also, the housing used in this test cannot fully evaluate the filter performance [Natarajan, 1995]. Sabnis [1993] and Sabnis et al. [1994] evaluated the

impact of non-uniform flow inside the SAE J726 housing on the filter efficiency measurements using both flow visualization and LDV measurements to compute efficiency. They found the flow close to the housing walls to be strongly recirculating separated flow which would cause the tested filter to experience different flow rates in different regions, far from the uniform design flow rates. The SAE J726 housing has been shown to have re-circulation zones in its upstream flow (due to the large diffuser angle) which present the filter element with a non-uniform flow field and result in low efficiency measurements close to the edges (Fig. 2.4).

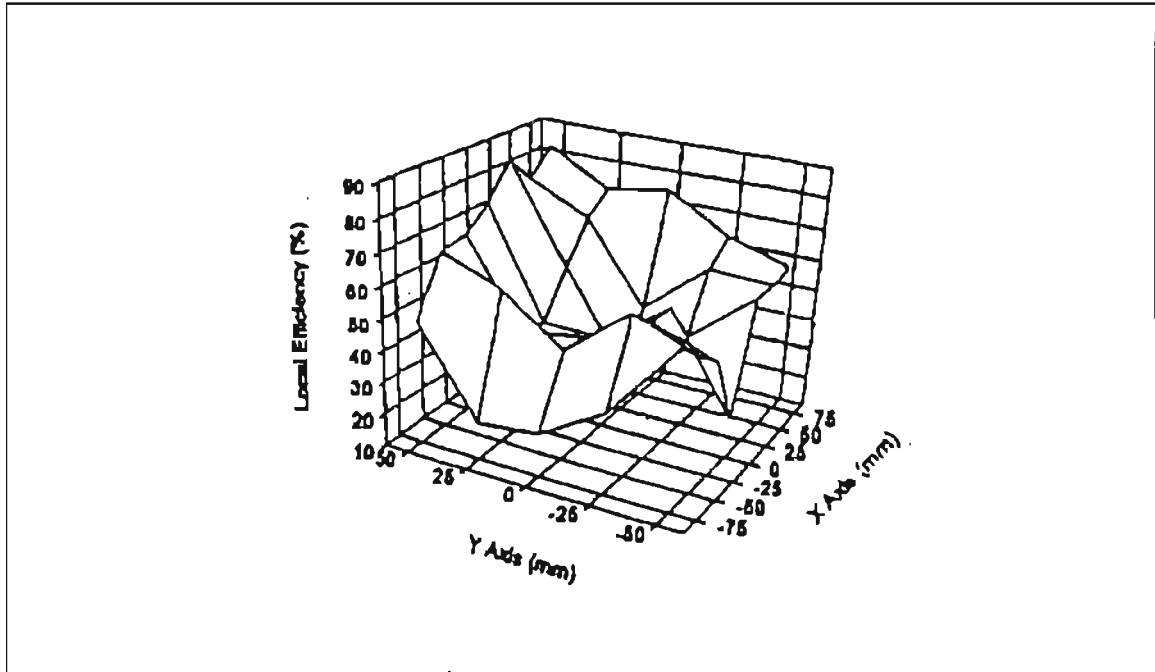


Figure 2.4 Local Efficiency over Filter Face in SAE housing ($204 \text{ m}^3/\text{hr}$, $0.966 \mu\text{m}$ particles) [Natarajan, 1995].

2.4.2 SAE J1669 Passenger Compartment Air Filter Test Code

Although this test is proposed for the cabin air filters, it has been designed keeping

in view the deficiencies of the SAE J726 test code and can be used for other types of filters. Apart from overall efficiency measurement, the test is designed to measure fractional efficiencies, i.e. efficiencies for different particle sizes. This is made possible by the use of sizing instrumentation to accurately size particles. Fractional efficiency tests are done with aerosols other than dust while dust is used for overall efficiency and dust holding capacity tests. The aerosol is also electrically neutralized to eliminate electrical charges which may influence the efficiency measurement. Another important difference in this test from the SAE J726 test is the use of a small angle diffuser having a diffuser angle less than 7° . This allows for the filter to be placed in a uniform flow field as shown by Natarajan [1995] and confirmed by the present study. The setup and many conditions suggested for this test have been incorporated by the author for the present study.

This type of housing was also used by Jadbabaei [1997] for testing pleated automotive intake filters, and the appearance of recirculation zones along the edges of the filter on the downstream side were reported. These were due to the mounting of the filter which caused the rubber edging on the lower side of the filter to reduce the flow area, causing the recirculation zones.

2.4.3 ASTM F1215-89 Standard Test

The ASTM F1215-89 is a standard test method for determining the initial efficiency of a flat sheet filter medium in an air flow using latex spheres. The test is designed for filter media, not filter elements like the SAE J726 and J1669 tests, and is aimed at filter media evaluation and development. It uses optical light scattering to

measure particle counts upstream and downstream in a representative volume over a size range of 0.5 to 5 μm with air flow velocities of 1 to 25 cm/s. Care is taken to neutralize any charge on the aerosol particles.

The biggest source of error in this test can come from the sampling procedure. The test recommends isokinetic sampling (a condition where the velocity of the air flow entering the sampling nozzle is the same as the velocity of the air flow passing around the sampling nozzle) which may not be possible to achieve due to losses in the sampling transport line caused by settling, diffusion and inertia of the particles.

2.5 Experimental Studies

A number of experimental studies are found in the literature and a list of some of the older ones is provided in Yeh [1972]. These attempt to better simulate the actual conditions experienced by air filters. They serve as developmental tools in the process of validating and improving filter design and their theoretical models. Some of these experimental studies will be reviewed next.

Yeh [1972] did an experimental study to compare the results of his theoretical model. Since the theory assumed monodisperse spherical particles and cylinder fibers, the experiments were designed to meet these conditions. A dacron filter with 11.3 μm diameter fibers was used along with DOP (Di-2-Ethylhexyl Phthalate) particles in the size range of 0.327 μm to 1.07 μm . The filter solidity or volume fraction, α , was varied between 0.013 and 0.0851, filter thickness was varied between 0.409 cm and 2.76 cm, and pressure was varied between 0.2 and 1 atmosphere. The aerosol concentration upstream

and downstream of the filter was determined by collecting aerosol samples in glass bottles and using a Sinclair Phoenix Smoke Photometer was used to determine the particle concentrations. The results were converted to single fiber efficiency using Eq. (2-9) and then compared to existing theoretical models. The true filter efficiencies were not plotted for all flow velocities. To prevent the clogging of the filter, the pressure drop was checked frequently; and if it exceeded the starting value by 10%, the filter was replaced with a new one. Therefore, the results reflected clean filter results, an assumption made in theoretical models. The measurement technique of collecting samples in bottles caused some loss of aerosol resulting in an error in the accuracy of the results.

Some of the results and their comparison to theory are shown in Fig. 2.5 and Fig. 2.6 which plot true (not single fiber but actual) filter efficiencies versus particle size for two different flow velocities. The experimental data shows good agreement with the theory. Also, Yeh [1972] used flow velocities in the range of 0.295 to 22 cm/s which are low for any kind of automotive filtration application. The use of very low filter solidities (α) in comparison to those observed in practice also reduces the applicability of these results. These experiments were primarily designed to validate the theory and hence, employed parameters to idealize the filtration process.

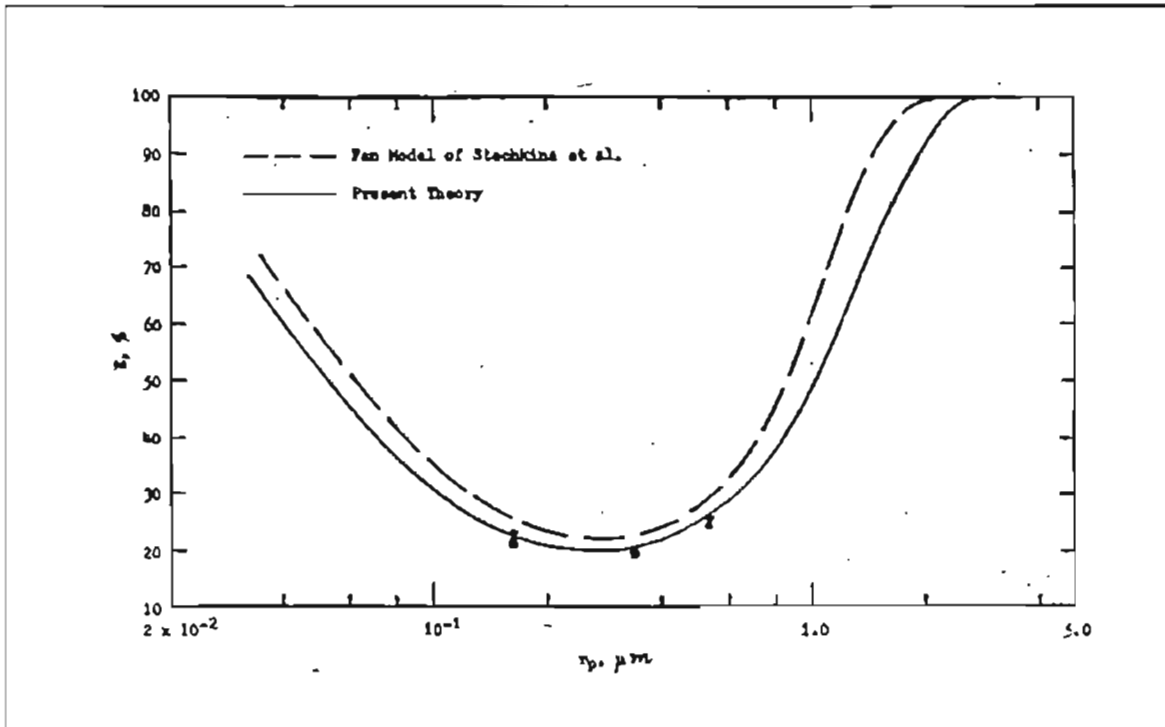


Figure 2.5 Comparison of Theoretical and Experimental Filter Efficiencies as a Function of Particle Size (r_p) for a Dacron Filter with $d_f = 11.3 \mu\text{m}$, $\alpha = 0.0493$ and $U = 3.96 \text{ cm/s}$ [Yeh, 1972].

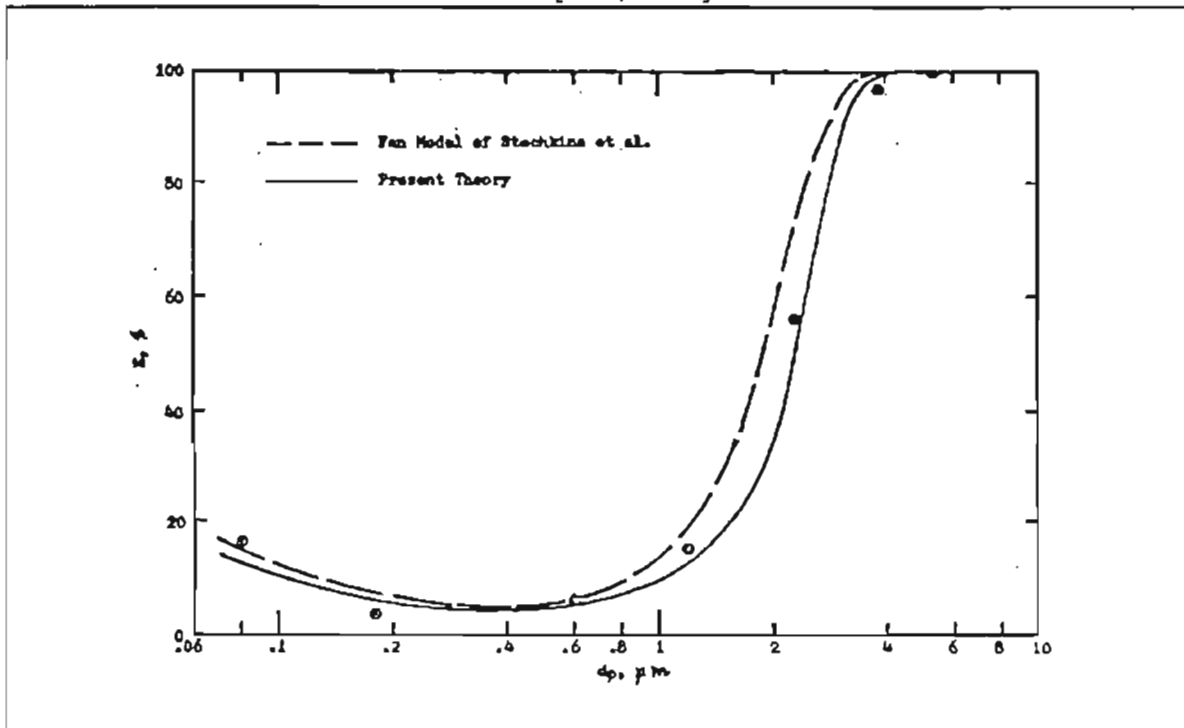


Figure 2.6 Comparison of Theoretical and Experimental Filter Efficiencies as a Function of Particle Diameter (d_p) for a Glass Fiber Filter with $d_f = 10 \mu\text{m}$, $\alpha = 0.03$ and $U = 21.34 \text{ cm/s}$ [Yeh, 1972].

Lee [1977] and Lee and Liu [1982] devised a new filter efficiency measurement technique by developing a new monodisperse aerosol generator and a new aerosol detector allowing for filter efficiency measurement over a wider range of conditions. They also used DOP particles but in the size range of 0.035 to 1.3 μm and varied the flow velocity between 1 and 300 cm/s. They used two types of filters, Dacron A ($d_f = 11.0 \mu\text{m}$) and Dacron B ($d_f = 12.9 \mu\text{m}$) and varied the filter solidity by compressing the filters by applying different pressures to reduce void volume in the filter. The filters were specifically designed for the study and had uniform size fibers which meant that they represented the ideal conditions assumed in theories. Also, the charge on the particles was neutralized by passing the generated aerosol through a tube containing Kr-85 (a radioactive substance).

An electrical aerosol detector was used to make particle concentration measurements upstream and downstream of the filter. The electrical aerosol detector allows measurement of particle concentrations over a wide range of flow rates. The results for these experiments have been presented in the form of plots and tables in Lee [1977]. All of the plots were with single fiber efficiency obtained from the true efficiency by using Eq. (2-9). The author has extracted some of the true efficiency values from Lee [1977] and presented them in Table 2.2 and Fig. 2.7.

For the purpose of comparing data applicable to actual filtration conditions, the author extracted data for higher filter solidities to plot the curves of Fig. 2.7. The curves are for 1 μm particles only, which were used by the author in the present study. The curves of Fig. 2.7 will be used later for comparison with the results obtained in this study.

The variation in flow velocity is representative of the variation in Stokes number (for the same filter) as all other parameters (including particle size) are identical. One can observe that there are two efficiency values for a given flow velocity (or Stokes Number) for the same filter (Dacron B) depending on the filter solidity. This suggests that efficiency is not dependent on Stokes number and filter solidity independently but on both in a more complex and composite manner.

Table 2.2 True Efficiencies for 1 μm Particles [Lee, 1977]

Filter Type	Filter Solidity (α)	Face Velocity (cm/s)	Filter Efficiency (%)
Dacron A	0.299	1	72.9
		3	60.3
		10	59.1
		30	77.3
Dacron B	0.271	1	26.4
		3	18.6
		10	23.1
		30	38.1
		100	85.0
		300	96.5
Dacron B	0.421	1	52.2
		3	50.3
		10	68.2
		30	86.7
		100	99.1
		300	98.9

Stokes Number Variation: Dacron A: 1 cm/s \rightarrow 0.00277 and 1000 cm/s \rightarrow 2.77
(Author's Definition) Dacron B: 1 cm/s \rightarrow 0.00236 and 1000 cm/s \rightarrow 2.36

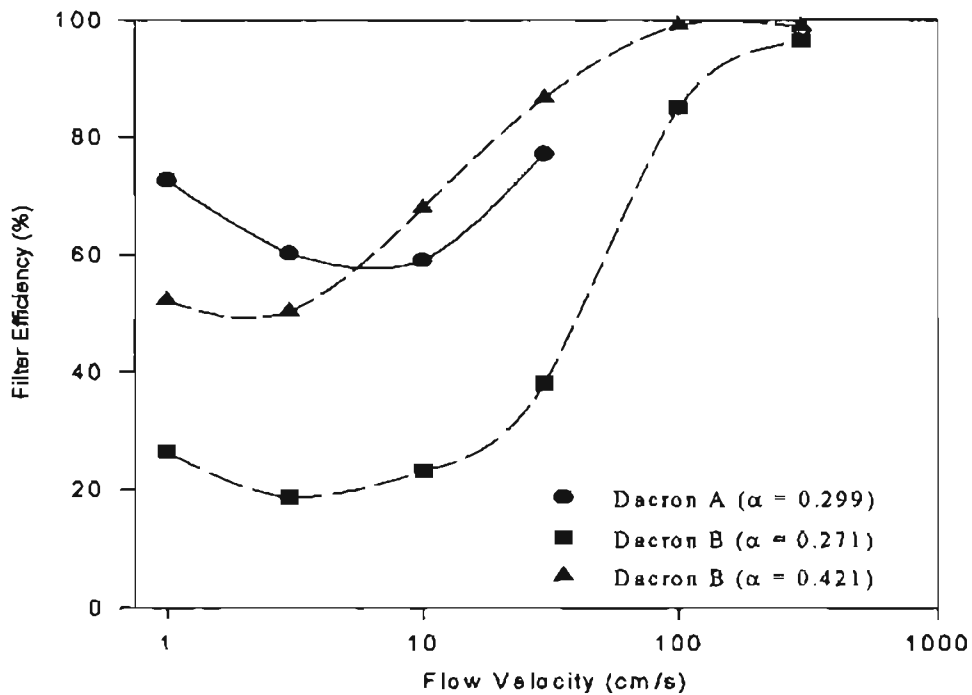


Figure 2.7 True Efficiencies for 1 μm Particles [Lee, 1977].

Lee and Liu [1982] also compared their results to various theories and found them in good agreement with the theory. All of the attempted comparisons are at low filter solidities where the theory would seem to match the experiments, as the theories cannot account for the effect of the neighboring fibers precisely, an effect which is important at higher filter solidities.

The fact that particle deposition during the process of filtration changes the filter characteristics has been known for a long time. Keeping this in mind and the fact that theory is unable to simulate these changes, a number of researchers have designed and carried out experiments to study this dynamic filtration process. The most important

aspects of such a study are the variation of filter efficiency with loading accompanied by the rise in pressure drop across the filter.

Jaroszczyk [1987] calls this dynamic filtration process 'non-stationary' filtration where structural changes caused by the deposited particles affect both filter efficiency and restriction. To investigate this process, a second order orthogonal approach experiment was designed wherein the filter performance which includes pressure drop, efficiency and dust capacity was represented by a function of aerosol velocity, fiber diameter, packing density and filter thickness. Experimental data for certain values of these parameters was obtained and extended to the entire range of these parameters using statistical techniques, thereby minimizing the number of experimental runs required to completely understand the dependence of filter performance on all of these parameters. The results from this study showed that filter efficiency has a maximum value for a certain aerosol velocity which can be determined for every filter medium and filtration process.

Another experimental study to understand the dynamic filtration process was done by Stinson et al. [1989] using a continuous aerosol monitoring system to make the measurements. They observed that efficiency and pressure drop were dependent not only on the loading but also on the particle size distribution, which determines the properties of the deposited dust cake and can cause changes in these two parameters by way of reentrainment or pinhole formation. Reentrainment occurs when the drag forces on the captured particles exceed the adhesive forces attaching them to the collectors. Pinholes are formed when the smaller pores get clogged and the flow is diverted to the larger pores which remain open. Wake and Jaroszczyk [1991] have made similar observations during

their experimental study and have shown that increasing the adhesive forces helps to increase the filter efficiency.

Jaroszcyk et al. [1993b] studied the reentrainment process via experiments. They showed that filter efficiency reduces at higher dust loading and aerosol velocities (Fig. 2.8). The dust cake at higher velocities becomes unstable and agglomerates of particles break loose and are re-entrained into the flow. This problem is more severe for fine dusts, as they do not have higher size particles which provide strength to the dust cake. Also, to achieve the same value of pressure drop, different amounts of dust of different size ranges are required, suggesting that filter performance cannot be characterized by one particular test dust.

Ptak et al. [1994] examined the factors influencing the performance of car interior air filters. Factors like flow rate, type of contaminants, filter defects, vibrations and environmental factors like temperature and humidity were evaluated. The effect of flow rate is shown in Fig. 2.9 which indicates a drop in efficiency with higher flow rate especially for lower particle sizes. This happens because the re-entrainment of particles increases with rising flow rate. Figures 2.10 and 2.11 show the effect of temperature and humidity on charged filter media. A decrease is observed in efficiency due to the deterioration of charge on the fibers caused by high temperature and humidity.

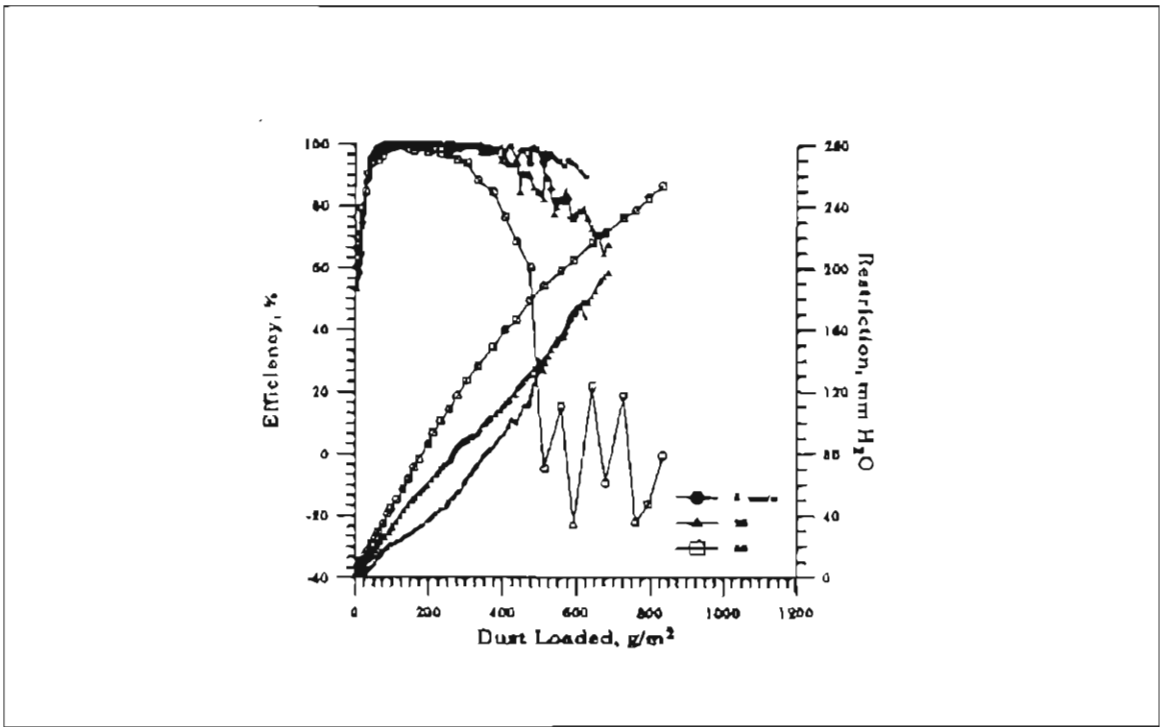


Figure 2.8 Performance of Filter Media for 0-10 μm Test Dust [Jaroszczyk et al., 1993b].

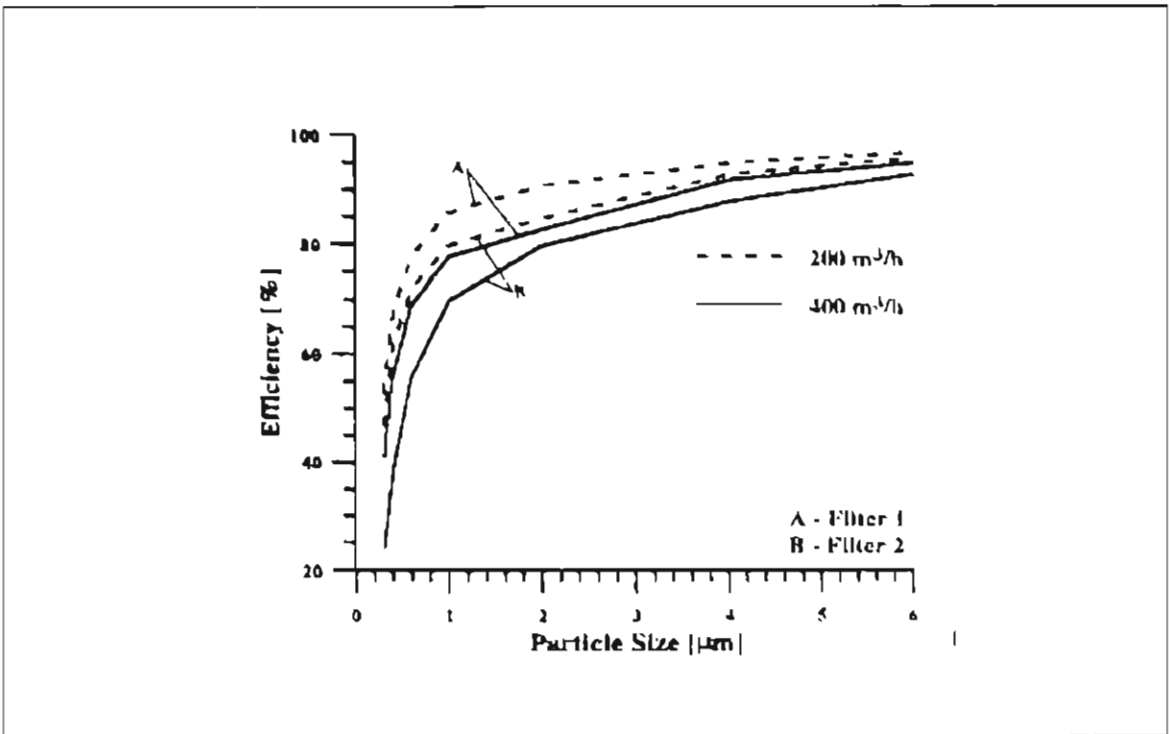


Figure 2.9 Dependence of Fractional Efficiency on Flow Rate [Ptak et al., 1994].

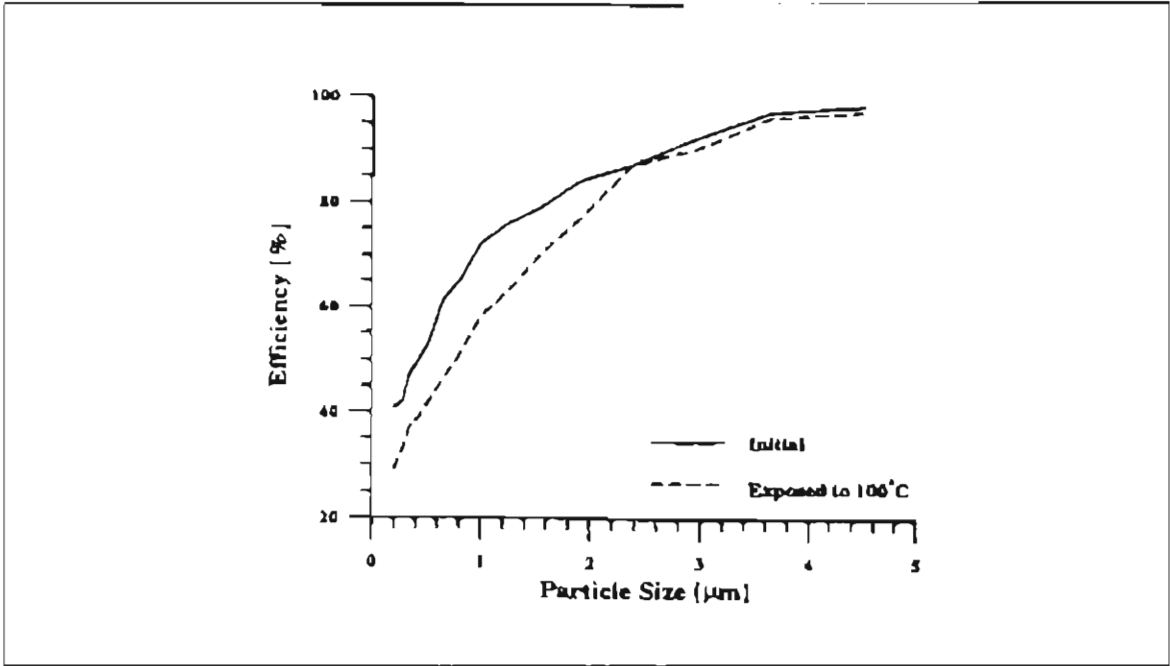


Figure 2.10 Dependence of Fractional Efficiency on Temperature [Ptak et al., 1994].

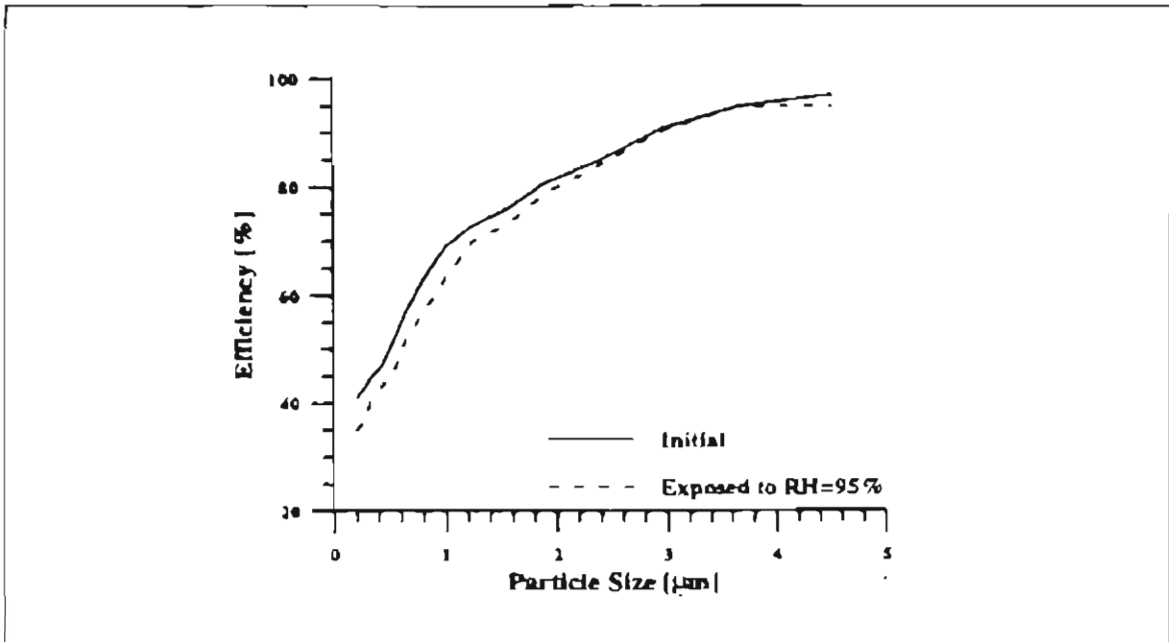


Figure 2.11 Dependence of Fractional Efficiency on Humidity [Ptak et al., 1994].

Williams [1996] and Natarajan et al. [1995a] conducted local efficiency measurements on flat media with the setup used for the present study. They varied the flow rates from 8.8 to 102 m³/hr. Although they were able to obtain relatively flat velocity profiles upstream, the same was not true for the upstream number densities (Fig. 2.12, velocity scale in Fig. 2.12 is expanded to show variations). Williams attributed this to the rebounded particles (after collision with the filter) being counted more than once. This would seem highly unlikely, keeping in mind that the measurement was made about 30 mm above the filter surface and the particles would probably not have enough kinetic energy to reach that location. On the downstream side, the number densities do not show any trend (flat profiles were expected as the filter was presented with a uniform velocity profile). Figures 2.13 and 2.14 show the local downstream number density and efficiency variation over the filter face, respectively. There is no trend in the efficiency which has a large variation from about 25% to 60%. The large variations in the number densities and efficiencies were attributed to experimental errors. Williams did some reliability checks on the setup but was unable to verify repeatability and accuracy satisfactorily. These issues will be discussed in greater detail in Chapter 4. The overall efficiency plots of Williams do show a trend similar to the one predicted by Davies [1973]. A comparison of these results with the present work will be done in Chapter 5.

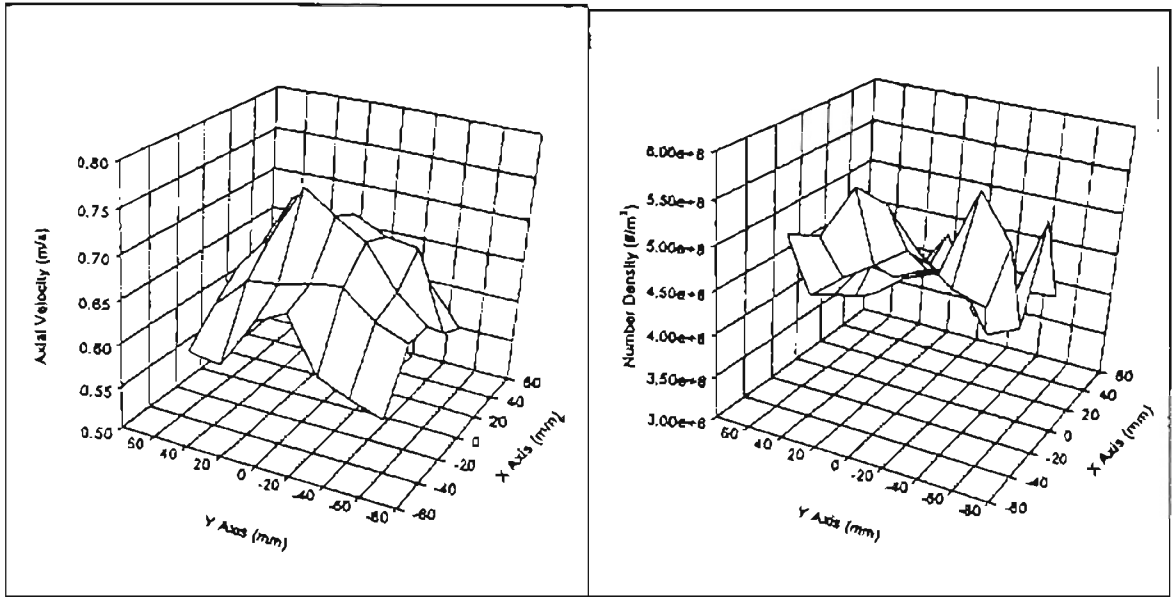


Figure 2.12 Axial Velocity and Particle Concentration Upstream of the Filter (42.5 m³/hr, Diffuser, 0.966 μm particles) [Williams, 1996].

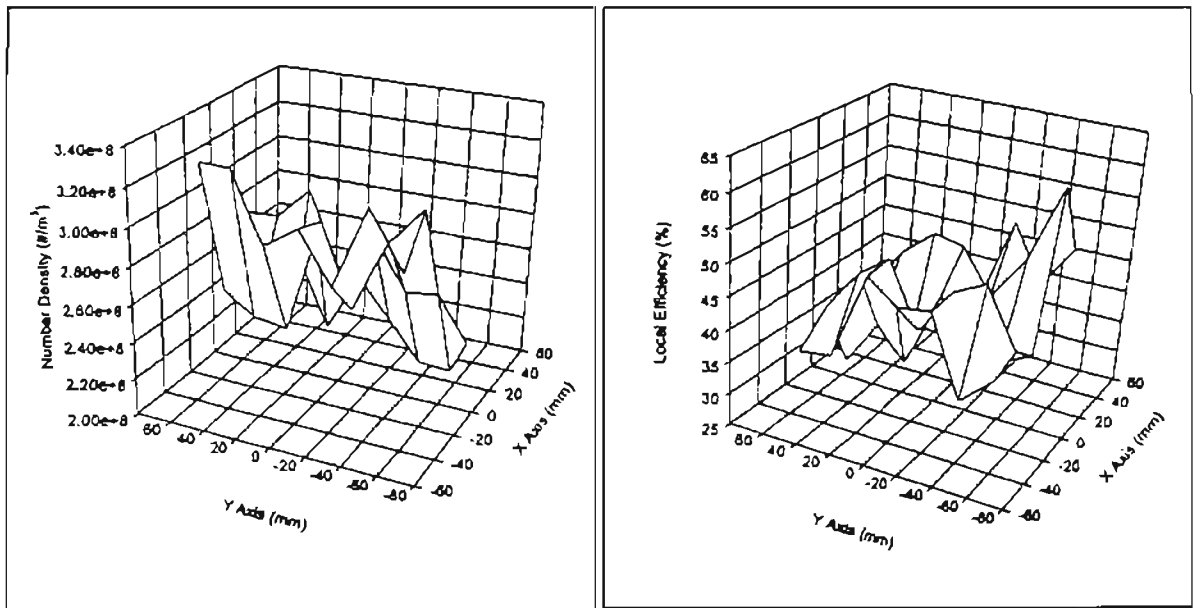


Figure 2.13 Number Density Downstream of Filter (42.5 m³/hr, Diffuser, 0.966 μm particles) [Williams, 1996].

Figure 2.14 Local Efficiency of Filter (42.5 m³/hr, Diffuser, 0.966 μm particles) [Williams, 1996].

Jadbabaei [1997] conducted experiments on pleated filters using the setup of Williams. The present study is based on the filter media employed in the manufacture of these pleated filters. The overall results are shown in Fig. 2.15 and Fig. 2.16 and indicate well defined trends, while the repeated measurements confirm the reliability and accuracy of the test results. A direct comparison with these results will be done in Chapter 5.

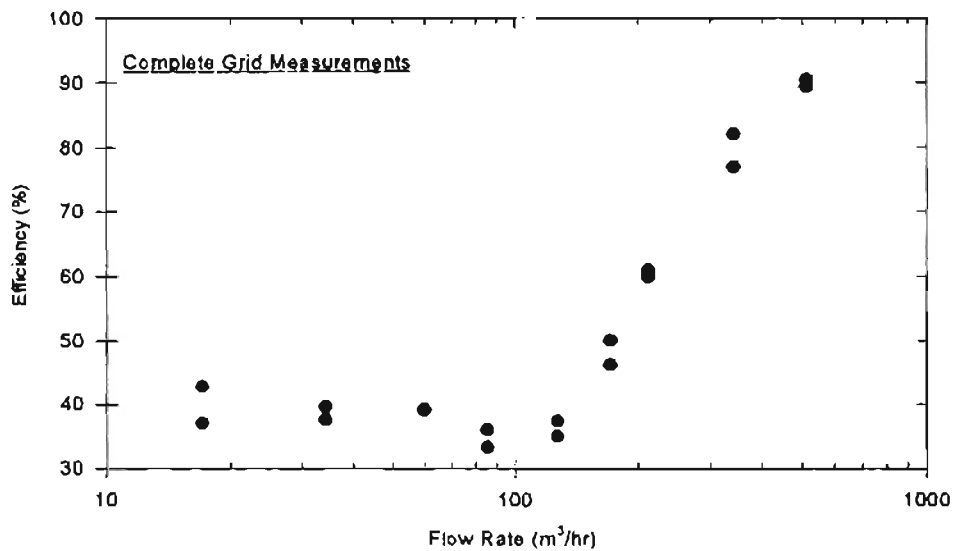


Figure 2.15 Overall Efficiency Measurements for Pleated Filter over Complete 5 x 7 Grid (Diffuser, 0.966 μm Particles) [Jadbabaei, 1997].

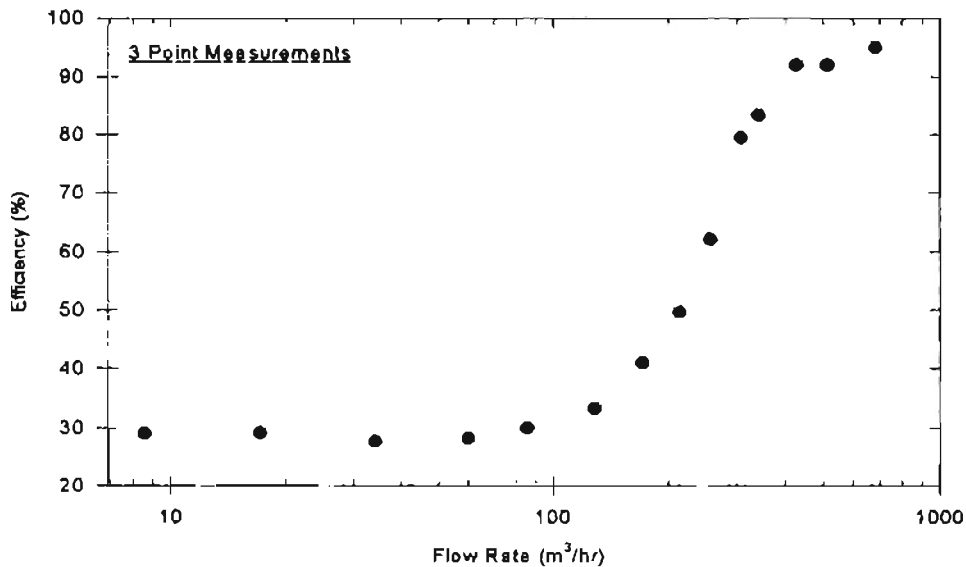


Figure 2.16 Overall Efficiency Measurements for Pleated Filter Using Three Point Averages (Diffuser, 0.966 μm Particles) [Jadbabaei, 1997].

2.6 Recent Developments

Several developments in the field of filtration have been published recently. These aim at improving the filter media, pleating design and testing procedures. Some of these developments will be reviewed in this section.

Electret fibers used to manufacture filter media involve the use of a combination of electrostatic charge and coarse fibers to produce a filter media with high initial efficiency and low pressure drop. Several enhancements have been made to these media under proprietary technologies [Hseih et al., 1996]. Figure 2.17 [Hseih et al., 1996] shows the performance of these electret fibers during the filtration process. They have high efficiencies in the beginning of the filtration process due to electrostatic mechanisms. This electrostatic effect tends to reduce with the deposition of particles on the fibers. As the electrostatic mechanisms reduce, the deposition of particles on the filter media causes the mechanical effects to become predominant. A minimum efficiency value will be seen in the transition region where the effects are changing. The electret fibers have a more uniform deposition of dust particles than the conventional uncharged fibers which collect more particles on the inlet air flow side. This reduces the blocked area of the filter, resulting in a slower pressure drop increase. Hseih et al. [1996] conducted tests on ten different electret filter media and verified their improved filtration properties.

Gustavsson [1996] evaluated the performance and requirements of cabin air filters and suggested that a good filter media should have the following properties

- fine fibers
- many fibers

- low velocity (large filter area)
- electrostatic charge (helps initially)

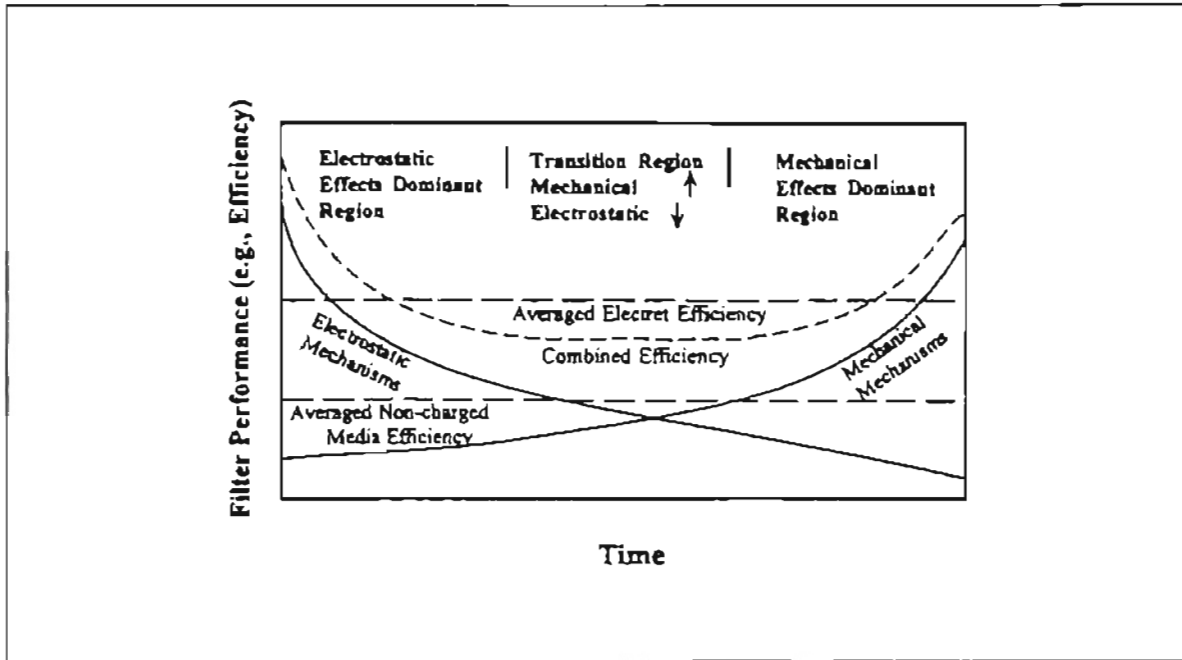


Figure 2.17 Schematic of the Performance of a Typical Electret vs. Time [Hseih et al., 1996].

Gustavsson suggests that smaller fiber diameter allows for better collection of smaller size particles (0-2 μm) especially after some dust has been deposited on the filter. He evaluated laboratory test dust versus atmospheric dust environment and concluded that laboratory test dust favors coarse electrostatically charged fibers which can easily get discharged under atmospheric conditions. Table 2.3 shows the effect of actual field conditions on cabin air filters at 340 m^3/hr (200 cfm). Gustavsson re-enforces the need to conduct tests with atmospheric conditions rather than with laboratory dusts.

Table 2.3 Cabin Filter Tested at 340 m³/hr, Used in Three Cars Under Normal Conditions [Gustavsson, 1996]

Filter	Distance km	Efficiency (%)		Pressure Loss Pa
		0.4 μm	1.0 μm	
new	-	32	55	67
in car 1	2550	17	43	82
in car 2	7117	14	30	80
in car 3	16530	7	19	76

Walker and Ptak [1996] conducted tests on cabin filters loaded in the field and compared them to laboratory loaded filters. Two field locations [Arizona and Alabama] were selected for their typical environmental characteristics. The results are shown in Fig. 2.18. They concluded that filter performance (efficiency and pressure drop) varied depending on the environment, and the SAE fine test dust reflected results similar to the two field locations. Also, laboratory tests for pressure drop measurements were reasonably close to those in the field as shown in Fig. 2.19 and Fig. 2.20.

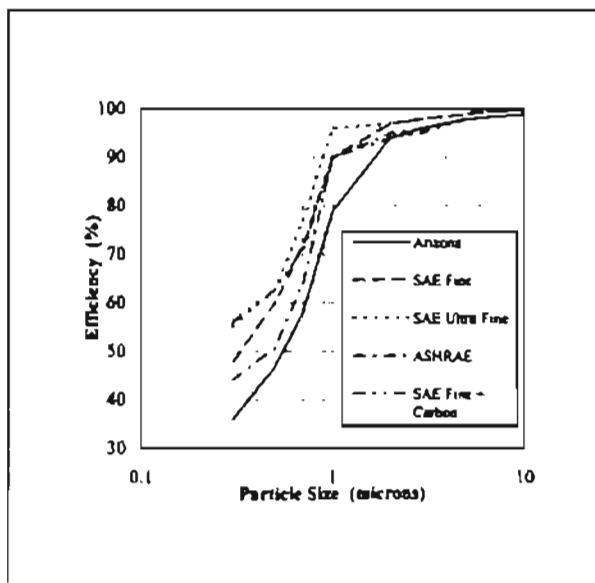


Figure 2.18 Influence of Loading with Different Dusts on Efficiency [Walker and Ptak, 1996].

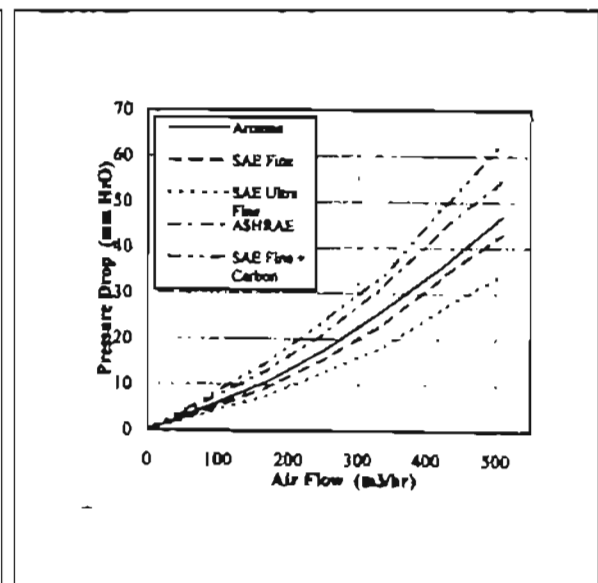


Figure 2.19 Dependence of Pressure Drop on Type of Dust [Walker and Ptak, 1996].

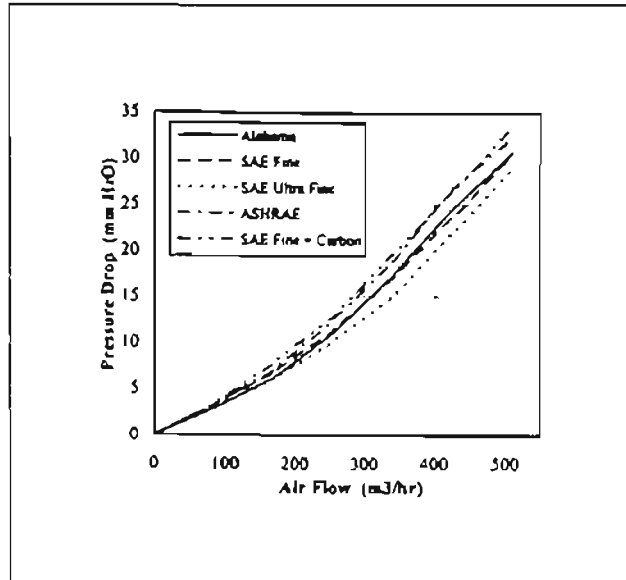


Figure 2.20 Dependence of Pressure Drop on Type of Dust [Walker and Ptak, 1996].

Lee [1996] also conducted tests on cabin air filters loaded in the field. Lee's tests were comprehensive as they involved more locations and larger fleet sizes (more cars). Filters from all locations were tested at intervals of 3500, 13000 and 24000 km. The results are shown in Figs. 2.21, 2.22 and 2.23. They do not show any specific trend (with dust loading) for pressure drop or fractional efficiencies stressing the importance of the environmental conditions in which the filter operates. Lee suggested that particle size distribution in each of the locations may be the key to explaining these somewhat random results, but conducted no particle size distribution measurements at any of the field locations. Lee [1996] also conducted in-vehicle tests and made measurements on a filter inside a moving vehicle. The results are shown in Fig. 2.24. This is probably the first reported in-vehicle test. The test vehicle followed another vehicle which generated the road dust. Two particle counters were used to make particle concentration measurements

inside and outside the vehicle. These tests were done on both highways and dirt roads. Because the outside particle concentration fluctuated due to the different driving conditions, wind direction and driving conditions of the leading vehicle, it was difficult to obtain solid quantitative data.

The recent advances in field filter testing help to provide a better idea of the filter performance under actual conditions. However, these field tests require large amounts of time and resources to carry out, indicating that laboratory tests may be the most efficient way of testing filter performance. Limited field testing can help in improving the laboratory tests and theoretical models so that they better simulate the actual conditions.

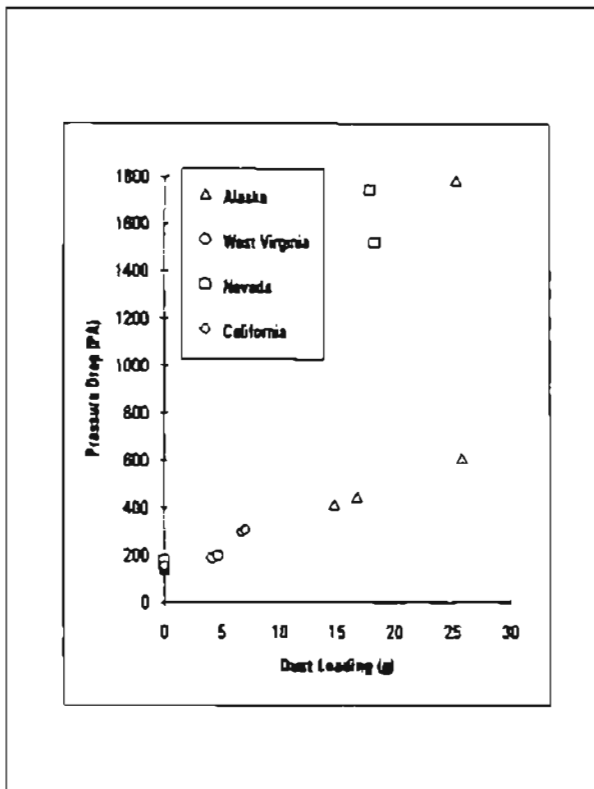


Figure 2.21 Pressure Drop vs. Dust Loading for Non-Woven Filters ($340 \text{ m}^3/\text{hr}$) [Lee, 1996].

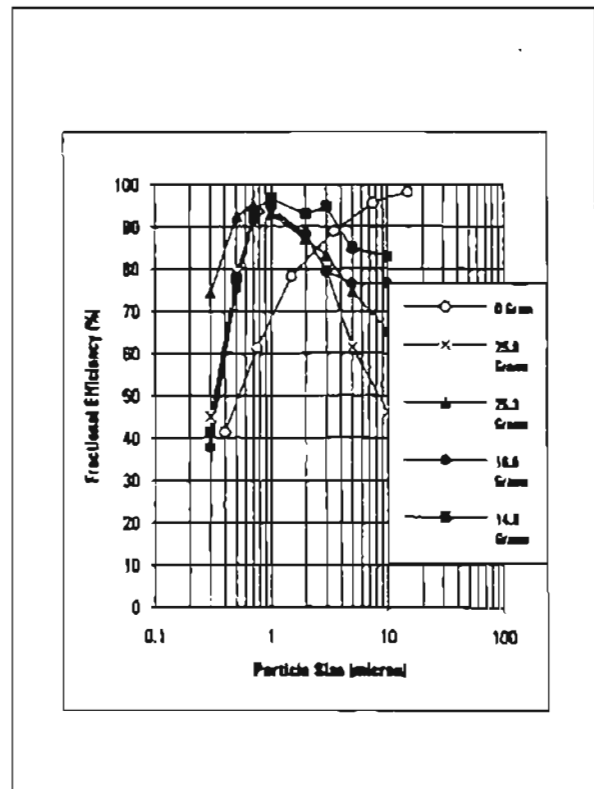


Figure 2.22 Fractional Efficiencies at Various Dust Loadings (Alaska, $340 \text{ m}^3/\text{hr}$) [Lee, 1996].

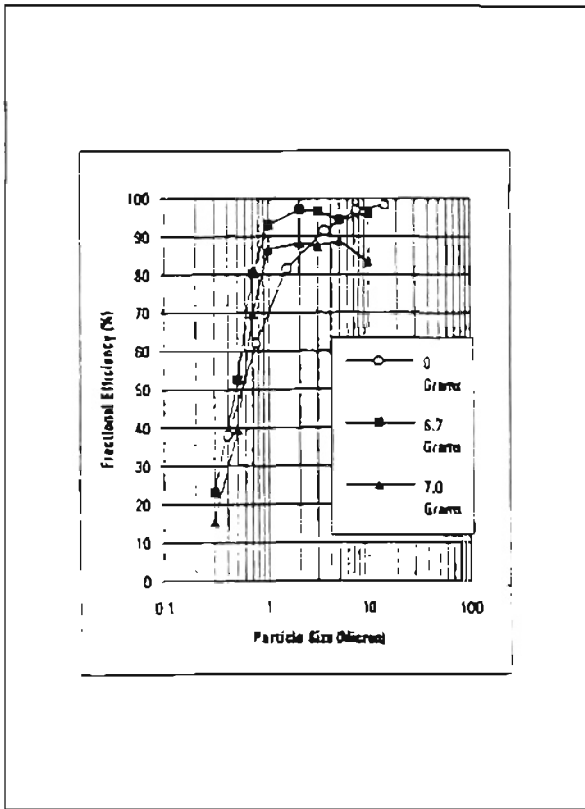


Figure 2.23 Fractional Efficiencies at Various Dust Loadings (California, 340 m³/hr) [Lee, 1996].

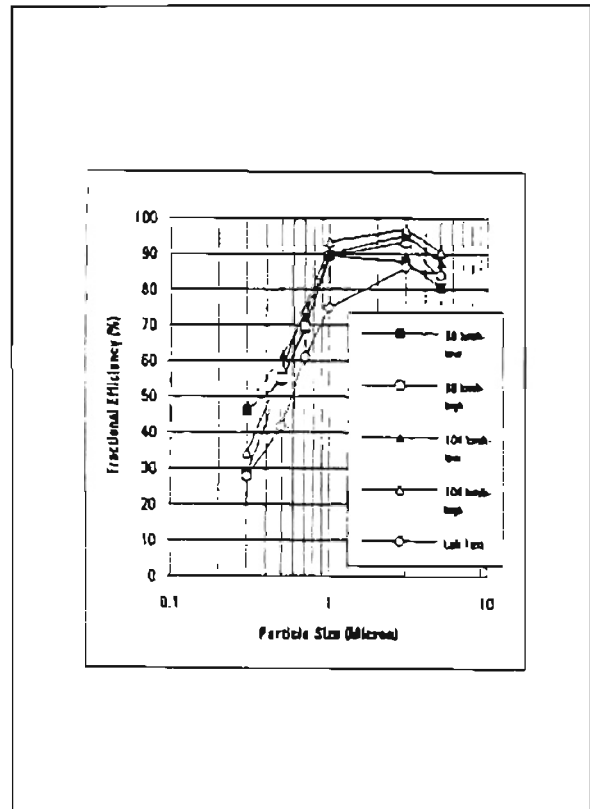


Figure 2.24 Overall Vehicle Particle Removal Efficiencies on Freeways (Different Blower Settings and Vehicle Speeds) [Lee, 1996].

Most filters used in automotive intake or cabin air filtration are of the pleated type. Pleated filters have higher dust holding capacity and efficiency due to the larger filter area and lower velocities. Also, pleated filters have lower pressure drops at higher velocities (typical to these applications) than flat sheet filters. Chen et al. [1996] studied the effect of pleat height and count on pressure drop of pleated filters experimentally. Figure 2.25 shows some of the results obtained by them. The purpose of the study was to obtain a filter pleat configuration which gave the lowest pressure drop. Figure 2.25 shows that the optimum pressure drop is a function of pleat count, pleat height and approach velocity. At

low pleat count, the pressure drop across the filter media increased due to reduced filter media area and increased media face velocity. At a high pleat count, the pressure drop also increased due to increased fluid viscous drag between the pleat spacings. Therefore, an optimal pleat count can be found for a given pleat height, which gives the lowest pressure drop across the filter panel. The minimum pressure drop point shifted to the lower pleat count and lower pressure drop when the pleat height was increased due to reduced pressure in the media dominated regime. Chen et al. [1996] used the experimental results to obtain a semi-empirical equation which can be used to design triangularly pleated filter panels. The model however fails to address how the pressure drop would influence the efficiency.

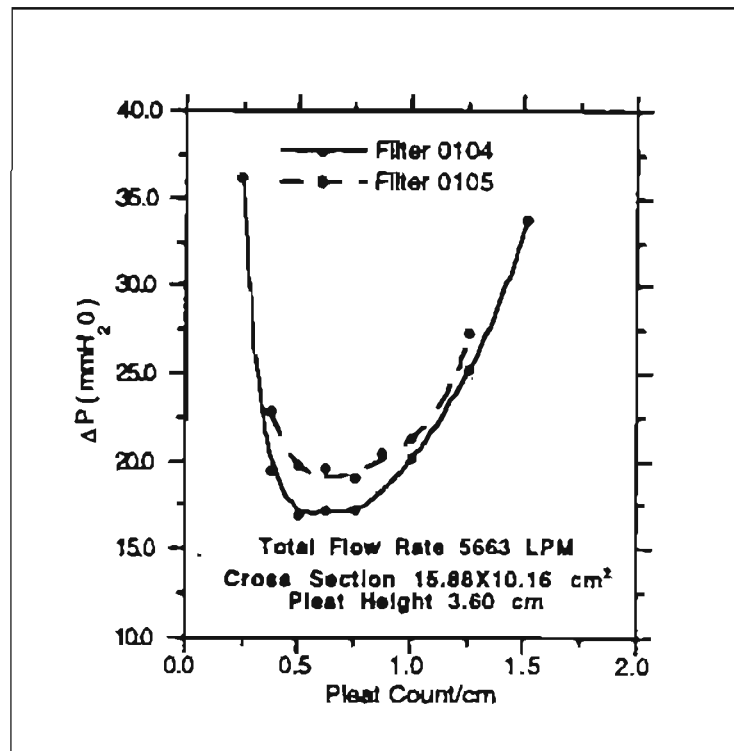


Figure 2.25 Typical Pressure Drop vs. Pleat Number Curve [Chen et al., 1996].

2.7 Present Work

Earlier sections in this chapter have reviewed both the theory and experimental studies done in the area of air filtration. While theoretical models can predict the filter performance to some extent, they are inaccurate and inadequate as far as simulating actual conditions. The literature shows that actual values of filter efficiency and pressure drop are lower than those predicted by theory. Most of the experimental work centers around dust loaded filters and compares efficiencies in the higher ranges (>90%). Also, the experimental work either relies on gravimetric measurements or single point measurements which do not display the complete behavior of the filter.

The present study aims at examining the filtration process more closely over a complete filter sheet to understand the influence of flow profile on the filter by making local efficiency measurements. Most of the literature assumes face velocity for pleated filters as the velocity obtained by distributing the flow uniformly over the open (stretched) filter. This study compares the performance of pleated and flat sheet filters of the same material to verify this assumption. The study also makes some preliminary measurements to quantify the effect of pressure drop on filter efficiency.

CHAPTER III

LDV INSTRUMENTATION AND THE FLOW SETUP

3.1 Overview

Filter efficiencies of the flat filter media were measured using a Laser Doppler System supplied by Aerometrics [Aerometrics, 1992]. Local measurements were made on a 5x7 grid (35 grid locations) (see Fig. 3.1) in a small angle diffuser housing similar to that specified under the J1669 cabin air filtration code [SAE, 1993]. The local efficiency at each grid location was determined from the upstream and downstream particle concentrations (or number densities) as

$$\eta_i = 1 - \frac{n_{i\text{down}}}{n_{i\text{up}}} \quad \text{at grid point } i \quad (3-1)$$

where $n_{i\text{down}}$ and $n_{i\text{up}}$ are the downstream and upstream number densities at the i^{th} grid location.

The particle concentration values at a location (either upstream or downstream) were obtained from the LDV measurement of average velocity (v_i) at the location, the number of particles counted (N_i) and the length of the time (t_i) taken to count those particles. Using the 'swept volume technique', developed by Liang [1994] (see Appendix B), the particle concentration was calculated as the number of particles contained in a volume having a cross-sectional area of the probe volume (point of intersection of the

laser beams) and length equal to the average velocity of the particles at the location multiplied by the time taken. Thus, the particle concentration or number density can be expressed as

$$n_1 = \frac{N_1}{v_1 t_1 A} \quad (3-2)$$

where A is the area of cross-section of the probe volume and equals $3.2 \times 10^{-11} \text{ m}^2$ [Liang, 1994].

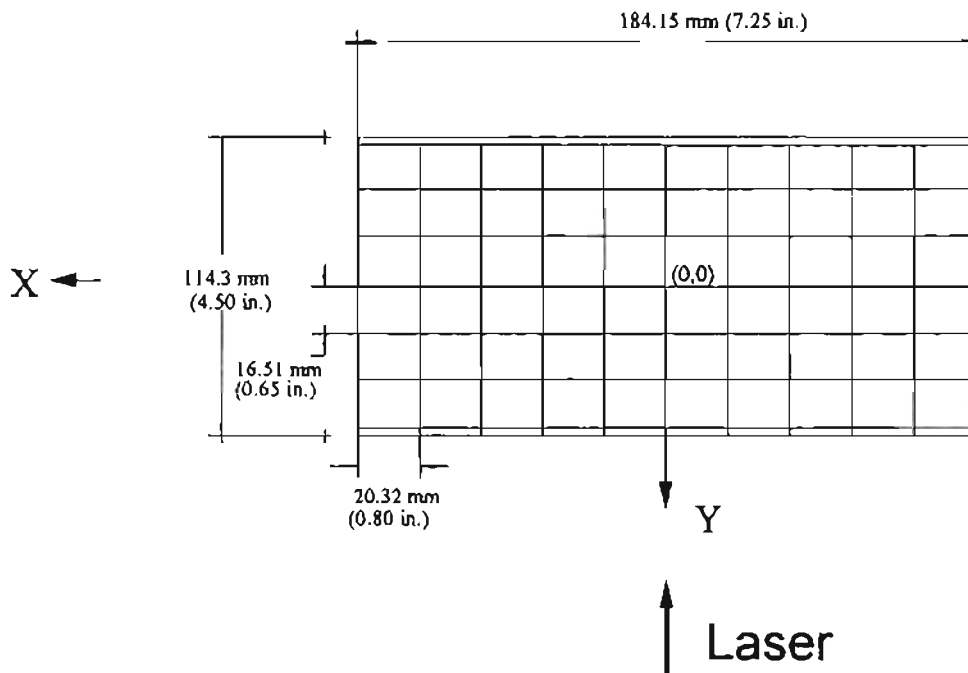


Figure 3.1 Measurement Grid over the Filter.

This chapter explains the LDV system and the flow setup along with the various parameters associated with them. Special emphasis will be placed on explaining the improvements made in the setup to obtain consistent data. Some tests which were performed to check the reliability and accuracy of the system will also be reviewed in

detail.

3.2 Laser Doppler Velocimetry System

The LDV system used for obtaining all of the data for this study is a two-component (or two-color) system coupled to an automated microcomputer (PC) based data acquisition system. The system is comprised of an optical setup required to generate the 'probe volume' and the electronic hardware to detect and process the signals (Fig. 3.2).

3.2.1 Optics of the LDV System

The measurements of particle velocity, particle count and the time taken to count the particles are accomplished by generating a probe volume at the location where these quantities are to be measured. The probe volume is created by the intersection of four beams (two green and two blue) resulting in an ellipsoid whose volume is estimated to be $1.388 \times 10^6 \text{ } (\mu\text{m})^3$ for blue beams and $1.674 \times 10^6 \text{ } (\mu\text{m})^3$ for green beams [Liang, 1994].

The two colors are used to measure the two components of velocity. One component is the axial component, perpendicular to the filter face, and the other component is the transverse component along the longer filter axis. Sample values of the velocities for the two components indicate that the transverse component is typically a fraction of the axial component and has a minimal influence on the resultant velocity until flow rates become as low as 5 scfm or until the probe volume is positioned in a recirculation zone. The third component, also being a transverse component along the

shorter filter axis, would be expected to be small in comparison to the axial component of the velocity. Therefore, the inability of the system to measure the third component of velocity along the smaller filter axis may cause a minimal error in the resultant velocity value. The velocity value v , used in Eq. (3-2) is the average resultant velocity.

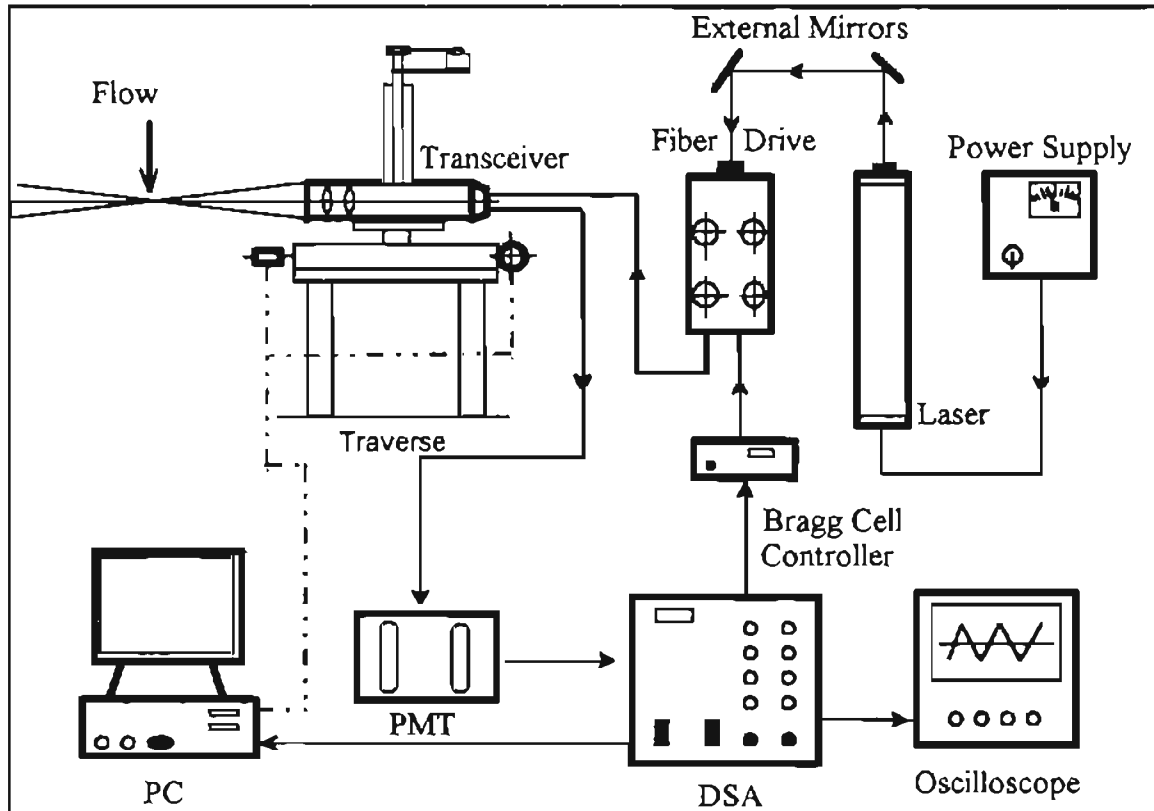


Figure 3.2 Schematic of the Laser Doppler Velocimetry System.

The laser beams which produce the probe volume are generated by a 5 watt Argon-Ion laser (see Fig. 3.2) supplied by Coherent (see Appendix A for specifications). The laser generates a multi-line, multi-wavelength beam which is guided into the fiber drive via two plane steering mirrors. Inside the fiber drive, the beam is split into four

beams of two colors (blue and green). One beam of each color is also frequency shifted by 40 MHz. This shift is used to detect the direction of particle motion in the probe volume. The splitting and shifting of the laser beam is controlled by a Bragg Cell while the separation is achieved by two dispersion prisms. The shifted and unshifted green and blue beams are directed into four independent fiber optic cables each of 4 μm diameter by means of focusing lenses housed inside the couplers located on the top of the fiber drive. The beams are then transmitted to the transceiver via the fiber optic cables. The transceiver is both a transmitter, transmitting the beams to create the probe volume, and a receiver, receiving the back scattered signals produced by a particle crossing the probe volume.

This particular LDV system works in the fringe mode. At the intersection point of the two similar colored beams, optical interference occurs which causes the generation of alternate bright and dark fringes. The intensity of the light in the probe volume is Gaussian in nature with the peak intensity at the center and decreasing to zero at infinity. A light intensity of $1/e^2$ is taken as the edge of the probe volume. It is near the minimum light intensity for detection of light signals [Drain, 1980]. When a seeding particle crosses the probe volume, it will scatter light matching the bright-dark-bright fringe pattern (Fig. 3.3) (high and low amplitude) superimposed on a low frequency high amplitude pedestal or envelope. This pedestal represents the Gaussian light intensity in the probe volume.

The 40 MHz shift given to one beam of each color causes the creation of a moving fringe pattern. This is useful in determining the direction of flow. If the particle moves in the direction of fringe motion, its relative velocity with respect to the fringes is smaller and

so will be the frequency of the detected signals. For motion in the other direction, the relative velocity increases thereby, increasing the frequency. A stationary particle inside the probe volume will generate a signal with a 40 MHz frequency.

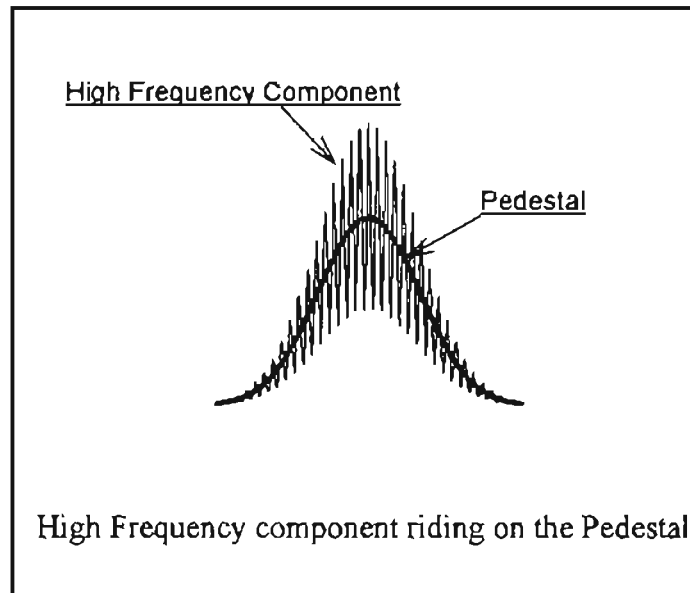


Figure 3.3 A Typical Laser Doppler Signal.

In order to obtain quality signals, it is important that the probe volume have optimum light intensity which remains stable during the course of the experiment. Also, the fringes in the probe volume should be well defined so that the signals have clean intensity variations as the particle crosses the fringes. A fall in the light intensity in the probe volume can cause a decrease in the particle count per unit time (sample rate). This happens because a fall in intensity causes the $1/e^2$ envelope to reduce in size, thereby decreasing the effective probe volume. The probe volume cross-sectional area is taken as a constant in Eq (3-2), but a decrease in light intensity causes a decrease in the actual

swept volume in which the particles are counted. The net result is a decrease in the measured particle concentration at the location.

The actual probe volume cross-sectional area is dependent on the light intensity to which the beams have been aligned. The constant value of the probe cross-sectional area (A in Eq. (3-2)) corresponds to a certain beam intensity which may not be always possible to achieve. This will affect the absolute particle concentrations measured but will have no influence on the efficiency value which is a function of the ratio of the number densities at the upstream and downstream locations (Eq. (3-1)), both having the same area term which cancels out. However, a change in intensity during the experiment will cause different sample rates at the upstream and downstream locations, and there can be no basis to compute the correct ratio of the number densities.

The intensity of the beam coming out of the laser head was monitored for a long duration of time on different days using a power meter. It was observed that this intensity remained constant with time. A close check on the beam powers coming out of the transceiver indicated a change in power (or intensity) especially when the blower was running. Beam powers can be optimized by aligning the optics inside and outside the fiber drive. Small changes in beam power can be restored by re-aligning the beams to focus accurately on the fiber optic cable using the X, Y and Z adjustment knobs on the couplers of the fiber drive. Large variations in beam power cannot be restored, and finally the beams will start deteriorating. The alignment has to be very precise, as the optical fibers have a diameter of 4 μm , and even a small change in focusing the beams on them can cause a significant drop in power.

To understand why this decrease in beam power occurs, the author examined the external factors affecting the optical system, especially when the blower was operational for flow generation. Through a trial and error process, many factors were evaluated as potential causes.

3.2.1.1 Factors Influencing the Optical Setup

The presence of a high power blower close to the optics would suggest that the vibrations were affecting the optical alignment. The laser, external mirrors and the fiber drive are mounted on an optical breadboard with the help of screws. The breadboard has a honeycomb structure sandwiched between two metal plates to give it strength and also dampen the influence of the vibrations. The board is placed on a metal table. In order to further dampen the vibrations from the blower, an acoustic screen is placed around the blower.

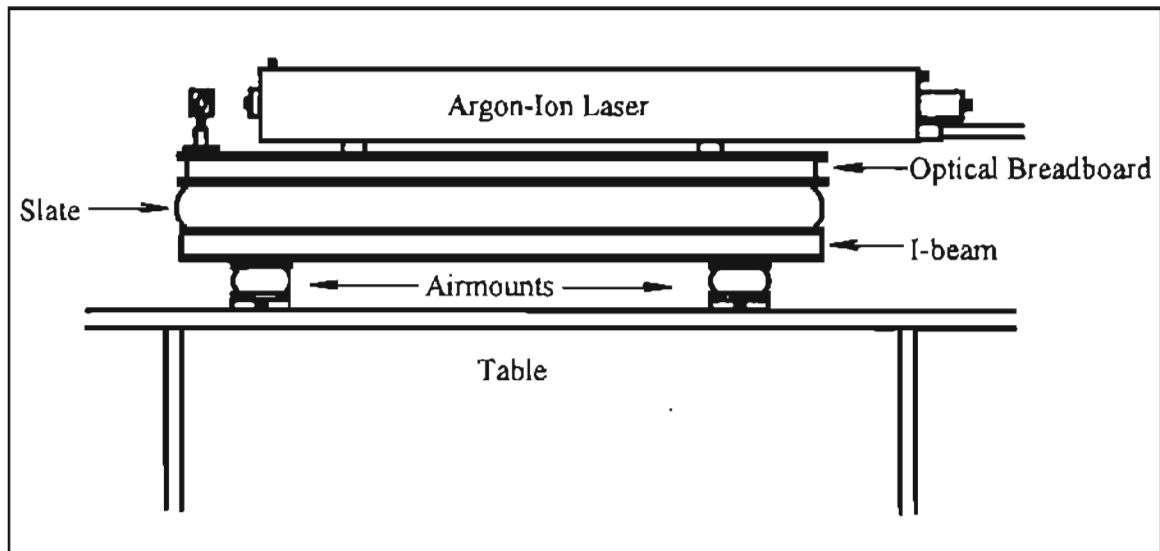


Figure 3.4 Mounting Base for the Optical Setup.

To completely minimize the effect of the vibrations, the author designed and fabricated a mounting base (see Fig. 3.4) on which the breadboard was supported. The mounting base was comprised of four air-filled isolation pads called airmounts, supplied by Firestone (Model No. WO2-358-5000), and inflated to 30 psi each. This inflation pressure was determined from the specification sheet, keeping in mind the frequency of vibrations for the total load supported. Each airmount inflated to 30 psig and supporting a load of 400 lb. has a natural frequency of vibration of 4.2 Hz (specification sheet for airmounts). Two I-beams of 4"x 4" cross section were placed on the airmounts (each supported by two mounts) along the longer sides of the breadboard. The I-beams supported a 1" thick plate of slate cut to the dimensions of the breadboard. The slate is a rigid material and provides a strong support for the breadboard. Finally, the breadboard with all its optics was placed on this plate. In order to make the entire setup rigid, the breadboard, the slate and the top flange of the I-beams were clamped together in six places. This clamping configuration was arrived at by a trial and error process and will be discussed in greater detail elsewhere in this section.

Following the installation of the mounting base, power measurement of the four beams was repeated, but showed no significant improvement in terms of stability. To further isolate the optical setup, a Plexiglas box was designed and built around it. This led to a small improvement in the beam power stability suggesting that possible acoustic and/or air related factors were influencing the optics. A small rise of about 2 to 4 °C in temperature was noticed when the blower was running. This rise in temperature was due to the inability of the air-conditioning system to compensate for the large amounts of room

air exhausted by the blower to the external environment.

The next logical step was to examine the influence of the temperature changes on the beam intensities. A small test experiment was setup for this purpose. A thermocouple was attached to the top surface of the breadboard and a thermometer was placed close to the fiber drive to monitor the board and room temperatures in the vicinity of the optics. A power meter was placed so as to measure the green unshifted beam power continuously from the transceiver. The experiment was begun by aligning the green unshifted beam to optimum power at a stable room and board temperature of 25°C. The room was then gradually heated by a gas heater located in the room. The room and board temperatures along with the beam power were measured as a function of time.

The plots for these values (Fig. 3.5) indicate a gradual rise in both temperatures for about one hour. The rise in board temperature is lower than the rise in room temperature as it is heated by natural convection and the heating rate is quite rapid for the board to be in equilibrium with the air in the room at all times. The corresponding plot for the green unshifted beam power indicated a drop in beam power from 50 mW to 35 mW, a 30% change. This large change in beam power is caused by the misalignment of the external turning mirrors with respect to the fiber drive optics, a direct consequence of the breadboard thermal expansion. An adjustment in the second external mirror helped in restoring some of the lost beam power (for complete restoration, the fiber drive optics would have to be realigned for this new external mirror configuration) which supports the explanation of breadboard expansion. To further confirm the breadboard thermal expansion theory, the author placed an alignment scope (provided by Aerometrics) in

place of the coupler for the green unshifted beam. In its aligned position, the beam should hit the center of the crosshairs on the scope, but, at this higher temperature, the beam had been translated to one side. This could be corrected by adjusting the external mirrors.

After the one hour period, the heater in the room was turned off and the beam realigned. This time a beam power higher than the initial value was achieved because of a different alignment configuration. The lag in the board and room temperatures caused the board temperature to keep rising for a short duration after the heater had been turned off. During the cooling period, the beam power rose initially before deteriorating again. The board temperature measurements were made using a thermocouple having a limited least count ($0.1\text{ }^{\circ}\text{C}$) causing a sharp edged plot of the board temperature.

This experiment confirmed the influence of temperature on beam power. A few more checks on beam power at relatively constant temperature (variation less than 1°C) indicated no significant change in beam power. The results of one such check are shown in Fig. 3.6. In order to alleviate this problem, the temperature in the Plexiglas box around the optical setup was maintained within $\pm 0.5^{\circ}\text{C}$ of the temperature at which the optics was aligned during the course of the experiment. Also, the beam powers were checked at the beginning of and at regular intervals during an experiment. During downtime, the room was maintained at a temperature close to the alignment temperature, so that at startup, the time required for the setup to reach the stable temperature was minimized. This is critical keeping in mind the temperature lag between the breadboard and the room air.

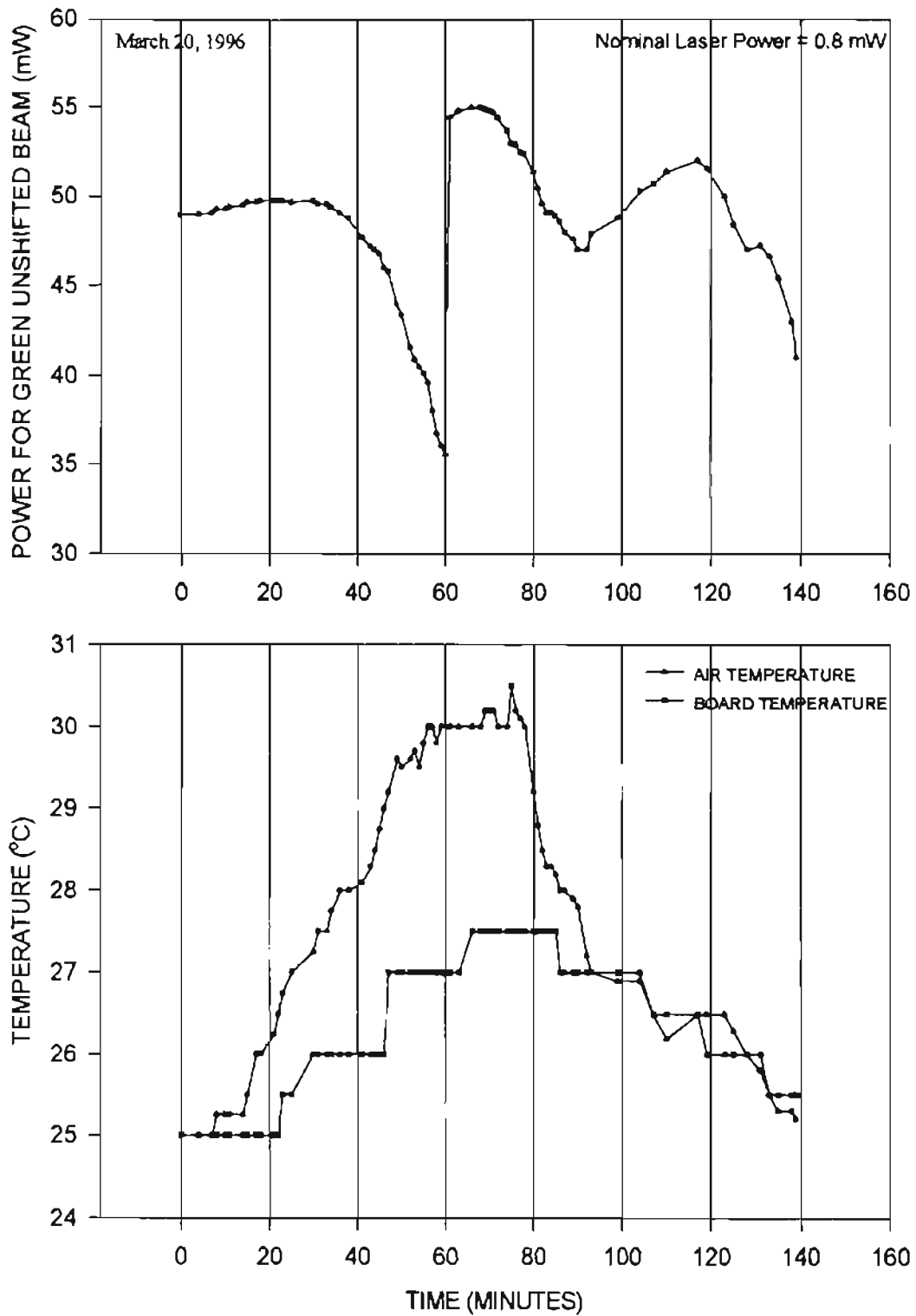


Figure 3.5 Influence of Temperature on Beam Power (Green Unshifted Beam).

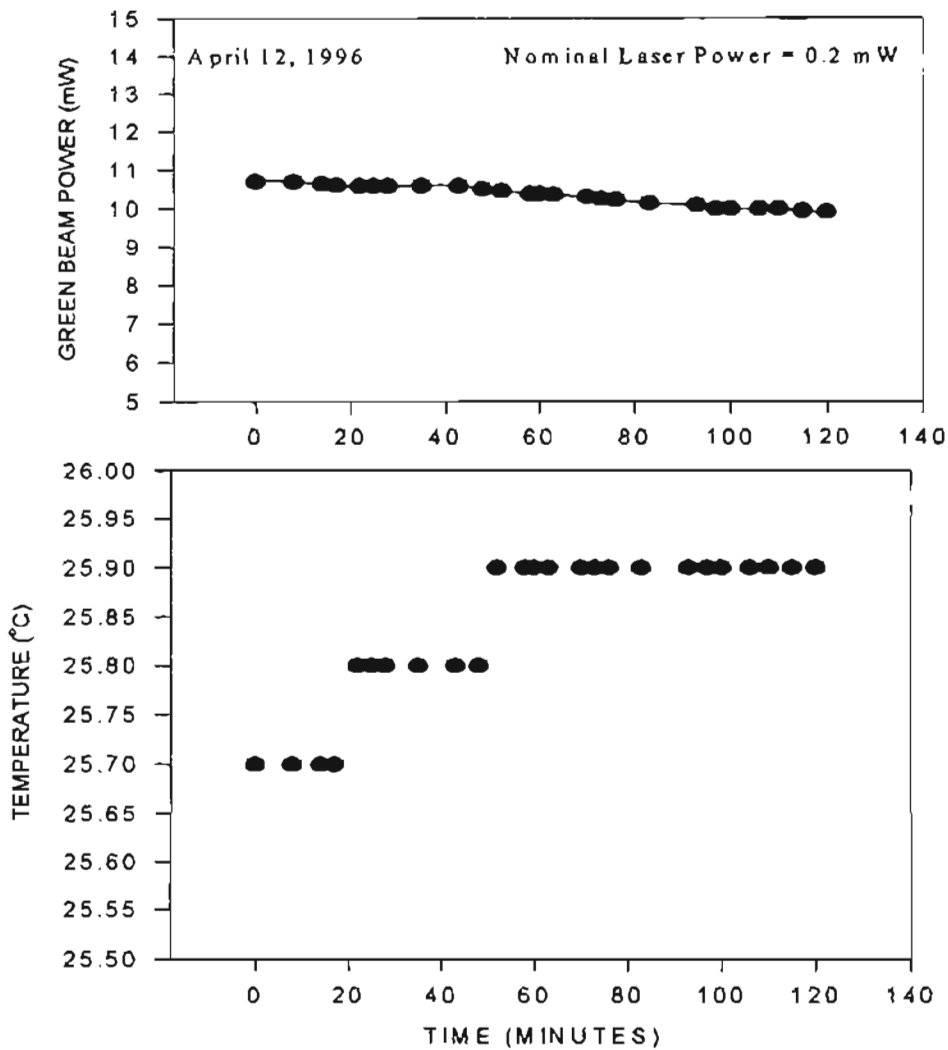


Figure 3.6 Beam Power Variation at Constant Temperature.

Another critical factor in obtaining high quality signals is the generation of fringes with optimal contrast inside the probe volume. This helps in obtaining signals which have a distinguishable high frequency component required for accurate velocity measurement. The beam splitter in the LDV system used in this study is based on beam polarization and causes a phase change between the two beams of each color. For good fringe contrast,

the interfering beams should be exactly in phase [Drain, 1980]. To ensure that the two beams of each color are in phase, their polarization was checked at the transceiver using a polarizing plate. The maximum and minimum light intensities for the two same color beams coming out of the plate should be at the same angular rotation of the plate (to ensure they are in phase) and the ratio of the maximum to the minimum should be 100 or greater (to ensure better fringe contrast). In case this ratio is less, the fiber needs to be rotated in its casing. This is a time consuming trial and error process as the beam needs to be aligned by the X, Y and Z knobs on the couplers each time. An aid in this process can be created by sticking a piece of tape around the screw cap which holds the fiber to the coupler and marking some rotation angles on it.

Some sample curves of the minimum light intensity as a variation of time are shown in Fig. 3.7. They indicate that the minimum intensity is not a constant value, but fluctuates with time. The author's goal was to minimize these fluctuations and reduce the peak value to the minimum possible by adjusting the rotation on the fiber. This peak value was used for calculating the maximum to minimum light intensity ratio. Also, after obtaining the desired ratio, the signal quality observed on the oscilloscope may still be bad. This indicates that the two beams are 90° out of phase and one fiber needs to be rotated by the 90° amount to rectify this problem.

A good alignment of the optical system is as important as configuring the electronic hardware which processes the signals. The next section will deal with the components and configuration of the electronic hardware.

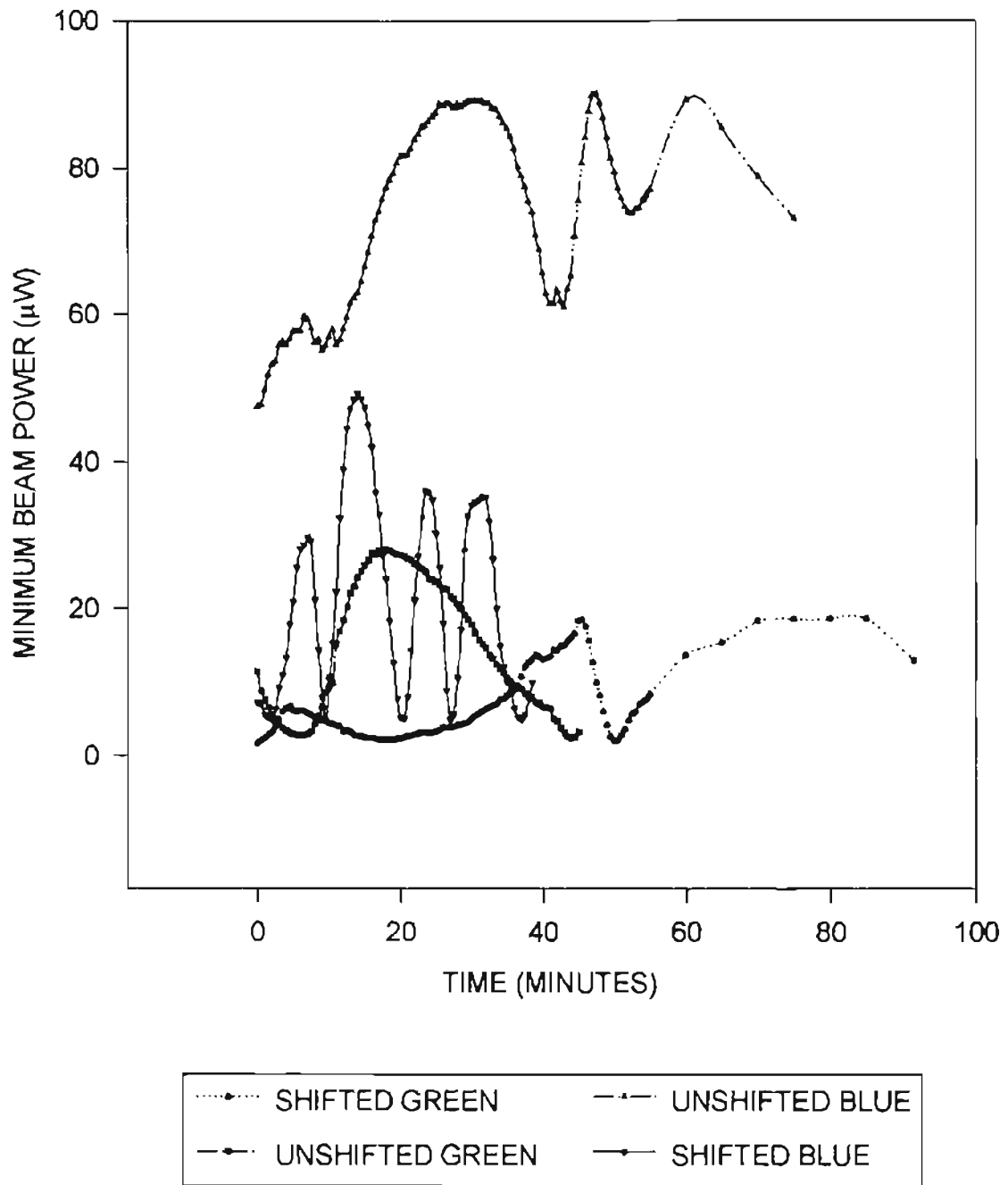


Figure 3.7 Minimum Polarized Beam Intensity Variation.

3.2.2 Signal Processing Setup

The back scattered signals are picked up by the transceiver and taken back to the

photomultiplier tubes (PMT) (see Fig. 3.2). The PMT converts the optical signal into an electronic signal which can be handled by the processing hardware present inside the Doppler Signal Analyzer (DSA) hardware box. In order to monitor signal processing and aid the adjustment of processing parameters, the signal at various stages of processing is displayed on an oscilloscope (see Fig. 3.8).

There are four signals displayed on the oscilloscope. The first signal (top) is the raw unprocessed signal after the PMT and pre-amplifier. The next step in processing is the removal of the Gaussian pedestal, since only the high frequency component is required for velocity calculations. This is achieved by a high pass filter. The second signal on the oscilloscope indicates the high pass filtered signal which is the Doppler burst without the pedestal. The next signal on the oscilloscope is the log signal. It is the condition of the signal after a logarithmic amplification is done on it to increase the amplitude of the signal and compress its dynamic range. The final signal on the oscilloscope is the burst detector signal which helps to locate the burst and issue a signal to the controller to transfer the sampled signal to the buffer for processing. A dedicated digital signal processor board is used to compute the Discrete Fourier Transform (DFT) using a Fast Fourier Transform (FFT) algorithm. This is done to compute the frequency spectrum of the signal and hence, the velocity of the particle by inverting the frequency. The signals for each of the two channels (or colors or velocity components) can be viewed independently on an oscilloscope through the BNC connectors for each channel provided on the front panel of the DSA.

In order to ensure accurate signal processing, it is important that the parameters

which control the settings of the hardware components of the DSA are set correctly. The parameters can be adjusted easily from a computer interface. Although a large number of parameters can be adjusted on the DSA, only some are important in terms of the flow. Some of the parameters have been configured on a permanent basis (particularly the ones related to the optics of the system) and should not be changed. For a detailed discussion of these parameters refer to the DSA manual [Aerometrics, 1992]. The author will examine the influence of some of the critical parameters on data acquisition in the following section.

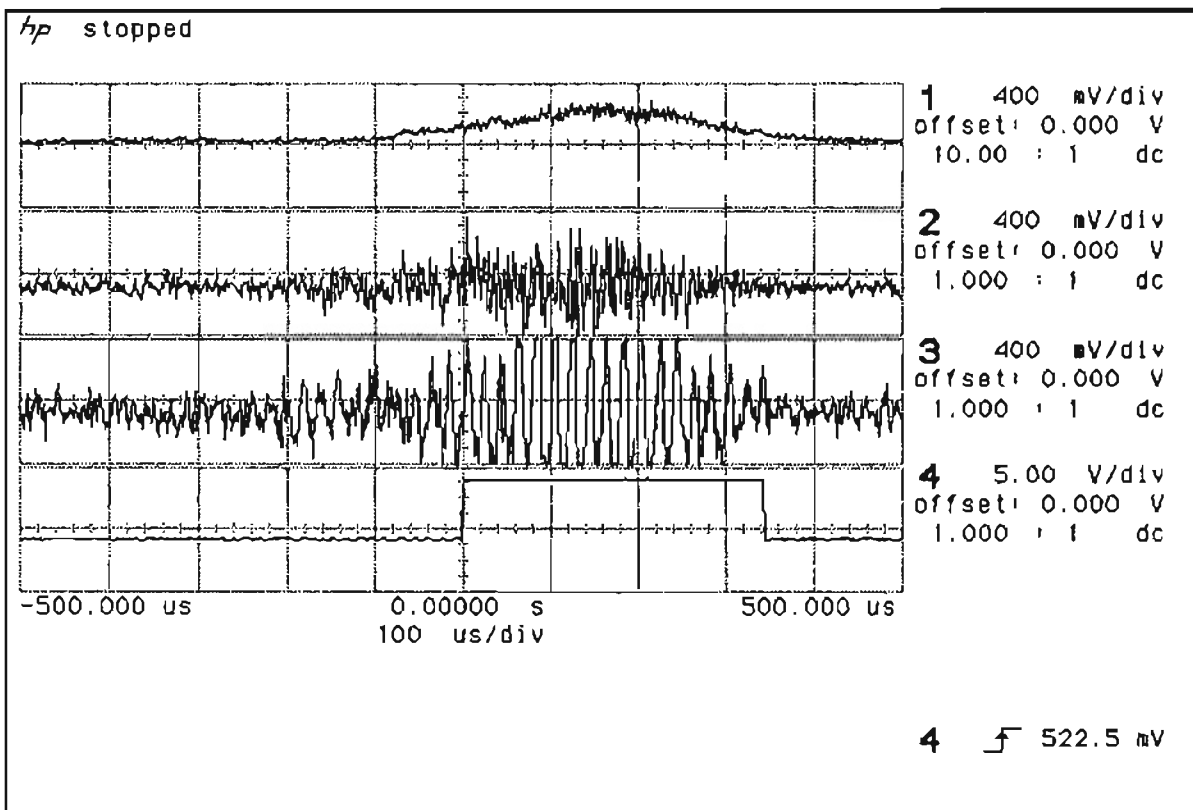


Figure 3.8 Sample Oscilloscope Screen.

3.2.2.1 DSA Parameters

Most of the key DSA parameters are set on the F3 velocity setup page of the DSA

software. These include

1. **High Voltage.** This is the voltage supplied to the PMTs and controls the amplification of the detected signals. It has a range of 200 to 800 volts. Selecting a very low value leads to the signal not being detected whereas setting a very high value saturates the PMTs. Depending on the beam intensity, flow rate and seeding density, the author used values from 550 to 750 volts. The high voltage setting has a big influence on the data rate and the quality of the data. The correct setting of high voltage has to be chosen in conjunction with other parameters like threshold and data validation. These will be discussed later in this section.
2. **Frequency Shift.** This is the frequency shift given by the Bragg Cell to the shifted beam of each color. This is a hardware dependent variable and has a value of +40 MHz for our system and should not be changed any time.
3. **DC Offset.** This parameter adjusts the raw signal to a common ground level. Depending on the laser beam intensity, the DC offset is set to a value such that the raw signal is just above the zero line on the oscilloscope. This ensures proper threshold operation, burst centering and signal processing. A value in the range of 10 to 20 mV was used by the author.
4. **Mixer Frequency and Low Pass Filter.** The author used a value of 40 and 20 MHz for these parameters respectively for all the experiments. For a detailed discussion on setting these parameters, refer to the DSA manual [Aerometrics, 1992].
5. **Burst Filter.** The burst filter restricts the frequency range encountered by the burst detector circuitry. To select the correct value, first the burst filter is set to 'All Pass',

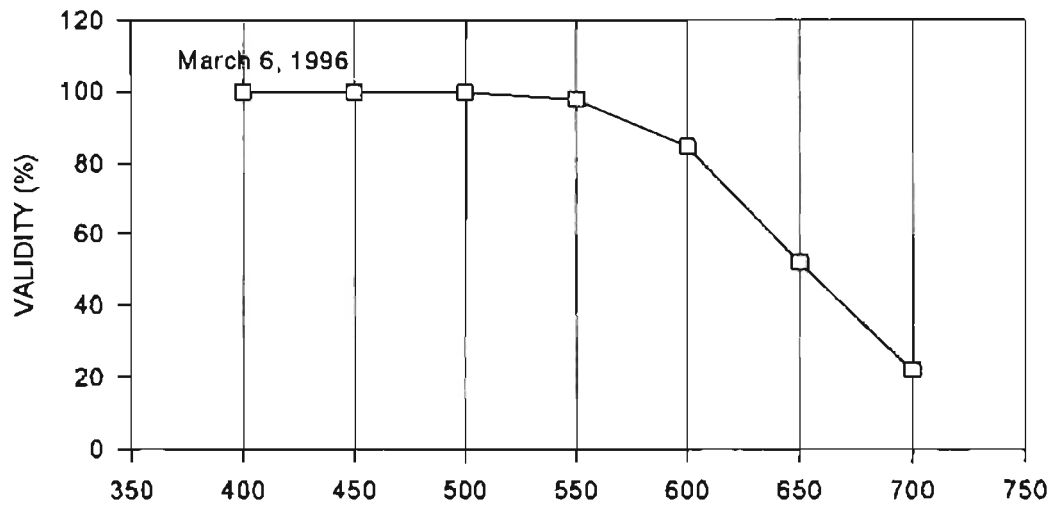
and some sample data is collected. Depending on the frequency of the signal (velocity of the particle), the correct value of the burst filter can be set. The 40 MHz band pass setting (35 MHz to 45 MHz) is suitable for velocities with Doppler frequencies less than 5 MHz, i.e. velocities with maximum levels between ± 15 m/s. Similarly, the 50 MHz low pass setting is suitable for signals with Doppler frequencies less than 10 MHz corresponding to velocities less than ± 28.5 m/s.

6. **Threshold.** The threshold determines the minimum signal amplitude required to cause a burst detection. Burst detection is critical in storing the signal correctly in the buffer before processing. It is set by observing the burst and the raw signals on the oscilloscope. Set the threshold such that the burst detector should stay on (up) for the duration of the burst. The author used a threshold value of around 60 mV. A high value of threshold improves the data validation rate, which is defined as the ratio of the number of validated signals to the attempted signals, but slows down the data rate as the signals require a high amplitude to be validated. High amplitude signals are produced when a particle crosses the probe volume at its center where light intensity is the maximum. Lower amplitude signals are produced when a particle crosses the probe volume away from the center. Setting the threshold too high causes these low amplitude signals to be rejected. A low value of the threshold can cause noise to be validated as a good signal. The threshold has to be adjusted in conjunction with the high voltage which controls the amplitude of the electronic signals obtained from the PMTs.

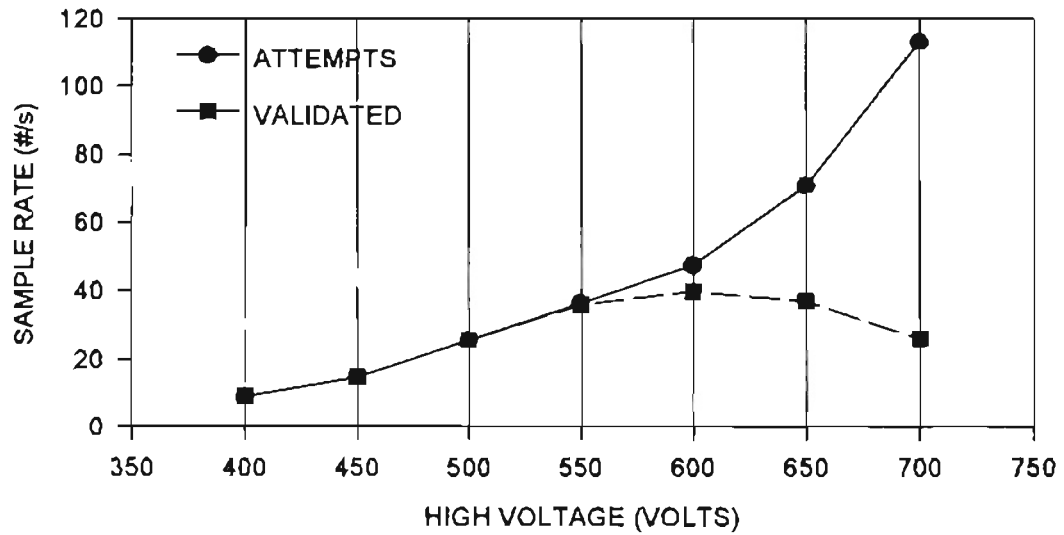
In order to determine the correct operating range for the high voltage and the

threshold, the author performed a short test. Data samples were collected for high voltage settings from 400 V to 700 V with a constant threshold of 60 mV. The plots of validity and sample rate, shown in Fig. 3.9, indicate that the validity percentage falls at around 575 V after remaining constant from 400 to 550 V. A look at the validated sample rate indicates that this is the voltage at which the sample rate peaks before falling. The rise in sample rate with high voltage is because of the increase in the signal amplitude; but, for values of high voltages greater than 600 V, the sample rate falls because of the amplification of the noise levels causing the signal-to-noise ratio (SNR) to be low and resulting in the rejection of signals. The gap in the attempted and validated sample rate plots is indicative of the validity.

A similar observation of validity and sample rate with threshold for a constant high voltage is shown in Fig. 3.10. It indicates a sharp rise in validity from 65% to 85% when threshold is raised from 40 to 60 mV, beyond which the validity gradually rises to 100%. During this period, the sample rate remains nearly constant. In order to achieve our goal of highest data rate with a good validation (neither too high as it rejects good signals, nor too low as it accepts noise as signals), a high voltage of around 600 volts with a threshold of around 60 mV is a good combination. This combination holds for the particular flow investigated and needs to be re-evaluated for other flows. Also, the settings used depend on the optical alignment and the power of the laser beams at the transceiver.



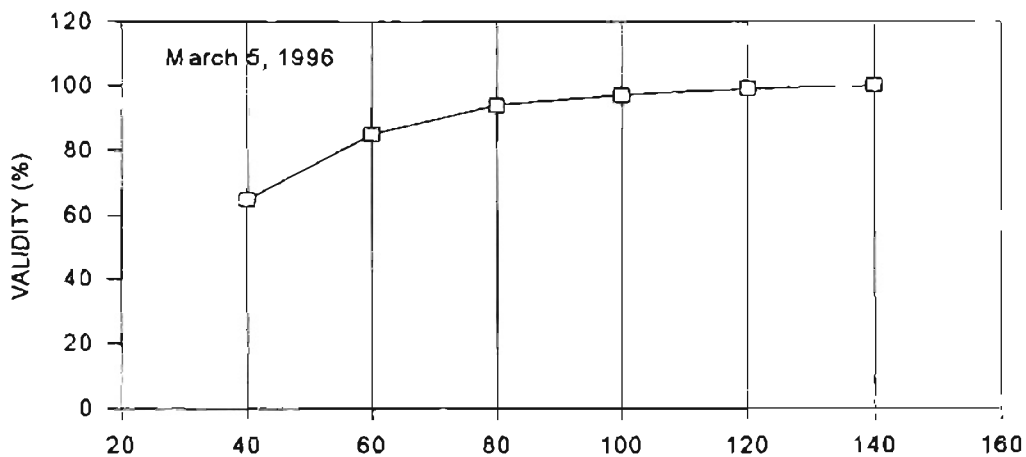
Validity vs. High Voltage



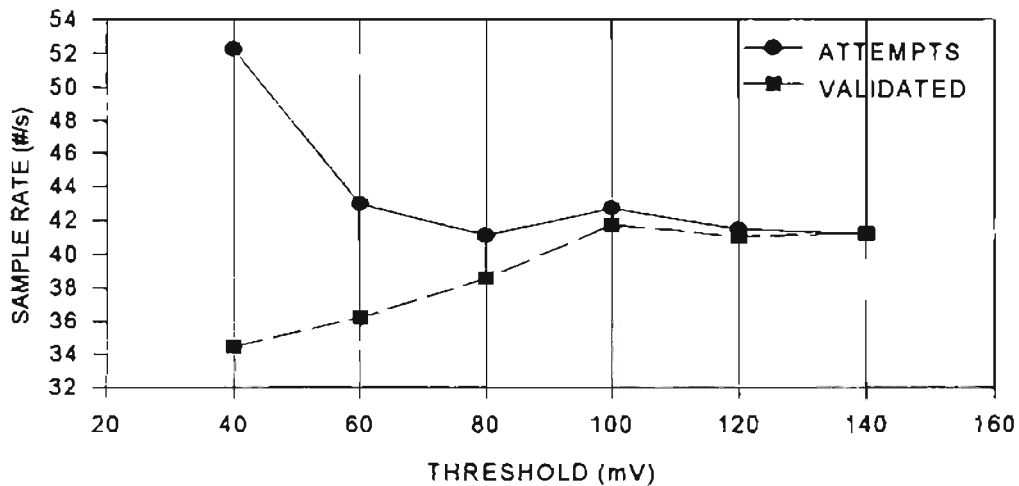
Sample Rate vs. High Voltage

Flow Rate = 128.25 m³/hr (75 cfm); Nominal Laser Power = 0.8 W; Threshold = 60 mV

Figure 3.9 Influence of High Voltage on Data Acquisition.



Validity vs. Threshold



Sample Rate vs. Threshold

Flow Rate = 128.25 m³/hr (76 cfm); Nominal Laser Power = 0.8 W; High Voltage = 690 V

Figure 3.10 Influence of Threshold on Data Acquisition.

- Envelope Filter. The envelope filter smooths the burst signal by removing the high frequency noise. It should be set at 100 ns to start with and then increased such that it is shorter than the shortest burst length. The burst lengths may be observed on the oscilloscope or in the ALT-F9 single sample data acquisition mode, where they should

be approximately equal to gate time (the time during which the signal is stored in the buffer of the computer) to prevent multiple detection in one burst.

8. **Peak Detection and % after Peak.** This parameter helps to detect the center or the highest amplitude of the burst, thereby enabling the signal around the peak to be processed by the processor. In cases where background noise is very high, the peak detector may be unable to locate the highest amplitude. Then the peak detection should be turned off. The percentage after peak indicates the percentage of the signal sampled after the peak. A value of 50% ensures the signal is sampled evenly around the peak. When the peak detection is turned off, the percentage after peak indicates the signal sampled after the burst. Therefore, in that situation, this value should be set to zero.

9. **Number of Samples and Sample rate.** The number of samples determines the frequency and velocity resolution of the instrument. The sampling rate and the number of samples must be set so that aliasing is avoided (which appears as repeated histograms of velocity distributions on the data acquisition screen; a consequence of erroneous signal frequency detection due bad signal sampling). This is achieved by setting the sampling rate greater than twice the Doppler signal frequency and the record length shorter than the burst length so that all the sampled points are within the burst. The relationship between record length, sampling rate and the number of samples is given as

$$\text{Record Length} = \frac{\text{Number of Samples}}{\text{Sampling Rate}} \quad (3-3).$$

For low velocity flow rates, the record length will generally be less than the burst

length for a sampling rate of 80 MHz, but, to increase the accuracy of the measurement, it is a good idea to increase the record length to around 80% of the burst length. This allows for a greater length of the signal to be sampled, and the frequency of the signal is determined more accurately. Thus, for low flow rate especially when the velocities inside the housing were close to zero, the author used sampling rates of 5 or even 2.5 MHz. If record length is greater than the burst length, velocity histograms with strange characteristics may result (like large negative velocities can appear in the histogram away from the mean).

10. Minimum Signal-to-Noise Ratio. This value determines the minimum quality of the burst signal to be accepted. Aerometrics defines this signal-to-noise ratio with the magnitudes of the spectral components in the frequency 'bins' shown in the single burst data acquisition screen (ALT-F9). It is defined as

$$SNR = \frac{Power_{j-1} + Power_j + Power_{j+1}}{\sum_{i=0}^N Power_i - (Power_{j-1} + Power_j + Power_{j+1})} \quad (3-4)$$

where j = bin with maximum power magnitude.

The minimum SNR should be set around 0.3, which corresponds to a -5.2 dB signal level, in order to reject poor quality signals while maintaining a high data rate. The SNR of each signal can be seen on the ALT-F9 single burst data acquisition screen.

11. Enabled Range. This parameter is the velocity range calculated by the DSA software based on the optical setup, sampling rate, mixer frequency and filter selections. Depending on the flow rate, this parameter has to be monitored and adjusted by

changing the above parameters. For low flow rates, it is advisable to use a velocity range closer to the actual velocity to improve the display accuracy of the velocities.

12. Velocity Maximum and Minimum. These are the velocity bounds set on the measurement. They are primarily set to obtain a good resolution of the velocity distribution histogram on the screen.

13. Measurement Range. Depending on the enabled range and the user defined values of the maximum and minimum velocities, the DSA software determines a range over which the velocity measurements will be finally made. This range is the measurement range and should encompass the possible velocity values to be encountered in the flow.

Some of the other parameters also need to be set on the F4 Diameter Menu Setup page. These include the data drive, experiment name, test name and run number to fix the location of the saved data on the hard disk. The data acquisition can be stopped in 2 modes, the sample mode and the time mode. In the sample mode, the number of valid samples after which the data acquisition is to be stopped can be specified on this page. In the time mode, the data acquisition halts after the specified time, irrespective of the number of samples collected. The author used the sample mode to collect all of the experimental data for this study. The number of samples used varied according to the flow rate and the seeding density to restrict each run to a reasonable time span.

The measurement of quality data depends not only on the instrumentation but also on the experimental setup. The next section will explain the flow setup used in this study in detail.

3.3 Flow Setup

The flow setup (Fig. 3.11) is used to generate the flow environment in which the flow is tested. The flow setup can be broken down into four components. They are

- Seeding Mechanism
- Housing
- Filter Mounting
- Flow Generation and Measurement

An explanation of each of these components is provided next.

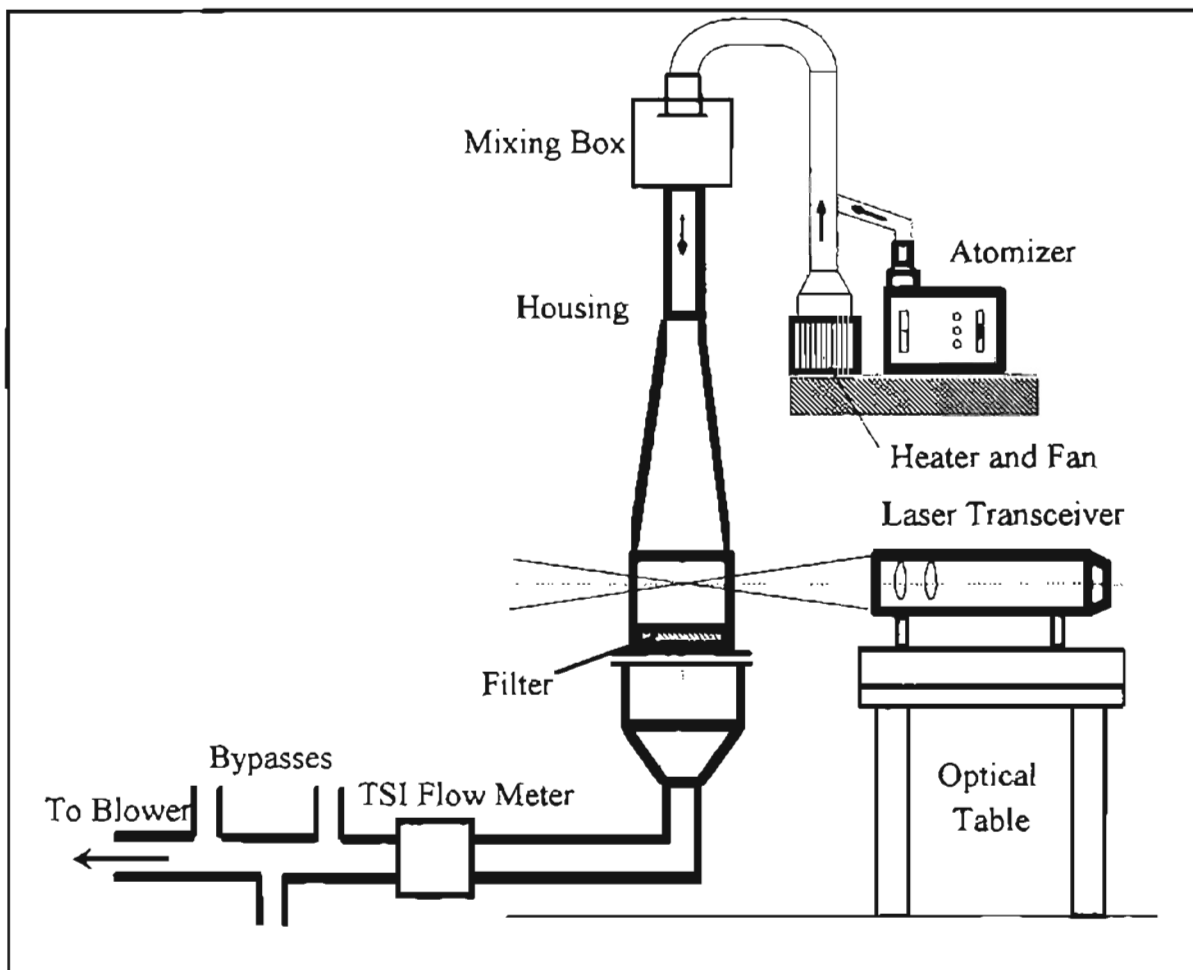


Figure 3.11. Flow Setup for the Small Angle Diffuser Housing.

3.3.1 Seeding Mechanism

In order to measure the efficiency of the filter, the flow needs to be seeded with a contaminant. All experiments in this study were carried out using 0.996 μm diameter monodisperse polystyrene latex particles (PSL). These particles are also required to detect velocity as the LDV system needs “seeding” particles to measure the flow. Since the particle size is small, it was assumed that they have the flow characteristics of the air flowing in the setup.

The flow was seeded using TSI’s Model 9306 six-jet atomizer. The atomizer uses compressed air to draw a water or particle solution from a reservoir and break it up into a very fine spray by forcing it through a very small orifice (see the TSI manual for more details). The atomizer has a pressure regulator and an air dilution system to control the seeding rate. It also allows for two or four jets to be used to change the seeding rate. The PSL particles are available in a 10% solid solution commercially. The author used a 1% or 0.5% solution of this commercially available solution in distilled water to prepare a suspension which was atomized and used for seeding. The concentration value was varied to prevent the filter media from clogging up and affecting the efficiency measurements during an experiment. The problem of clogging is more severe at low flow rates, as the number densities at these flow rates are high (Eq. (3-2)). Therefore, the lower concentration was used at the lower flow rates.

In order to remove the water droplets from the spray, a heater was used to heat the air flow into the duct. The thermostat on the heater was short circuited to ensure that it operated continuously. To verify that no water droplets reached the filter,

measurements were attempted using distilled water without PSL particles. No signals could be recorded by the LDV system, confirming that the heater was working satisfactorily.

The performance of the atomizer could be affected if its jets were clogged over a period of use. Different experiments under similar flow conditions would show different values of number density. To ensure repeatability, the atomizer jets were cleaned thoroughly at frequent intervals (say after five experiments). Also, to ensure that the particle consumption rate from the atomizer and the measured number densities were in the same range, a calculation of expected number densities was done based on the solution consumption rate. The expression for number density (n) can be developed from the known volume flow rate (Q in cfm), the volume of solution used from the atomizer (V_{al} in ml), the particle diameter (d_p in μm) and the time (t_{sol} in seconds) taken for consumption of this solution. The number density is given as

$$n = \frac{\text{Number of Particles Consumed in Time } t_{sol}}{t_{sol}Q}$$

$$n = \frac{\text{Volume of Particles Consumed in Time } t_{sol} / \text{Volume of One Particle}}{t_{sol}Q}$$

$$n = \frac{\frac{V_{al} (0.1 \times 0.01 \times 10^{-6})}{\frac{\pi}{6} d_p^3 (10^{-4})^3} \text{ m}^3}{\left(\frac{12 \times 2.54}{100}\right)^3 \left(\frac{1}{60}\right) t_{sol} Q \text{ m}^3} = 4.047 \times 10^{12} \frac{V_{al}}{t_{sol} Q d_p^3} \quad (3-5)$$

3.3.2 Housing

The housing (see Fig. 3.12) used in the present work was the small angle diffuser

housing as specified in the SAE J1669 cabin air filtration code (see Fig. 3.13). The top section of the housing has a gradual diffuser angle of 6.34° . This ensures that the flow is uniform at the filter plane. The standard housing used for testing filter efficiency is the SAE J726 (see Fig. 3.14) intake air housing. The SAE J726 housing has been shown to have recirculation zones along the edges [Natarajan, 1995] caused by the separation of flow due to the large diffuser angle. Since the flow coming into the housing was from one side, a mixing box was used at the entry to the housing. This would potentially reduce the flow bias from the side from which the duct turned. The housing has a top section and a bottom section which are separated by an aluminum plate on which the filter is mounted. The flanges of the top and bottom half along with the aluminum plate in between are clamped together to a stand on which the housing is supported. The bottom half of the housing is similar to the top half except for it having a shorter nozzle section, thereby leading to a steeper nozzle angle. The front faces of the top and bottom sections (where the laser enters) are of glass which is scratch resistant and has better optical properties than Plexiglas. This prevents the probe volume from being distorted due to refraction of the beams passing through the Plexiglas.

In order to monitor the pressure drop during the experiment, two pressure taps are provided in the housing. One tap is in the upstream section while the other tap is on the downstream section. These are then connected to an inclined manometer to determine the pressure drop across the filter at different times during an experiment. Since the pressure drop changes in the setup are small, it is advisable that an inclined manometer be used instead of a U-tube manometer as it has a lower least count. Another aspect which needs

to be carefully addressed is the alignment of the housing. The level of the housing should be checked with a spirit level at different locations along with its alignment with respect to the transceiver. The transceiver should be exactly perpendicular to the front face of the housing so that the velocity components can be measured accurately.

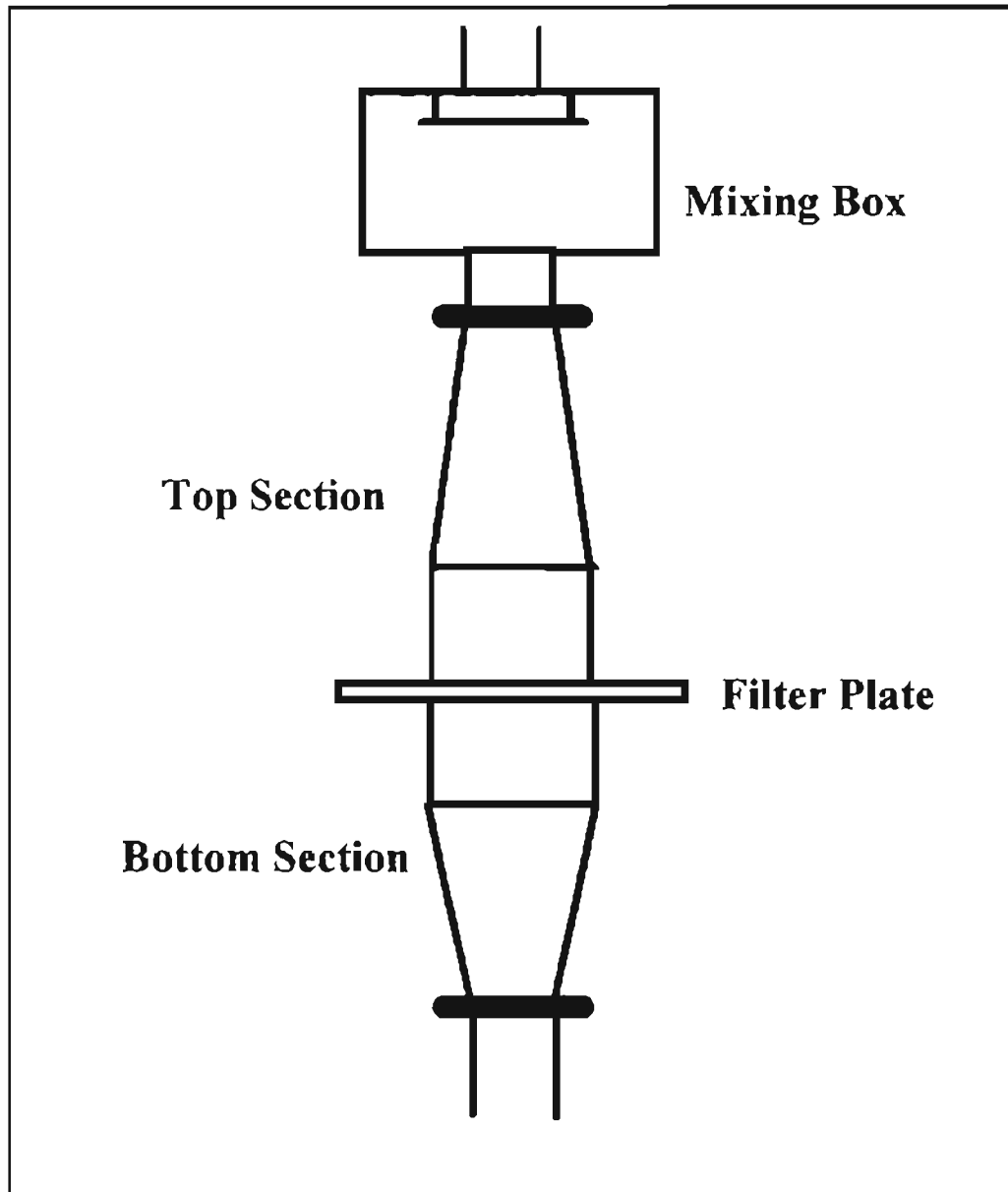


Figure 3.12 Schematic Assembly of Housing.

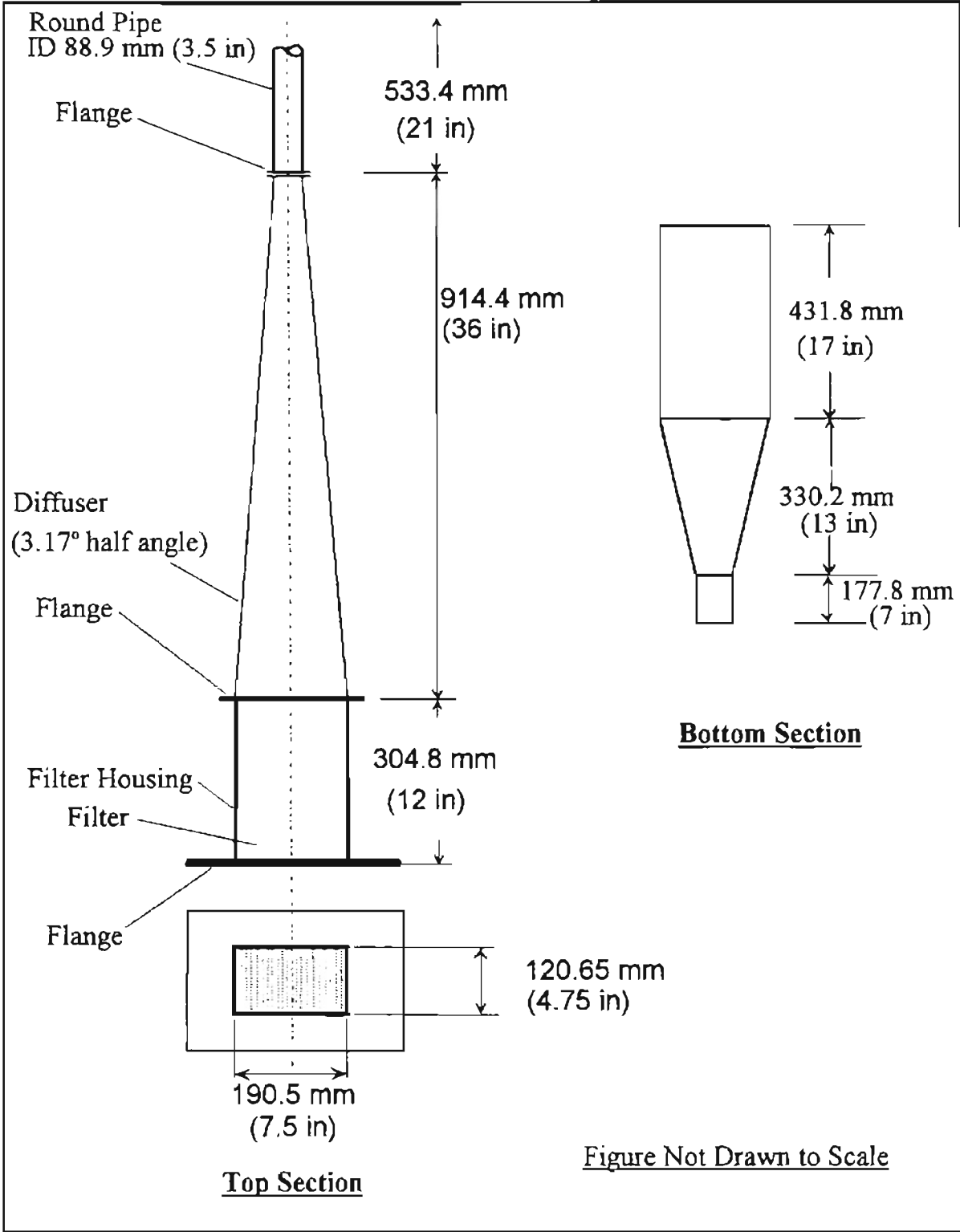


Figure 3.13 Small Angle Diffuser Housing.

Figure Not Drawn to Scale

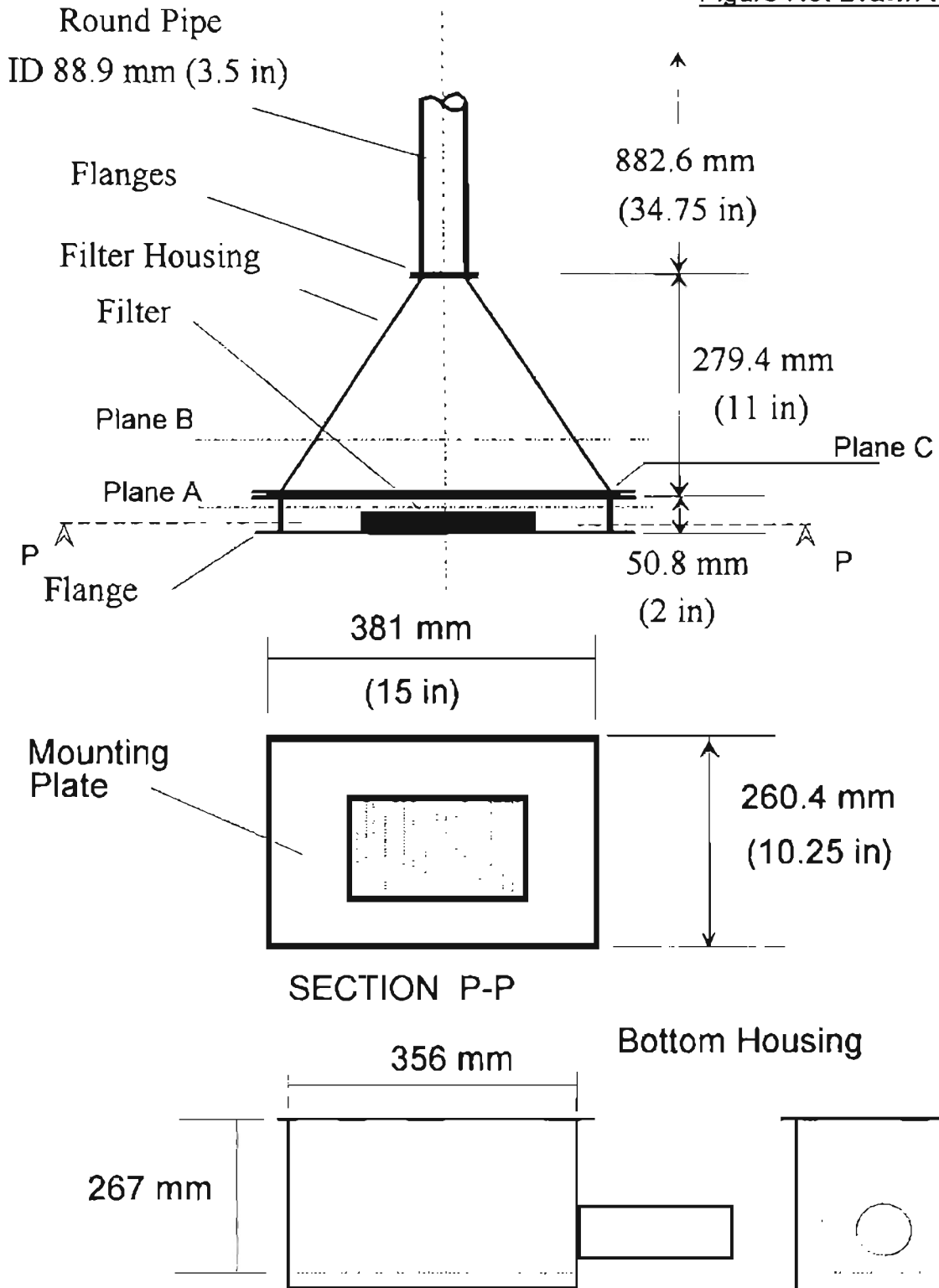


Figure 3.14 Schematic of SAE J726 Housing.

3.3.3 Filter Mounting

The filter is mounted on an aluminum plate which is placed between the flanges of the top and bottom halves of the housing. The aluminum plate has a rectangular hole in it with the internal dimensions of the housing. A wire mesh is placed over this opening and the flat filter is mounted over this mesh (see Fig. 3.15). The purpose of the mesh is to provide support to the filter media, especially when operating at high flow rates. The wire mesh and the filter are taped down to the aluminum plate. A compressible lining is placed along the edges of the opening on the plate as well as on the top and bottom halves of the housing. This helps to make the joint between the flanges air tight when clamped together.

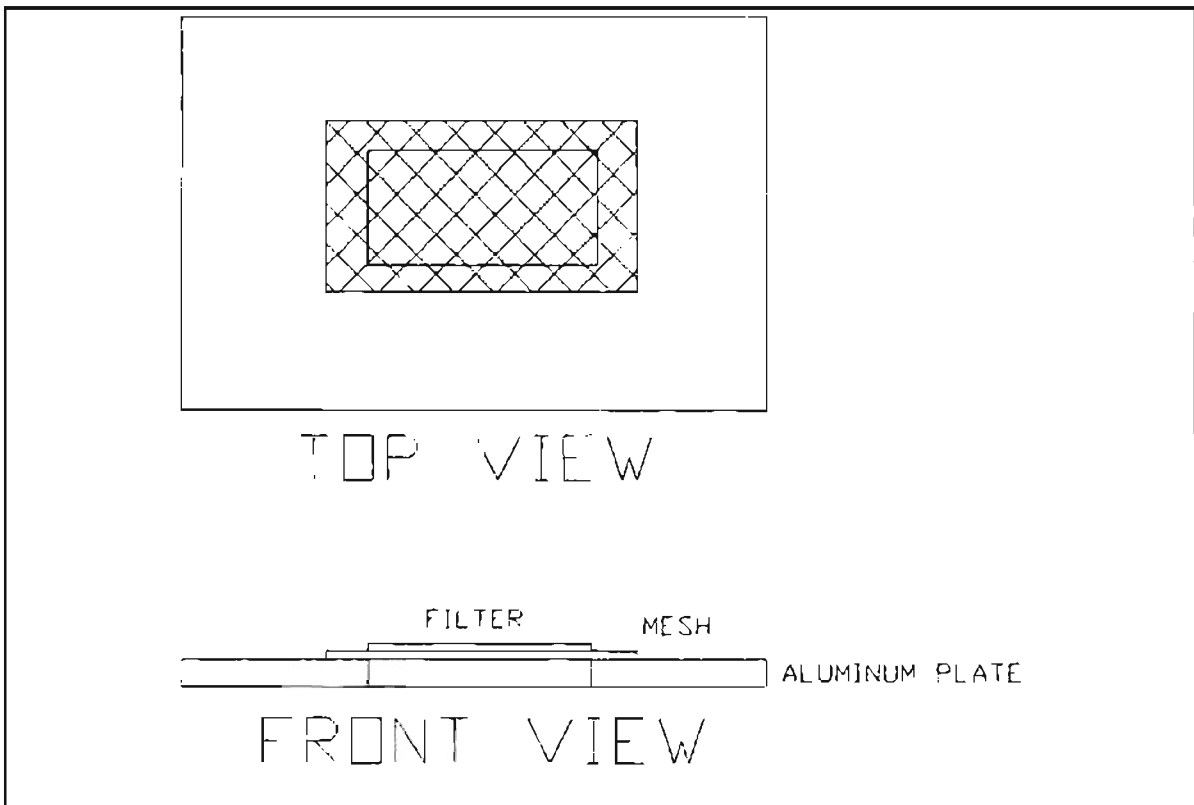


Figure 3.15 Filter Mounting Setup.

After the housing was clamped on to the supporting stand along with the mixing box, it was tested for leaks. The housing was pressurized to about 207 kPa (30 psi), and a soap solution applied to the housing to check for leaks. All of the leaks were plugged using a Plexiglas bonding agent.

3.3.4 Flow Generation and Measurement

The bottom half of the housing is connected to the SAE Purolator test stand blower via PVC pipes with a TSI flow meter (Model No. 2018) in line (see Fig. 3.11). The duct work is provided with three bypass valves after the TSI flow meter to control the flow rate. The flow is generated by the blower (constant flow rate) which can be bypassed to obtain flow rates varying from 42.75 m³/hr (25 cfm) to 855 m³/hr (500 cfm) inside the housing. For flow rates below 42.75 m³/hr (25 cfm), the additional bypass valves were used. These valves could reduce the flow rate to as low as 5.13 m³/hr (3 cfm).

The TSI flow meter has a heated flow sensing element and a temperature sensing element, both exposed directly to the flow. The flow sensor is of the hot film type and is sensitive to changes in temperature. The temperature compensation feature automatically compensates for the relatively slow changes in fluid temperature. The flow meter measures the standard flow rate in cfm based on a standard temperature of 25°C and a pressure of 1 atmosphere. To ensure that the flow meter measured the flow rates accurately, a calibration was done using a 1" diameter nozzle for flow rates from 0-85.5 m³/hr (0-50 cfm) (see appendix C).

CHAPTER IV

CONSISTENCY MEASUREMENTS

Repeatability and accuracy are essential in experimental research to validate the results. Previous researchers [Williams, 1996 and Natarajan, 1995] working on the same experimental setup had experienced difficulties with this aspect of their results. Williams performed some reliability tests on the setup. One such test involved measuring the number density at one grid location (center) for a certain period of time at constant laser power and then as a function of laser power. At constant laser power, the number density was observed to fall in a short period of twelve minutes. With variation in laser power, the number density was observed to vary considerably (see Fig. 4.1). Number density measurements were also made using different sample numbers on the DSA software (Section 3.2), and the lowest variation was observed for a value of 1000 samples which was $\pm 20\%$. Similar reliability tests performed by Natarajan showed better results but were still in an error range of $\pm 15\%$.

Both Williams and Natarajan attributed these errors to changing laser power, varying atomizing rate and flow rate variations, but they were unable to predict the exact influence of each of these factors. The effects of laser power and flow rate variation have been discussed in Chapter 3, and some changes were made to the flow setup and instrumentation to ensure their stability. To check the atomizer, some tests were

performed and will be discussed later in this chapter. This chapter will also review some of the other experiments done to check the system's accuracy and reliability. A stepwise approach was followed in this regard and these tests can be divided into three categories

- Open Flow Tests
- Particle Tests Inside the Housing
- Complete Filter Mesh Tests

In each of these tests, the consistency of the measurements with variation of the three major parameters (laser power, high voltage and threshold) was done.

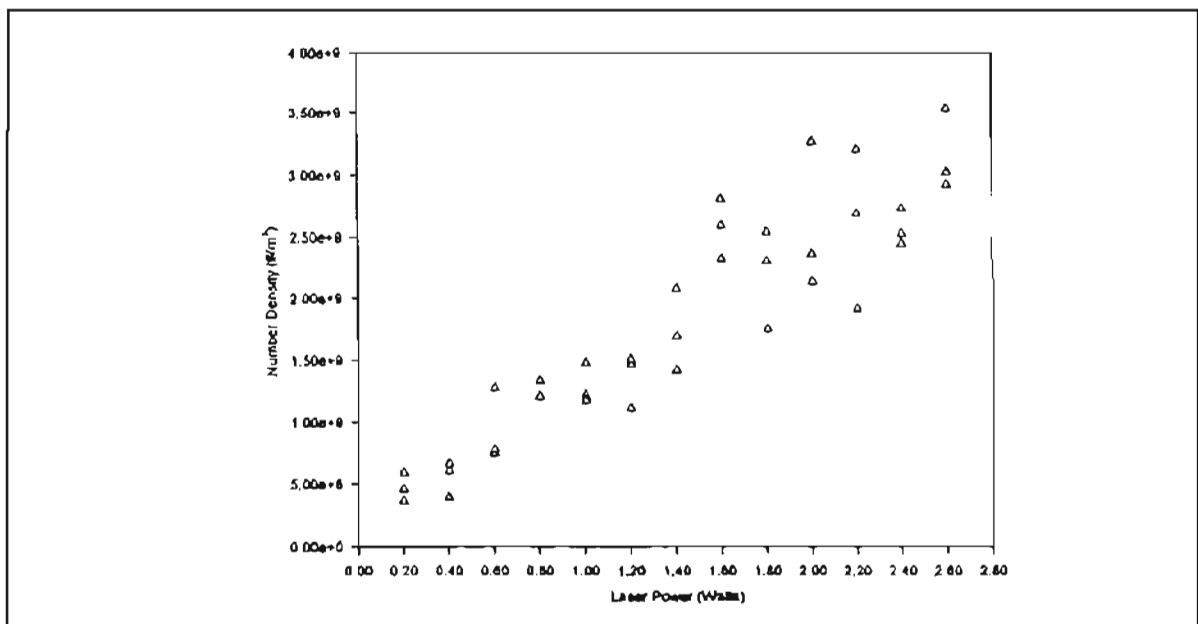


Figure 4.1 Particle Number Density at Center of Housing as a Function of Laser Power [Williams, 1996].

4.1 Open Flow Tests

In order to check the consistency of the atomizer, measurements were taken on a spray of water from the atomizer. This was an open flow into the air with no housing.

These tests were done to ensure that the atomizer was generating the spray at a steady rate. Also, these tests would examine the influence of the variations in high voltage, threshold and laser power on the data acquisition rate.

These tests monitored the sample rate or the number of counts per unit time instead of the number density, as the measurements were made at a single point and repeated measurements showed a constant velocity. Therefore, the variations in the sample rate are reflective of the changes in the number density. Some of these results are presented next. The sample rates have been normalized with the averages of the respective set in order to compare different sets. Figure 4.2 shows the normalized attempted and validated sample rates for different power settings. Each set is comprised of 30 runs, with each run taking approximately one minute. Thus, the entire test took about two hours.

Almost all of the data is within the $\pm 5\%$ range, which is an acceptable error. Change in laser power has little effect on the consistency (see Fig. 4.2 for data runs with different powers), but the actual sampling rate varies as shown in Fig. 4.3. There is a sharp rise in the average sampling rate for a power change from 0.4 W to 0.6 W (1000 to 1750 #/s); but beyond that the sample rate remains nearly constant (1750 to 2000 #/s), indicating that after a certain laser power, increase in power has no benefit. Most of the experiments in this study have been conducted using a laser power of 0.8 W. A plot of average sample rate with validity (Fig. 4.4) for the same experiment indicates a relatively flat profile for the validity values with respect to laser power.

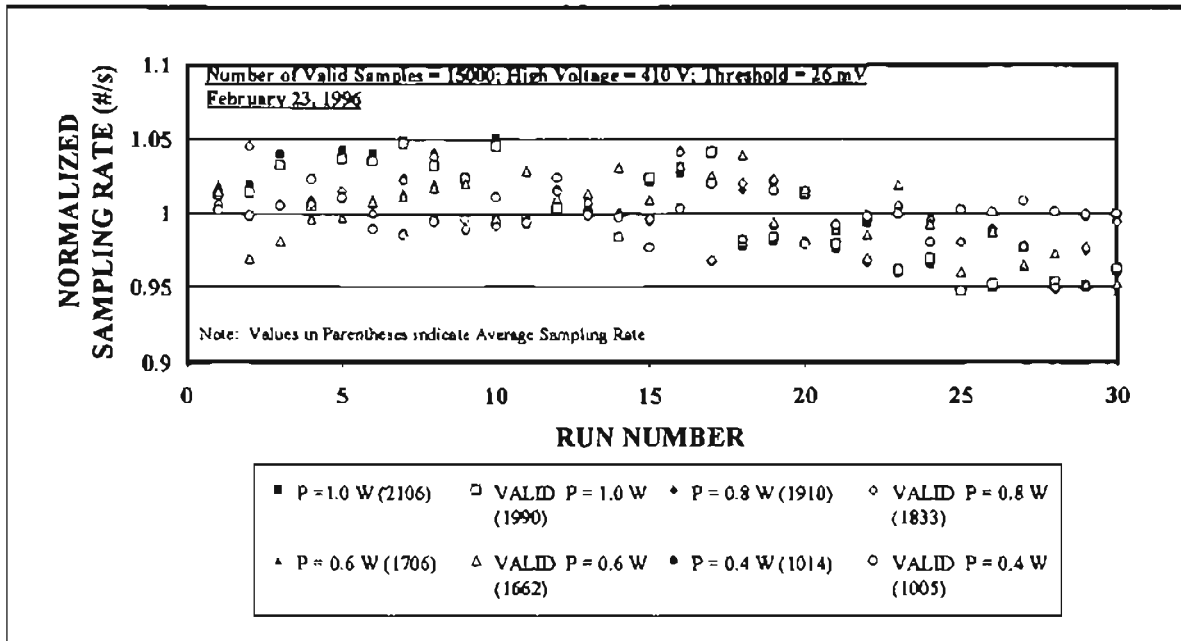


Figure 4.2 Atomizer Consistency as a Function of Laser Power (Open Flow).

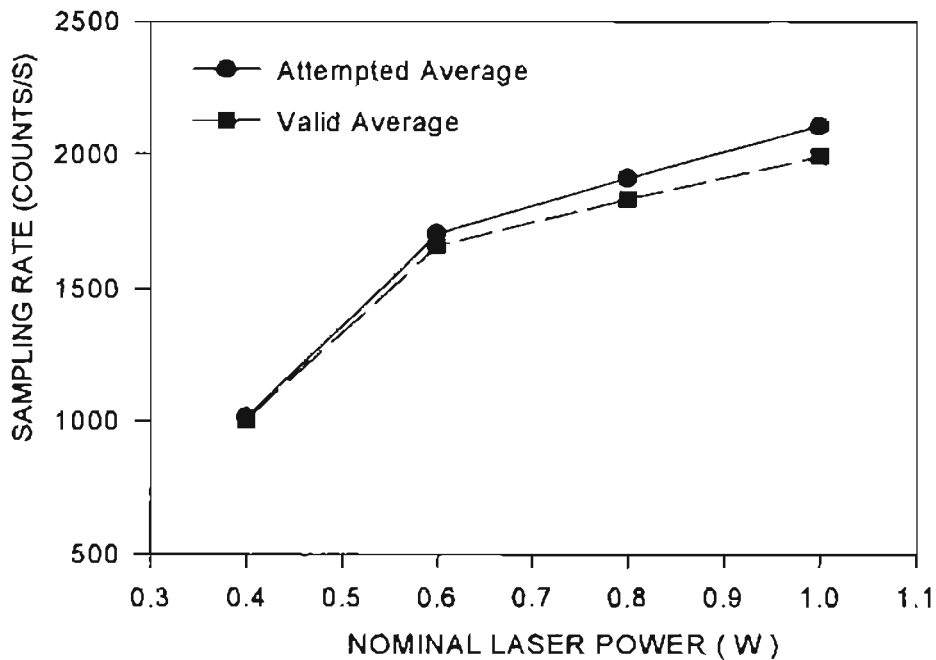


Figure 4.3 Influence of Nominal Laser Power on Sample Rate (Open Flow).

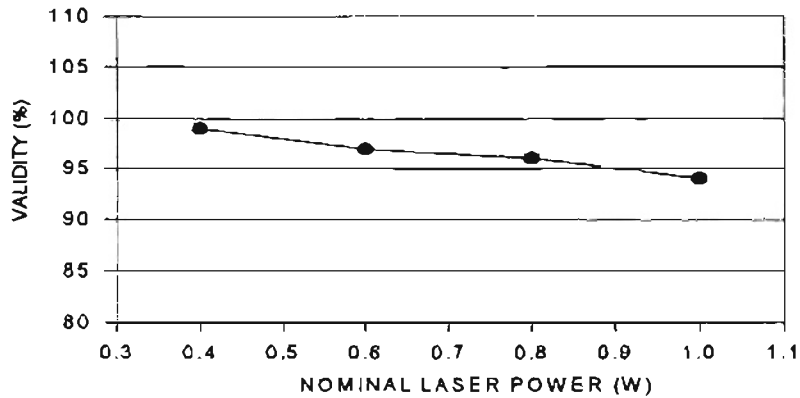


Figure 4.4 Influence of Nominal Laser Power on Validity (Open Flow).

The impact of high voltage and threshold on the sampling rate was discussed in detail in Chapter 3. The consistency of the data was also checked with respect to these DSA software parameters. Plots similar to Fig. 4.2 are shown in Figs. 4.5 and 4.6. They show the same bandwidth of $\pm 5\%$ for all of the data.

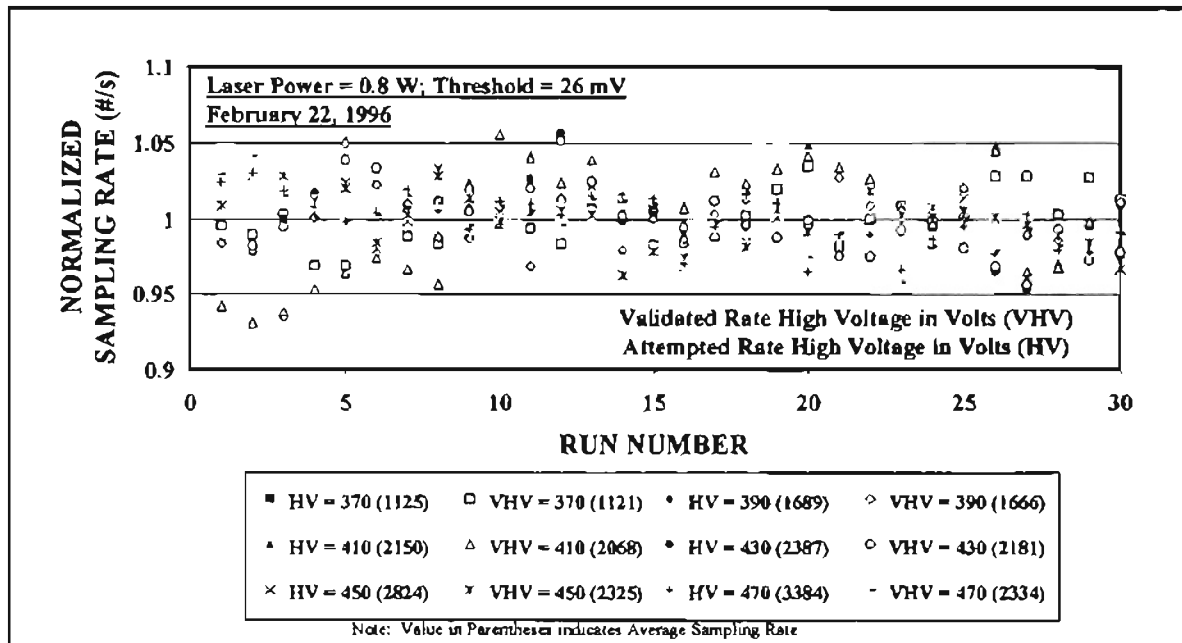


Figure 4.5 Consistency as a Function of High Voltage (Open Flow).

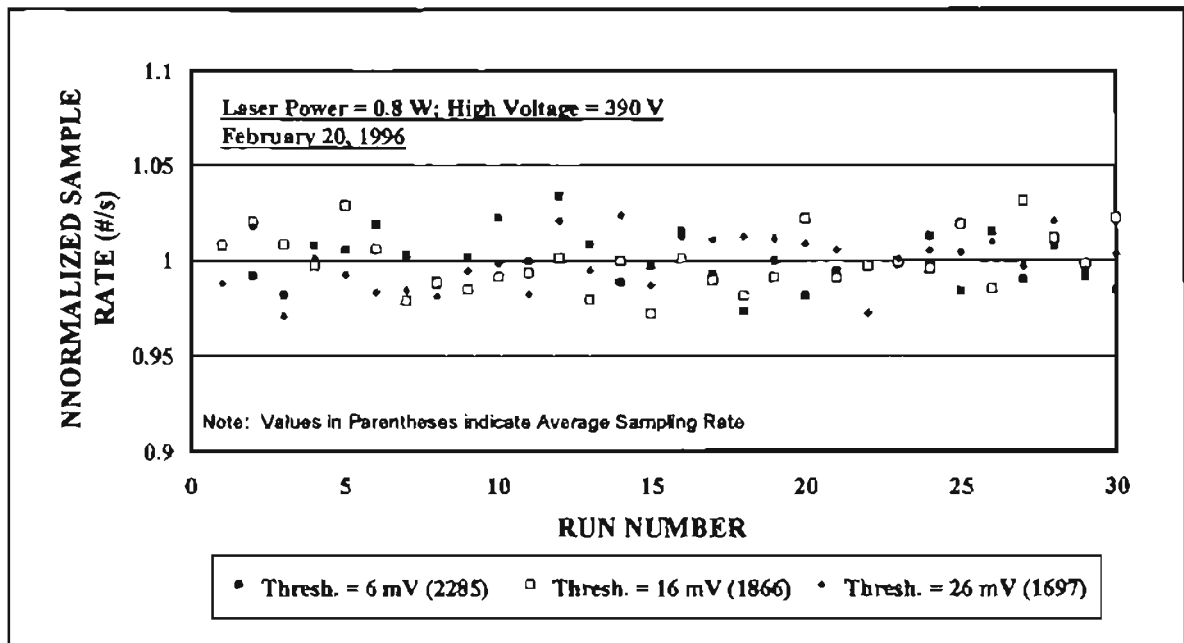


Figure 4.6 Consistency as a Function of Threshold (Open Flow).

These results on open flow helped build up confidence in the seeding rate of the atomizer which had been questioned by Williams and Natarajan but never proven.

4.2 Particle Tests Inside the Housing

Having proven the steady performance of the atomizer in an open flow situation, the next step was to test its performance inside the housing with actual PSL seeding particles. With this in mind, tests similar to one described in the preceding section were done inside the small angle diffuser housing. Measurements were made inside the housing at the center point location on the upstream side with no filter. Consistency with changing laser power, high voltage and threshold was observed. The results of these tests are shown in Figs. 4.7, 4.8 and 4.9.

The results show that most of the data in all three plots is within a $\pm 5\%$ bandwidth, and the complete data is within a $\pm 10\%$ bandwidth. Some of the points which lie outside the $\pm 5\%$ band are at a low power setting (0.4 W; Fig. 4.7), or a low high voltage (530 V; Fig. 4.8) or a low threshold (40 mV; Fig. 4.9). All of these tests were performed twice at a flow rate of 128.25 m³/hr (75 scfm). These results show that if the laser power and other DSA parameters are set in the correct range, the data acquired by the system is consistent, repeatable and reasonably accurate ($\pm 5\%$).

Another test was performed to check the consistency with time. This test was done at a flow rate of 128.25 m³/hr (75 scfm) with a 570 V high voltage, 60 mV threshold and 0.8 W laser power. This test took 50 runs instead of the 20 or 30 runs in the previous experiments which meant a total test time of about one hour. The results of this test are shown in Fig. 4.10 and conform to the $\pm 5\%$ bandwidth.

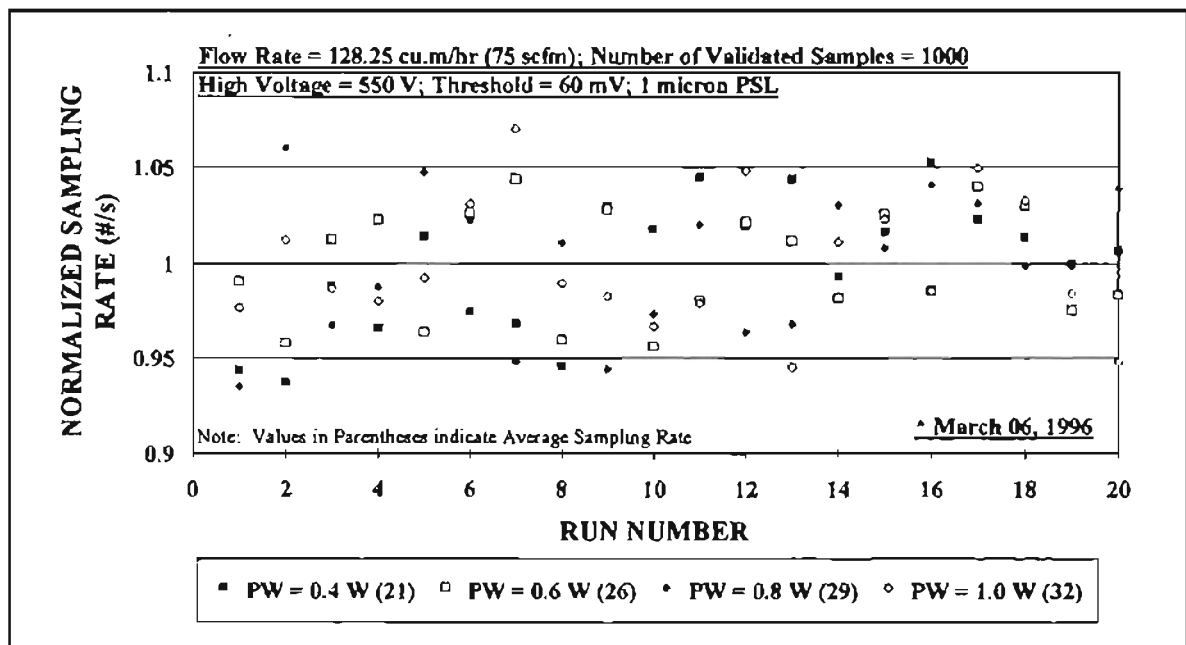


Figure 4.7 Consistency as a Function of Laser Power (Inside Housing).

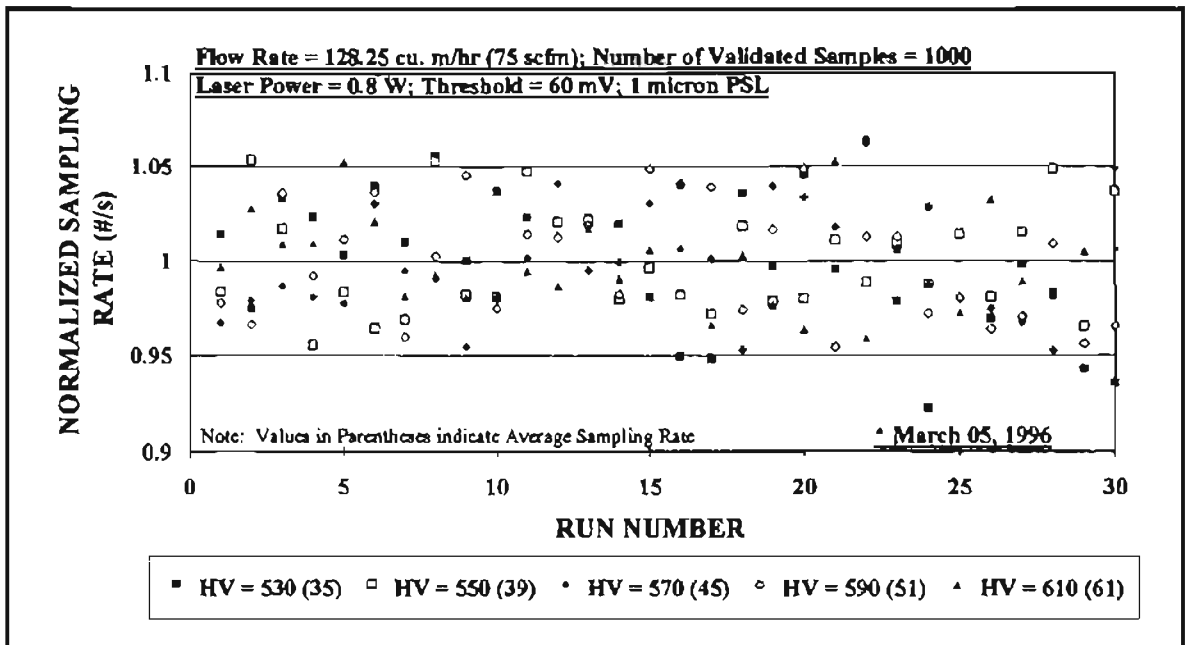


Figure 4.8 Consistency as a Function of High Voltage (Inside Housing).

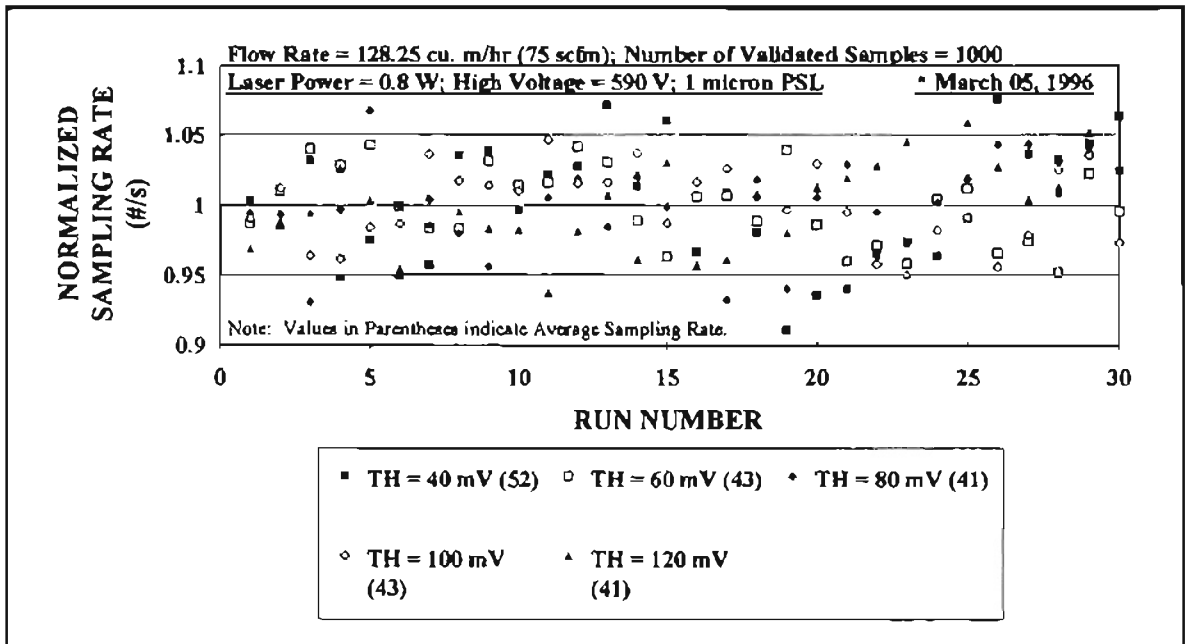


Figure 4.9 Consistency as a Function of Threshold (Inside Housing).

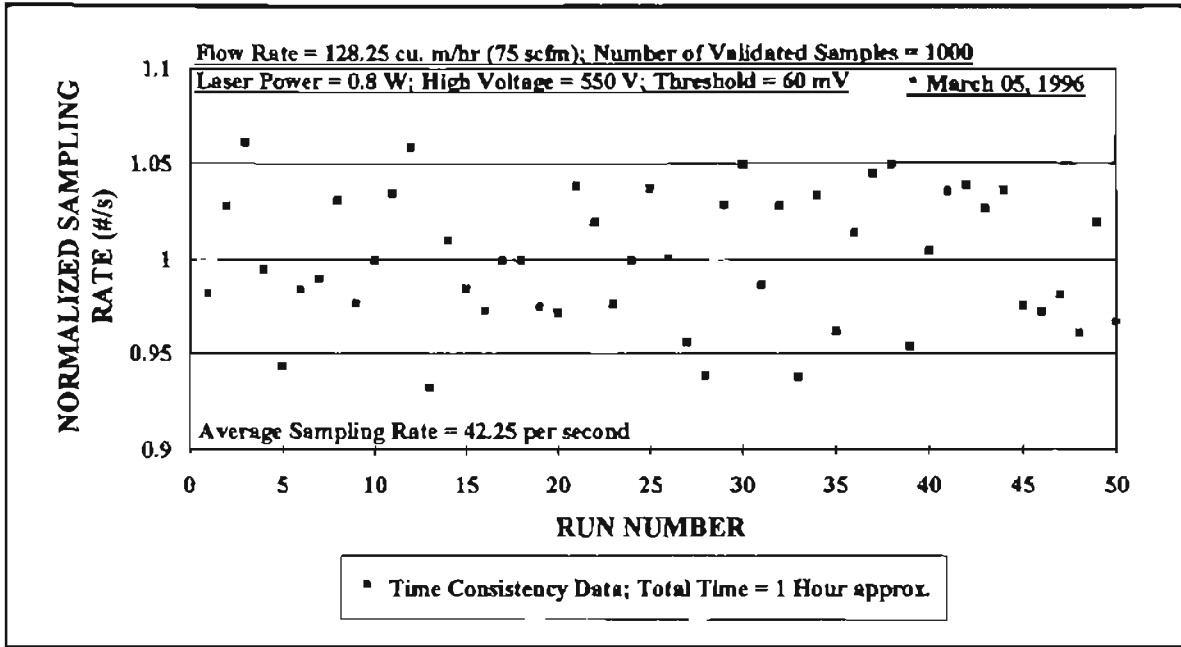


Figure 4.10 Time Consistency Measurement (Inside Housing).

An error of $\pm 5\%$ in the number density would mean a higher error in efficiency [Jadbabaei, 1997]. Equation (3-1) relates upstream and downstream number density values to filtration efficiency. The highest efficiency value will result if n_{down} is 5% lower and n_{up} is 5% higher while the lowest efficiency will result in the reverse case. If R_{nd} is the ratio of downstream to upstream number density then

$$\eta = 1 - R_{\text{nd}} \quad (4-1).$$

$$\eta_{\text{max}} = 1 - \frac{0.95}{1.05} R_{\text{nd}} \cong 1 - 0.9 R_{\text{nd}} \quad (4-2)$$

and

$$\eta_{\text{min}} = 1 - \frac{1.05}{0.95} R_{\text{nd}} \cong 1 - 1.1 R_{\text{nd}} \quad (4-3)$$

Equations (4-2) and (4-3) show that the actual error will depend on the ratio R_{nd} . For example, for 50% filtration efficiency, $R_{nd} = 0.5$. Therefore the error in efficiency will be $\pm 5\%$ (absolute efficiency; i.e., efficiency will be between 45% and 55%) according to Eqs. (4-2) and (4-3). Higher efficiencies will show lower errors as R_{nd} is lower and vice versa. The maximum error of $\pm 10\%$ will occur at 0% filtration efficiency, as $R_{nd} = 1.0$. To confirm this, a set of 5 tests were performed to obtain filtration efficiency with no filter. Number density measurements were performed upstream and downstream alternately at the center point of the filter grid 30 times for each test. The efficiency values for these tests fell within the predicted $\pm 10\%$ band, with the average efficiency values close to zero. The worst and best cases are shown in Figs. 4.11 and 4.12. A more detailed error analysis is shown in Appendix E.

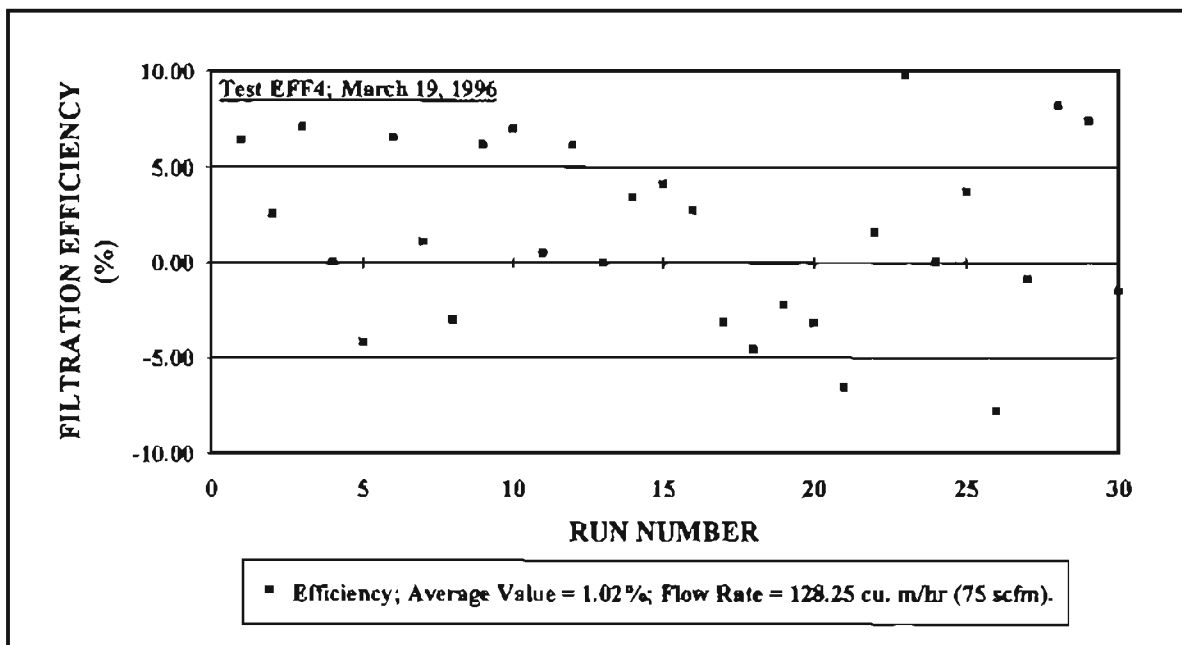


Figure 4.11 Filtration Efficiency at Center Line for No Filter (Worst Case).

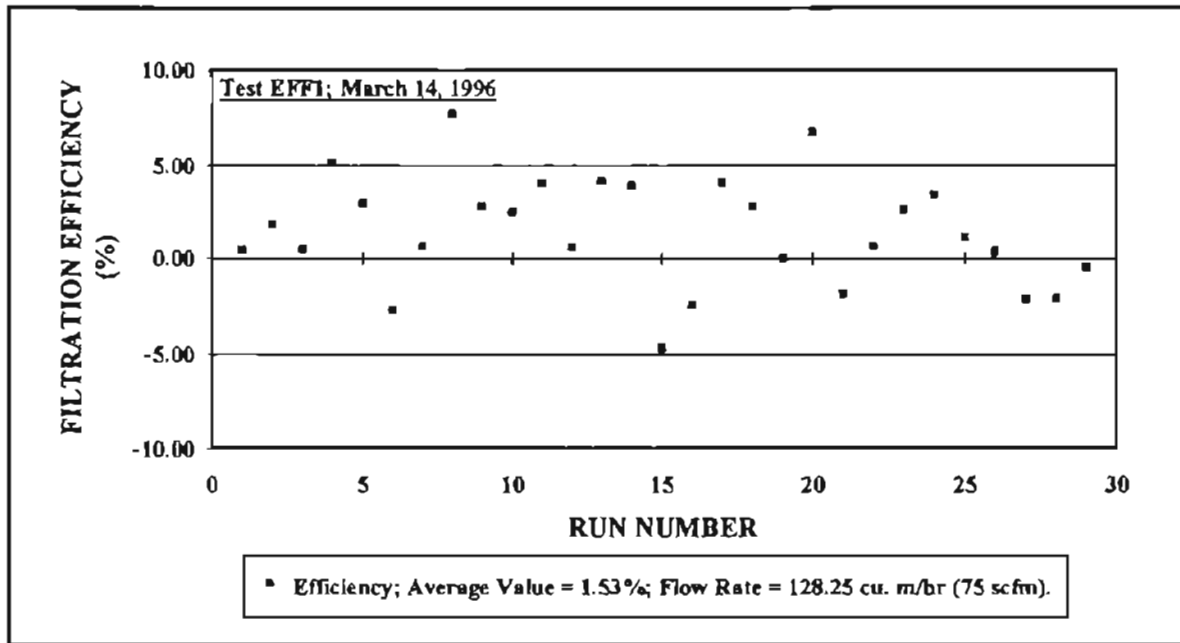


Figure 4.12 Filtration Efficiency at Center Line for No Filter (Best Case).

Another test which was performed to check the consistency of the atomizer inside the housing was to measure the number densities with varying solution concentrations at the center of the filter plane without a filter. The plot of the results in Fig. 4.13 shows a relatively straight line correlation indicating that the atomizer seeding rate and the instrumentation are accurate.

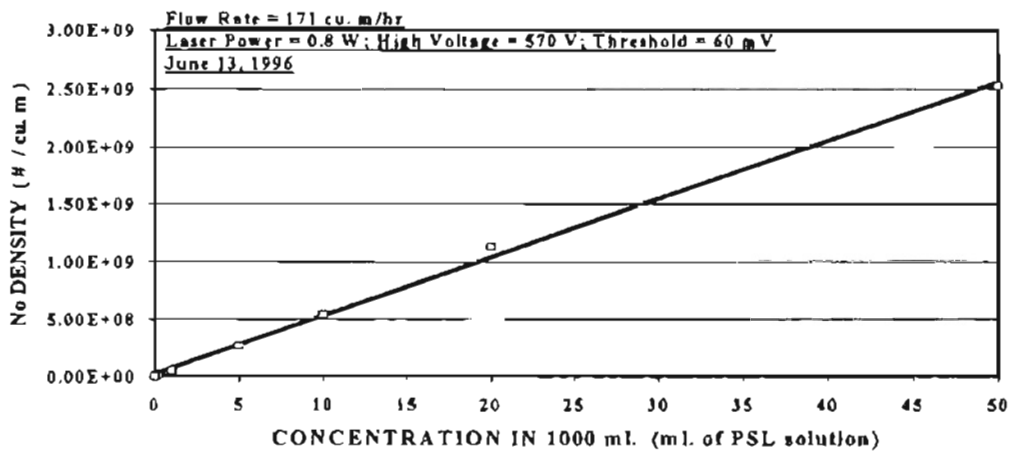


Figure 4.13 Number Density for Different Solution Concentrations.

4.3 Complete Filter Mesh Tests

The final step in checking the consistency of the setup was to make filtration efficiency measurements over the entire 7 x 5 grid (Fig. 3.1) with no filter inside the housing. An average efficiency close to zero would prove that the system was capable of making reasonably accurate measurements. Before attempting to review any of these test results, an explanation of the detailed experimental procedure is required.

4.3.1 Detailed Experimental Procedure

In order to perform the experiments, a set procedure was developed and followed for obtaining all of the data in this study. The steps included:

1. The room temperature was brought to the stable alignment temperature (by either heating or cooling) and the laser and the LDV system were powered up.
2. The flow setup was assembled with a new filter media (as explained in Section 3.3) and the computer controlled three-dimensional traverse was powered up along with its software.
3. The probe volume was brought to the center line position of the housing by moving the traverse.
4. About 500 to 800 ml. of the PSL solution of the desired concentration was prepared and placed in the atomizer. The atomizer was then placed in the flow stream, and a compressed air hose was connected to it (Fig. 3.1).
5. The blower was powered up, and the flow rate was adjusted to the desired value.

Next the heater used to evaporate the water particles from the atomized spray was powered up.

6. A note of the initial pressure drop was made from the inclined manometer connected to the flow setup.
7. The compressed air flow to the atomizer was opened and the pressure, and air dilution rates on it were set.
8. The parameters on the DSA software were set as discussed in Chapter 3.
9. To take the data, a standard format MS-Excel file was developed instead of dumping data on the hard disk and processing it later. This gave the advantage of the test being monitored closely and efficiency values being obtained on-line. No significant time loss occurred due to this procedure, as the major time spent in a complete test was the time taken to move the traverse from one location to another. At each grid location, either upstream or downstream, three number density measurements were made and averaged out to get the value used to determine the efficiency. Also, on the Excel file, the nominal laser power, the laser power of each beam, the high voltage, threshold, the atomizer pressure, the test date and time, the flow rate, the pressure drop values at beginning and end of a test, the solution consumed and the total test time were recorded.
10. To make measurements, the traverse was moved to an upstream location for a grid point, then to the downstream position of the same grid location followed by the downstream position of the next grid location, and so on.

4.3.2 Filter Mesh Results

Two tests with no filter were made on the entire grid. The grid spacing for these tests was 19.05 mm x 19.05 mm (0.75" x 0.75"). The results for these tests named MESH32 and MESH33 are shown next.

The efficiency plot (Fig. 4.14) for test MESH32 indicates a variation of $\pm 5\%$, although the value calculated from Eq. (4-1) is $\pm 10\%$. The average value of the efficiency is -0.39% which is very close to the expected value of zero. The number density plots for the upstream and downstream position are shown in Fig. 4.15 and Fig. 4.16, respectively. The variations in these number densities from the average for each plane were calculated to be in the range of $\pm 10\%$. This variation is higher than that seen for the center line measurements earlier. This higher value can be explained by the fact that the flow does not have a flat profile across the housing, and these variations in the flow could have resulted in non-uniformities in the number density values.

Similar plots for efficiency, and upstream and downstream number densities for test MESH33 are shown in Fig. 4.17, Fig. 4.18 and Fig. 4.19, respectively. These plots have trends similar to the ones for test MESH32. For test MESH33, the average efficiency is -0.22% , while the upstream and downstream number densities vary within almost $\pm 10\%$.

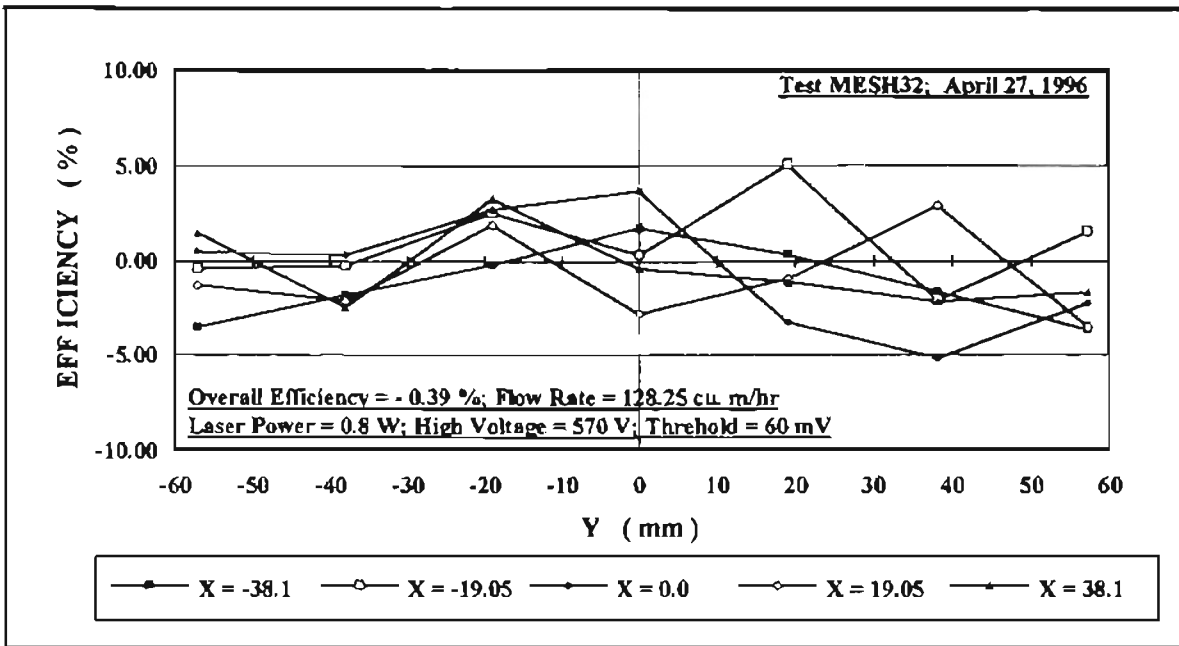


Figure 4.14 Local Efficiency Plot with No Filter (Test MESH32).

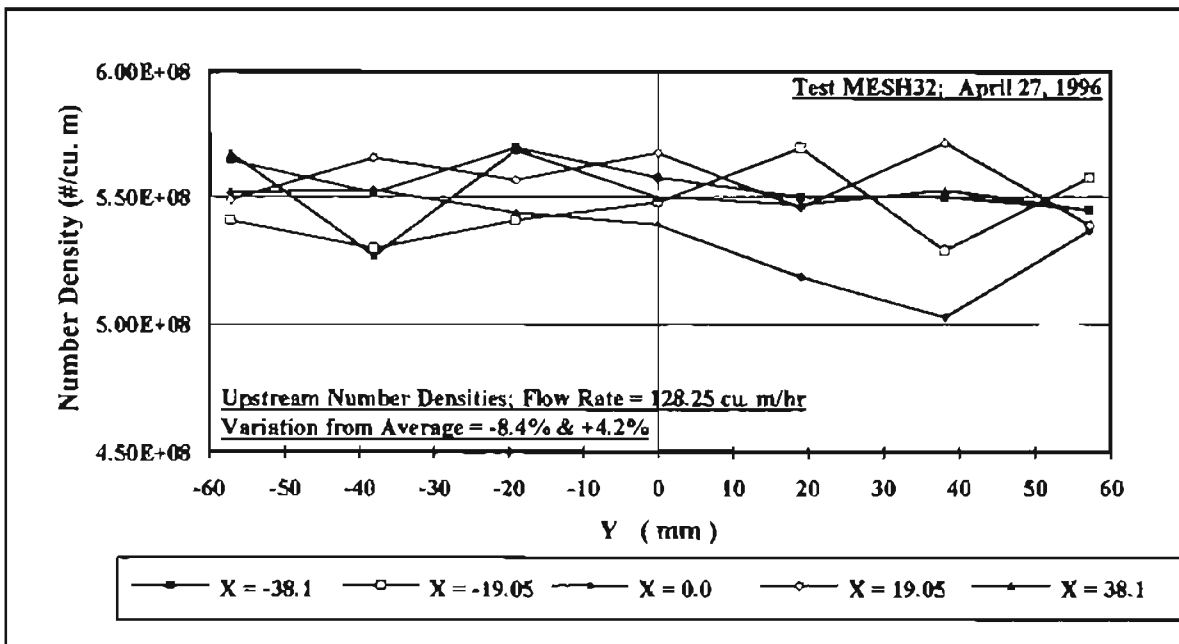


Figure 4.15 Local Upstream Number Density Plot with No Filter (Test MESH32).

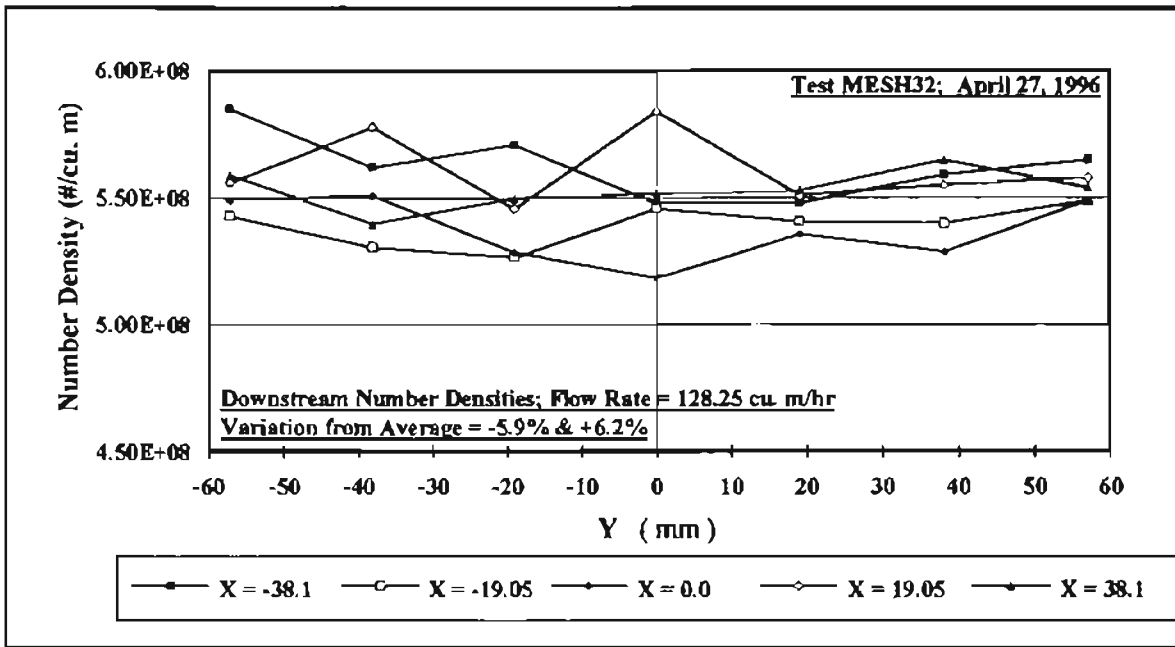


Figure 4.16 Local Downstream Number Density Plot with No Filter (Test MESH32).

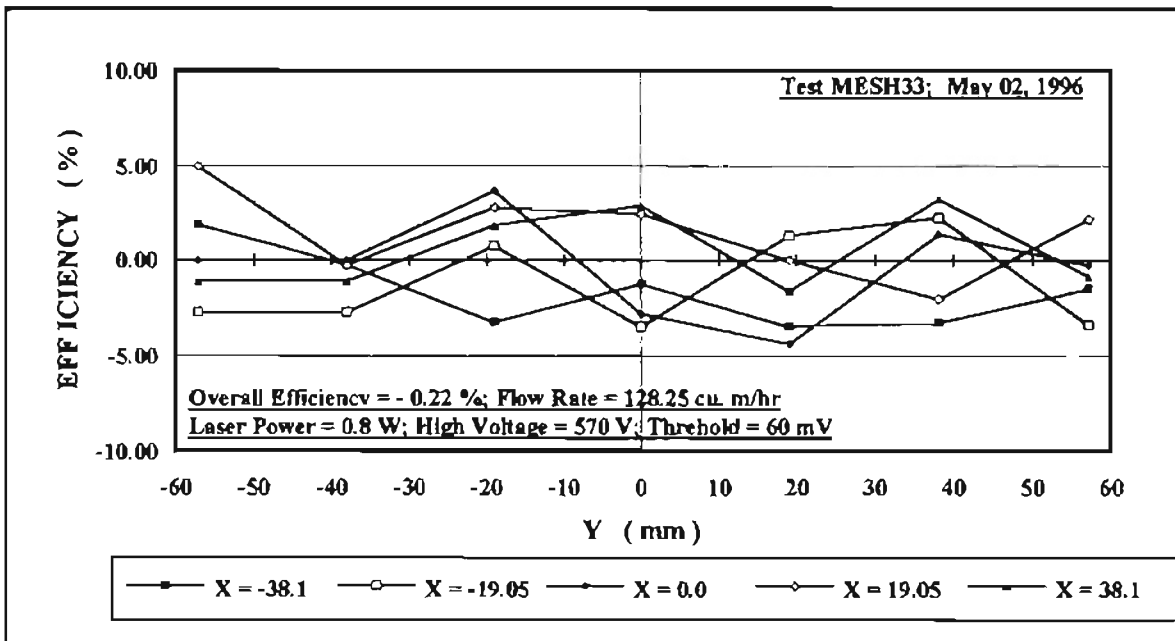


Figure 4.17 Local Efficiency Plot with No Filter (Test MESH33).

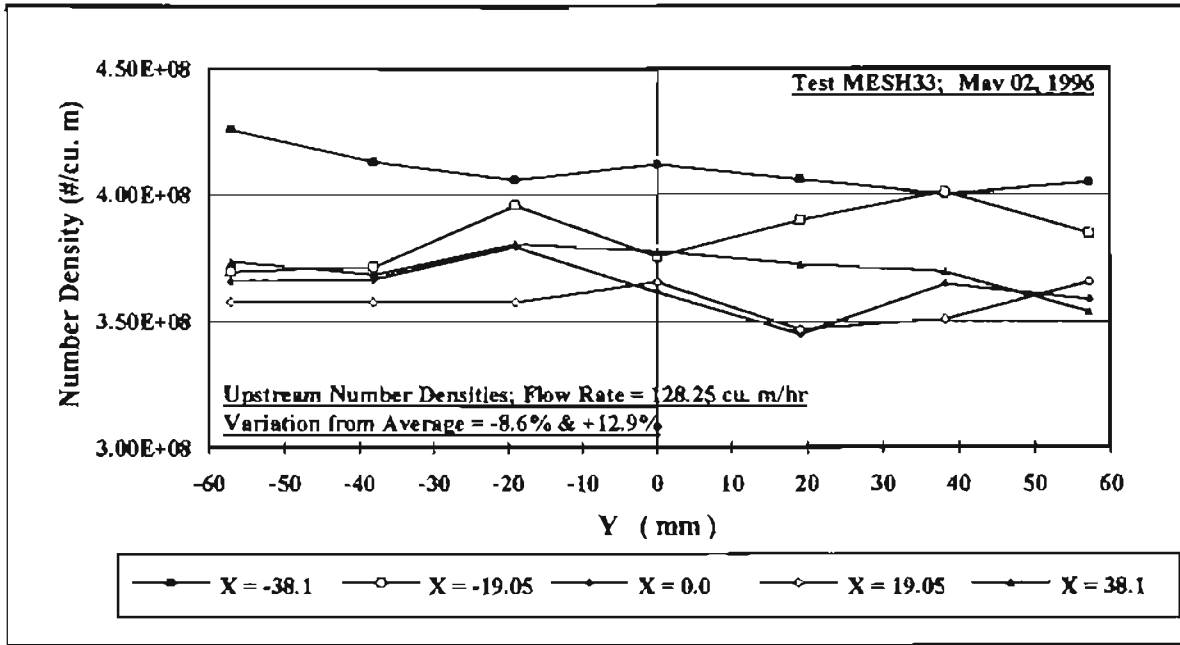


Figure 4.18 Local Upstream Number Density Plot with No Filter (Test MESH33).

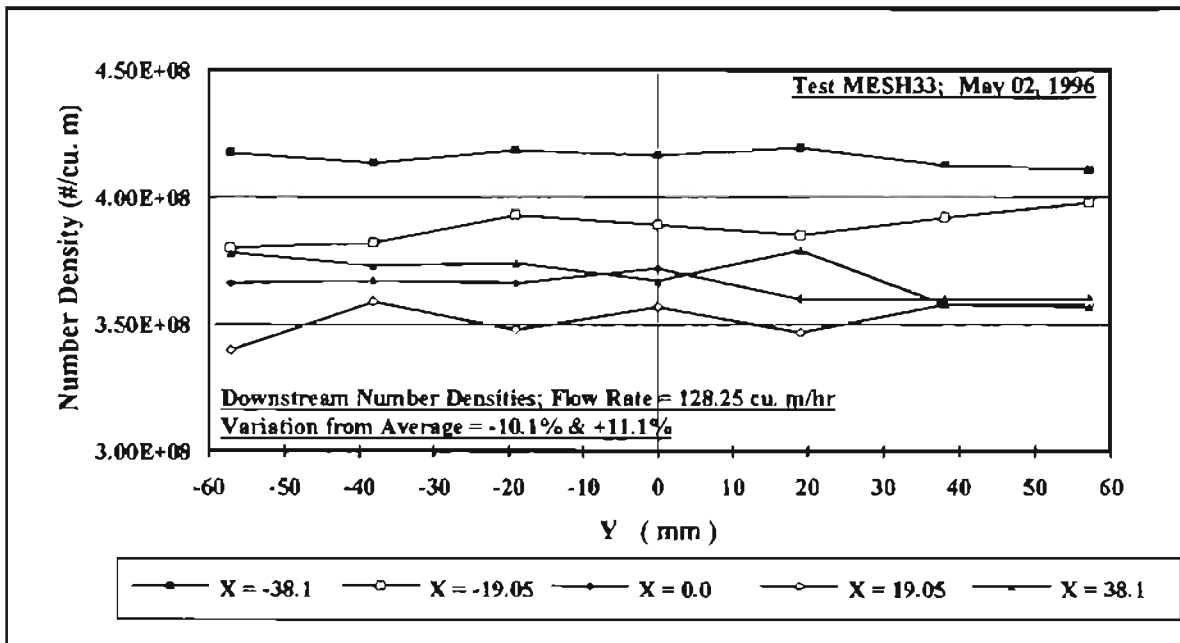


Figure 4.19 Local Downstream Number Density Plot with No Filter (Test MESH33).

CHAPTER V

RESULTS AND DISCUSSION

5.1 Overview

In an effort to compare the results of this study with the pleated filter results of Jadbabaei [1997], filter efficiencies at various flow rates needed to be determined. Since, particle size was kept constant, variation in Stokes number could be achieved by varying the flow velocity or in effect the flow rate. All data for the present study was collected using the experimental setup described in Chapter 3. The reliability and accuracy of the instrumentation used for making the measurements was ensured by performing the series of tests outlined in Chapter 4. This chapter aims at explaining the results obtained from a final series of experiments.

The experiments for the present study were conducted over a flow rate range of 2.51 to 92.93 m³/hr which was closely monitored by a TSI flow meter. The actual test flow rates were 2.51, 5.68, 13.61, 21.54, 29.48, 45.34, 61.20 and 92.93 m³/hr. Except for the flow rate of 2.51 m³/hr, all other flow rates were tested twice (or more) to confirm the repeatability of the tests. The 2.51 m³/hr flow rate setting was presumed to be suspect because the flow meter could not be calibrated at that flow rate (Appendix C).

The data was collected over the 5 x 7 grid shown in Fig. 5.1. Since the flow rates were low, and the total filter area small, clogging of the filter media due to particle

deposition would be a big influence on the measurements. The data acquisition time was high because efficiency at all of the 35 grid locations had to be determined. The number of samples collected at each grid location was anywhere from 200 to 1000 with three such measurements being recorded at all the locations. The lower sample counts were taken to reduce the data acquisition time and prevent deposition on the filter (though the statistical average over a smaller sample count of 200 would be less accurate than that for a higher sample count of 1000).

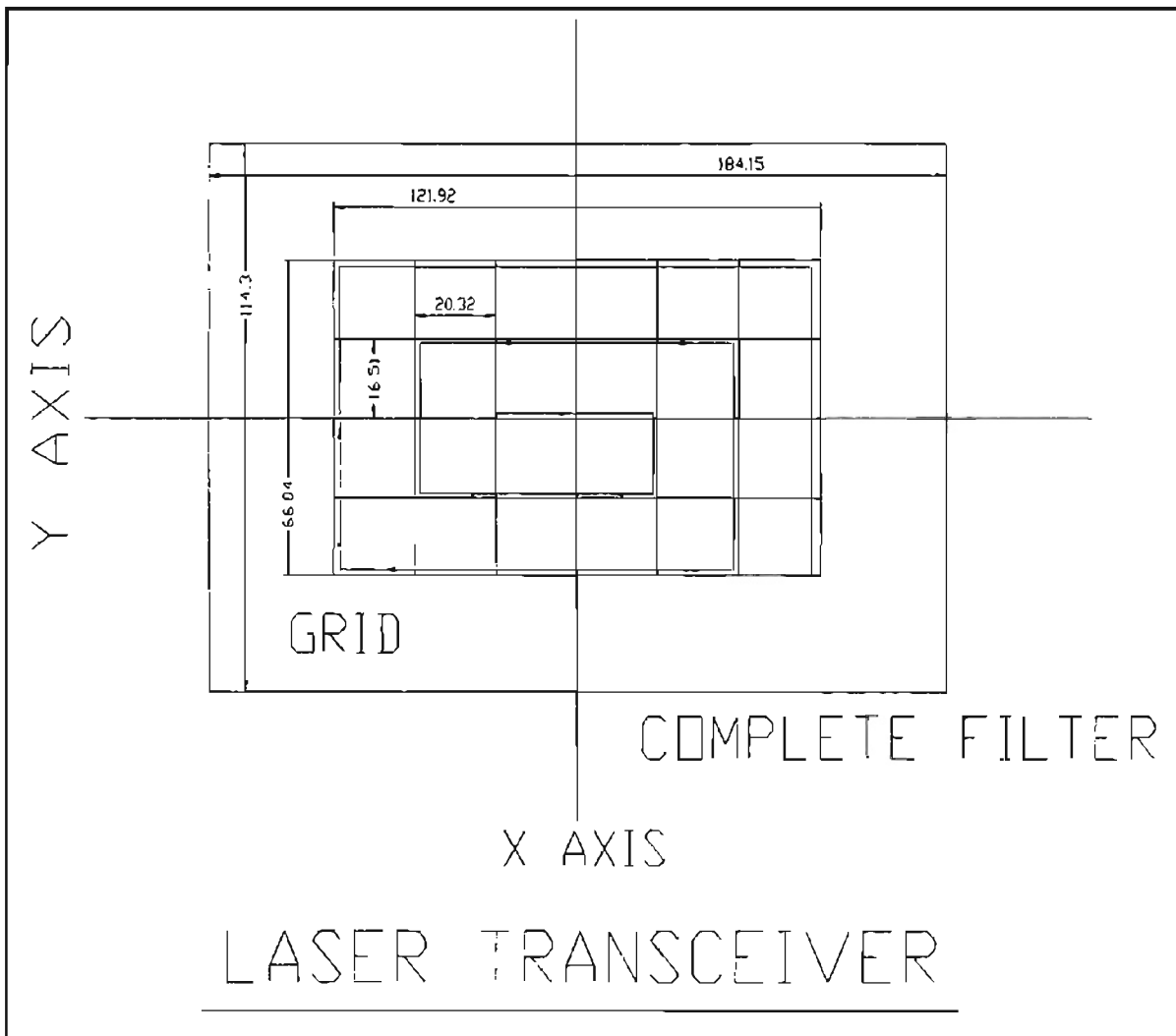


Figure 5.1 Grid Points on the Filter with the Measurement Grid Sequence.

Since the filter clogging would affect the number densities on the bottom side only, the entire downstream side was measured first. Consistency measurements explained in Chapter 4 indicate that the instrumentation remained stable over time to make accurate measurements in this fashion. This took anywhere from 30 to 45 minutes depending on the flow rate. The data collection on the downstream side was done in a typical inside out configuration shown in Fig. 5.1. This was done to collect the clean filter data around the central region of the grid, which had a more uniform velocity profile. The results show that this particular data collection procedure did not influence the results drastically, although a small bias in efficiency measurements between the central and edge grid points is observed in some cases.

The pressure drop during the entire test was carefully monitored and the pressure drop values at the start of seeding, beginning and end of data acquisition on the downstream plane and at the end of the data acquisition on the upstream plane were recorded. The critical pressure drop change here is the one between the beginning and end of the downstream side as it would indicate the extent to which the data was influenced by filter clogging. At flow rates of 21.54 and 45.34 m³/hr, the number density on the downstream plane was measured twice, once at the beginning and then after measuring the upstream plane. This was done to quantify the effect of pressure drop change on the filtration efficiency measurements.

The local efficiency, upstream and downstream velocity, and the upstream and downstream number densities were plotted for each test and some of the typical ones will be presented in this chapter. Also, the composite results of overall efficiency versus flow

rate and Stokes number will be presented and compared to the flat media results of Williams [1996] and Lee [1977] and to the pleated filter results of Jadbabaei [1997].

5.2 Flat Filter Results

The complete results are summarized in Tables 5.1 and 5.2. This section will investigate the trends in the velocities, number densities and efficiencies. Flow rates of 5.68, 21.54 and 92.93 m³/hr (corrected values) have been chosen as samples for discussion purposes. Table 5.1 shows the test name, the test date, the flow rate, the relative humidity (in the laboratory), the number of samples measured on the upstream and downstream side, the concentration of PSL solution used (ml of PSL solution in 1000 ml of distilled water), the average upstream and downstream number densities, the pressure drop changes during the test and the overall efficiencies for each experiment. Table 5.2 shows the Stokes number for each experiment calculated from the corrected flow rate (see Appendix C for TSI flow meter calibration results) and the average measured upstream velocity. All local measurement results in this chapter have been referred to by the corrected flow rates. The overall results presented in this chapter have also been corrected in accordance with the flow meter calibration results to reflect their true nature.

5.2.1 Measured Velocities

The velocities are summarized in Table 5.2. It shows the velocities calculated from the flow rate by uniformly distributing it over the entire filter sheet whose dimensions were 114.30 mm x 184.15 mm (4.5" x 7.25"). It also gives the average velocities

measured upstream and downstream of the filter (average of the 35 grid locations). The average upstream velocities are less than those calculated from the corrected flow rate. This is because the grid points measure the velocities over the central region, neglecting the regions close to the housing walls where the velocities are lower. The grid covers an area of 82.55 mm x 142.24 mm (3.25" x 5.6"). Thus, measurements cover only 55 % of the area. Measurements were made on this grid to have similarity with the pleated filter results of Jadbabaei [1997] for comparison. Because of the rubber edging on the lower side of the pleated filter, the grid had to be restricted to these values in that study.

The average upstream velocities ranged from 0.086 m/s to 1.536 m/s while the velocities on the downstream side ranged from 0.064 to 1.290 m/s. The downstream velocities were lower than the upstream values. This could be due to the redistribution of the velocity field by the filter media. A look at the individual velocity plots shows that the upstream velocity profile is flat with a slightly higher values at the center as expected (see Figs. 5.2, 5.3, and 5.4). Figure 5.5 shows a three-dimensional plot of the velocity profile. A closer look at all of these figures reveals that this profile is better observed for the higher flow rates. For flow rates from 2.51 to 13.61 m³/hr (see Fig. 5.3), the velocity is still closely banded but does not indicate a drop towards the walls. The downstream velocities do not show a specific trend but are still banded together (Figs. 5.6, 5.7 and 5.8). The velocity resolution for the velocities measured with the LDV system is 0.001 m/s. This can be calculated by converting the frequency resolution (obtained from the Aerometrics manual) to the equivalent velocity resolution by multiplying with fringe width.

Table 5.1 Complete Test Results

No.	Test Name	Test Date	Flow Rate (m ³ /hr)	RH (%)	No. Of Samples (#)		Sol. Conc. (ml)	Average No. Density (#/m ³)		Pressure Drop (mm of water)				Pressure Drop Change (mm of water)		η (%)
					Up	Down		Up	Down	Start Test	Start Down	End Down	End Test	Total	Down	
1	FLT22	08/22/96	2.51	50.2	300	300	1.3	1.21E+10	1.04E+10	2.040	2.040	2.040	2.040	0.000	0.000	13.78
2	FLT16	08/16/96	5.68	52.6	500	500	2.5	1.49E+10	1.26E+10	3.060	3.315	3.315	3.315	0.255	0.255	15.56
3	FLT17	08/19/96	5.68	54.6	1000	500	5.0	1.95E+10	1.65E+10	2.805	2.805	2.805	3.060	0.255	0.000	15.42
4	FLT14	08/15/96	13.61	47.4	1000	500	5.0	1.29E+10	9.76E+09	5.865	5.865	6.885	9.690	3.825	1.020	24.24
5	FLT15	08/16/96	13.61	52.8	500	400	2.5	7.77E+09	6.36E+09	4.845	5.355	5.610	6.375	1.530	0.765	18.00
6	FLT18	08/19/96	21.54	54.6	1000	500	5.0	6.79E+09	3.91E+09	8.670	9.690	11.730	22.695	14.025	3.060	42.38
7	FLT19	08/20/96	21.54	52.4	1000	500	5.0	8.17E+09	3.56E+09	9.690	10.710	15.300	34.425	24.735	5.610	56.30
8	FLT20	08/20/96	21.54	50.2	500	400	2.5	4.85E+09	3.59E+09	9.435	9.435	10.455	13.260	3.825	1.020	25.83
9	FLT21	08/20/96	21.54	50.2	500	300	2.5	4.85E+09	2.14E+09	9.435	13.260	14.535	14.535	5.100	5.100	55.80
10	FLT02	07/22/96	29.48	48.1	500	200	5.0	3.37E+09	1.53E+09	14.025	N/A	N/A	16.575	2.550	N/A	54.50
11	FLT03	07/26/96	29.48	46.4	500	250	5.0	3.57E+09	1.66E+09	14.025	N/A	N/A	28.050	14.025	N/A	53.46
12	FLT11	08/14/96	45.34	51.4	1000	300	5.0	3.15E+09	9.56E+08	21.930	21.930	28.305	41.310	19.380	6.375	69.54
13	FLT12	08/15/96	45.34	49.6	1000	300	5.0	3.07E+09	8.56E+08	22.185	24.225	28.560	39.525	17.340	6.375	71.97
14	FLT13	08/15/96	45.34	51.4	1000	200	5.0	3.07E+09	3.49E+08	22.185	39.525	47.430	47.430	25.245	25.245	88.60
15	FLT04	07/29/96	61.20	46.4	500	200	5.0	7.39E+08	1.58E+08	33.150	33.150	40.640	40.800	7.650	7.490	78.54
16	FLT05	07/29/96	61.20	47.9	300	200	5.0	8.42E+08	1.41E+08	32.895	32.895	35.955	39.270	6.375	3.060	83.19
17	FLT09	08/13/96	92.93	46.0	1000	200	5.0	1.56E+09	1.52E+08	53.550	53.550	56.100	66.300	12.750	2.550	90.24
18	FLT10	08/13/96	92.93	46.3	1000	200	5.0	1.52E+09	1.85E+08	53.805	56.610	61.965	72.675	18.870	8.160	87.71

Table 5.2 Stokes Number Analysis

No.	Test Name	Test Date	Flow Rate (m ³ /hr) (as shown on flow meter)	Flow Rate (m ³ /hr) (Corrected by flow meter calibration)	Velocity (m/s)			Stokes Number Calculated From		Efficiency (%)
					(1) Calculated From Corrected Flow Rate	(2) Average Up	Average Down	(1)	(2)	
1	FLT22	08/22/96	5.13	2.51	0.033	0.086	0.064	0.00333	0.00865	13.78
2	FLT16	08/16/96	8.55	5.68	0.075	0.124	0.103	0.00755	0.01248	15.56
3	FLT17	08/19/96	8.55	5.68	0.075	0.117	0.096	0.00755	0.01177	15.42
4	FLT14	08/15/96	17.10	13.61	0.180	0.184	0.154	0.01808	0.01851	24.24
5	FLT15	08/16/96	17.10	13.61	0.180	0.184	0.155	0.01808	0.01851	18.00
6	FLT18	08/19/96	25.65	21.54	0.284	0.333	0.289	0.02861	0.03351	42.38
7	FLT19	08/20/96	25.65	21.54	0.284	0.333	0.290	0.02861	0.03351	56.30
8	FLT20	08/20/96	25.65	21.54	0.284	0.328	0.272	0.02861	0.03300	25.83
9	FLT21	08/20/96	25.65	21.54	0.284	0.328	0.275	0.02861	0.03300	55.80
10	FLT02	07/22/96	34.20	29.48	0.389	0.326	0.483	0.03914	0.03280	54.50
11	FLT03	07/26/96	34.20	29.48	0.389	0.393	0.487	0.03914	0.03955	53.46
12	FLT11	08/14/96	51.30	45.34	0.598	0.704	0.589	0.06021	0.07084	69.54
13	FLT12	08/15/96	51.30	45.34	0.598	0.739	0.630	0.06021	0.07436	71.97
14	FLT13	08/15/96	51.30	45.34	0.598	0.739	0.610	0.06021	0.07436	88.60
15	FLT04	07/29/96	68.40	61.20	0.808	0.994	1.223	0.08127	0.10002	78.54
16	FLT05	07/29/96	68.40	61.20	0.808	0.995	1.290	0.08127	0.10012	83.19
17	FLT09	08/13/96	102.60	92.93	1.226	1.372	1.220	0.12340	0.13806	90.24
18	FLT10	08/13/96	102.60	92.93	1.226	1.536	1.289	0.12340	0.15456	87.71

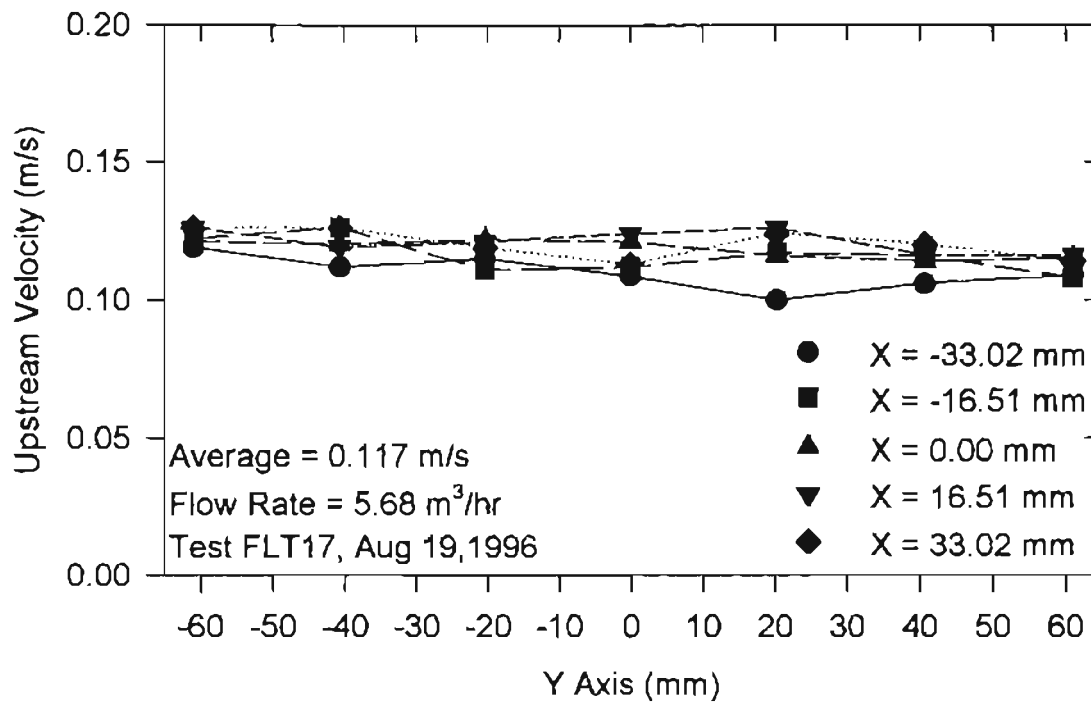


Figure 5.2 Local Upstream Velocity for Flat Filter (5.68 m³/hr).

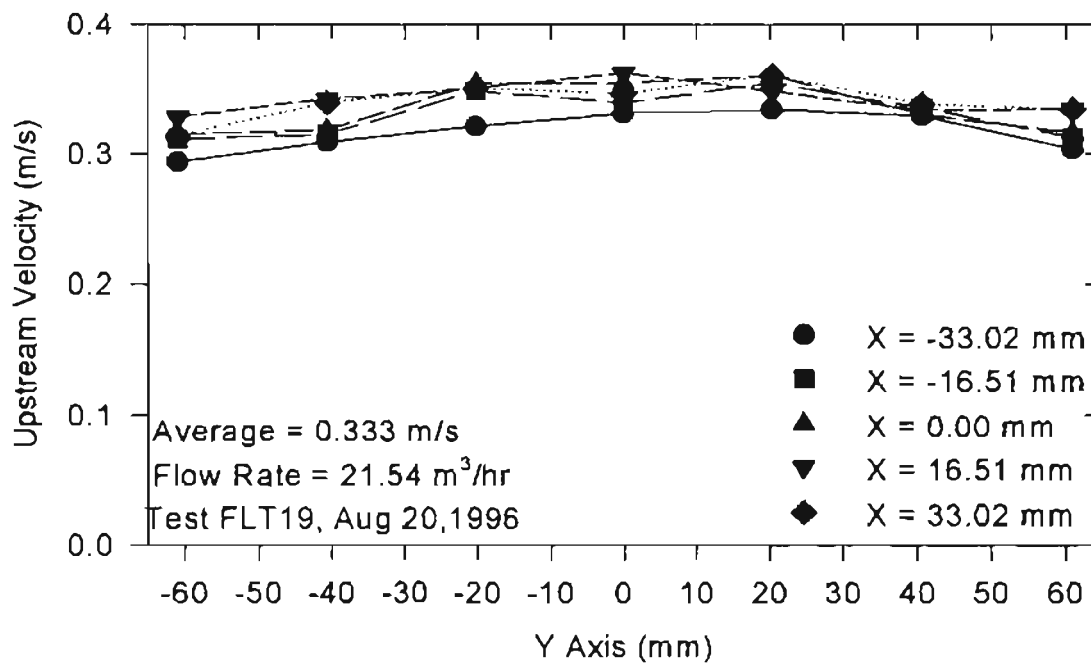


Figure 5.3 Local Upstream Velocity for Flat Filter (21.54 m³/hr).

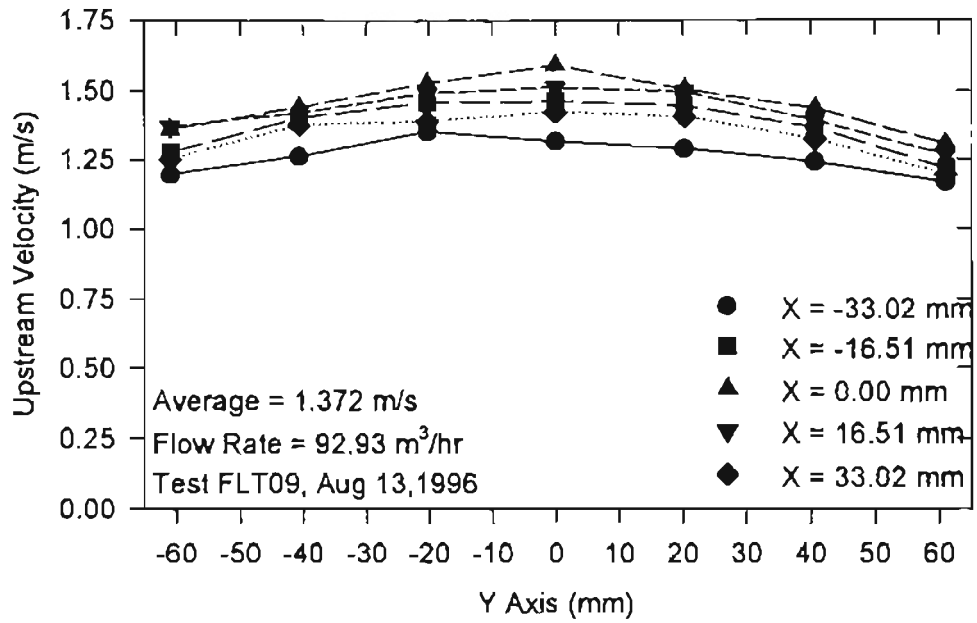


Figure 5.4 Local Upstream Velocity for Flat Filter (92.93 m³/hr).

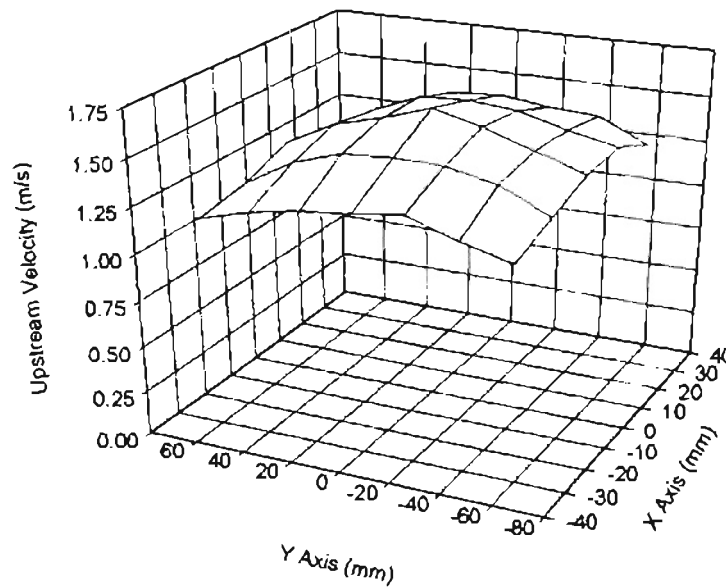


Figure 5.5 Local Upstream Three-Dimensional Velocity for Flat Filter (92.93 m³/hr).

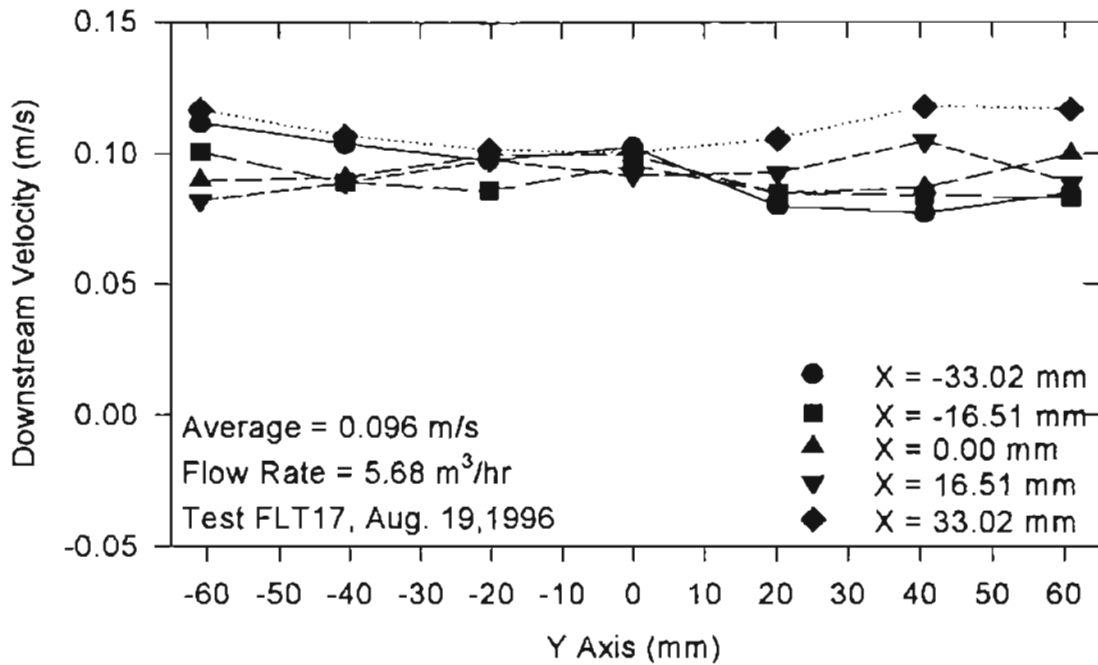


Figure 5.6 Local Downstream Velocity for Flat Filter (5.68 m³/hr).

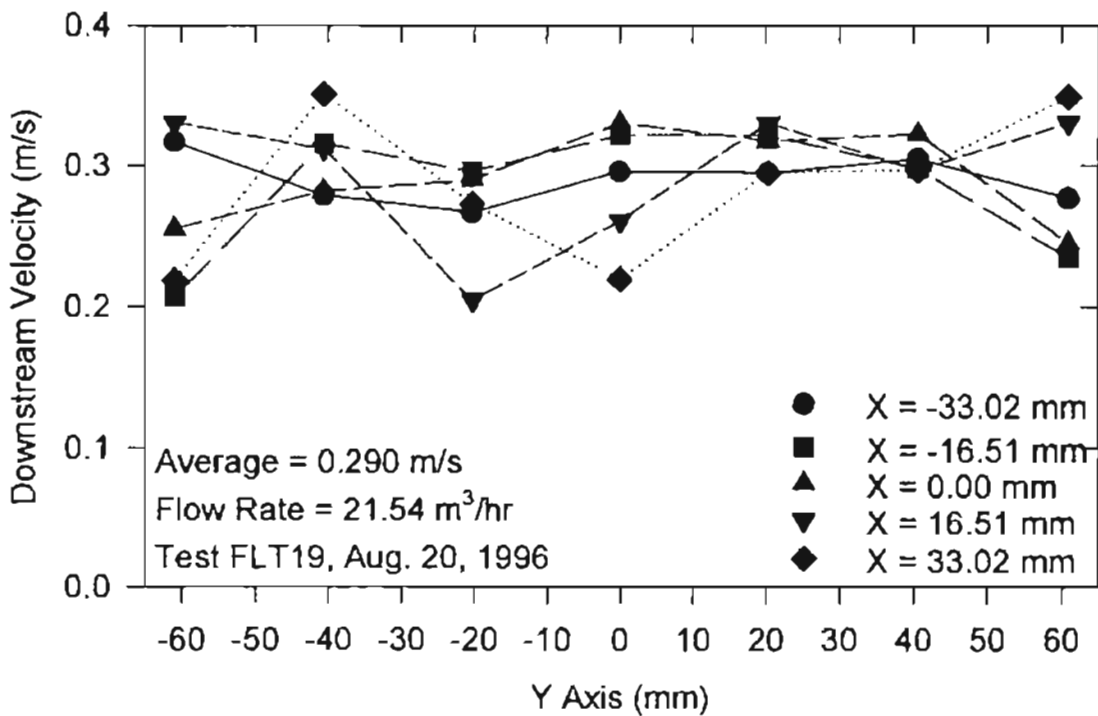


Figure 5.7 Local Downstream Velocity for Flat Filter (21.54 m³/hr).

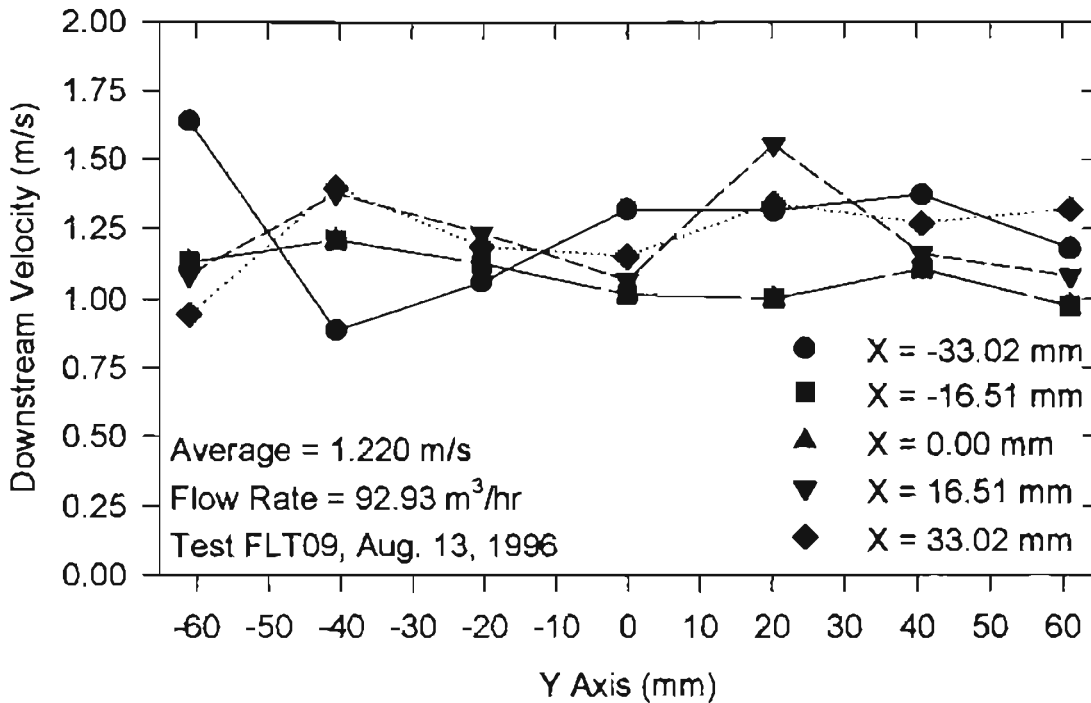


Figure 5.8 Local Downstream Velocity for Flat Filter (92.93 m³/hr).

5.2.2 Measured Number Densities

The number densities are also banded together. Figures 5.9, 5.10 and 5.11 show the upstream number densities while Figs. 5.12, 5.13 and 5.14 show the downstream number densities for the same tests for which velocities were shown earlier. The uniform flow field upstream is primarily responsible for the banded number densities which are within a $\pm 10\%$ bandwidth. The average upstream number densities range from 7×10^8 to $2 \times 10^{10} / \text{m}^3$ while the downstream number densities range from 1×10^8 to $1.7 \times 10^{10} / \text{m}^3$ for the entire range of flow rates examined in this study (Table 5.1).

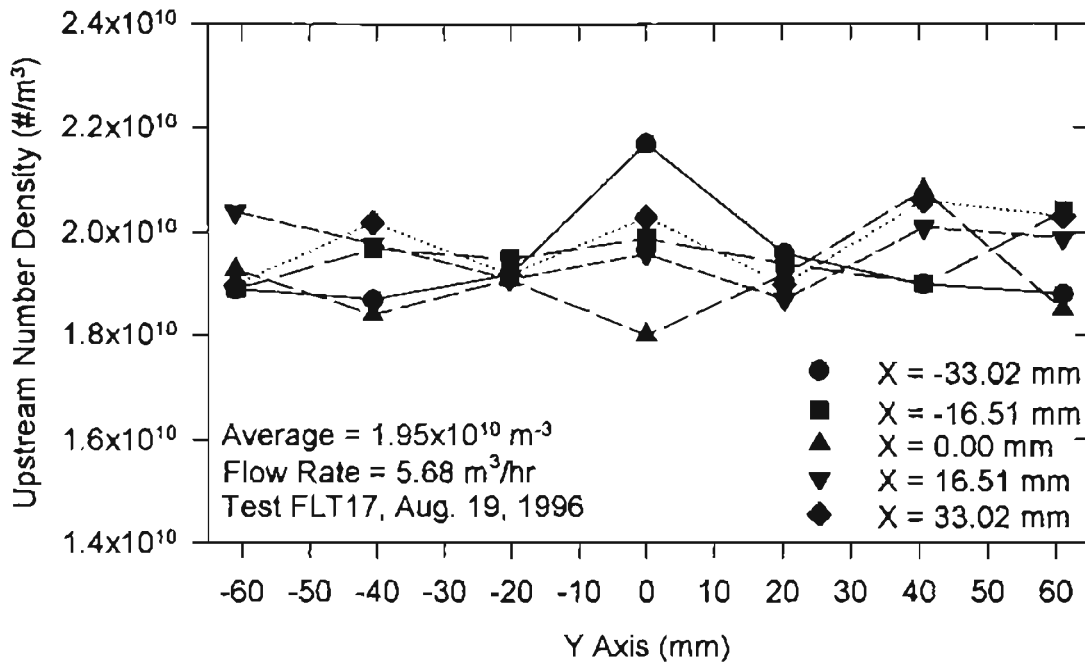


Figure 5.9 Local Upstream Number Densities for Flat Filter ($5.68 m^3/hr$).

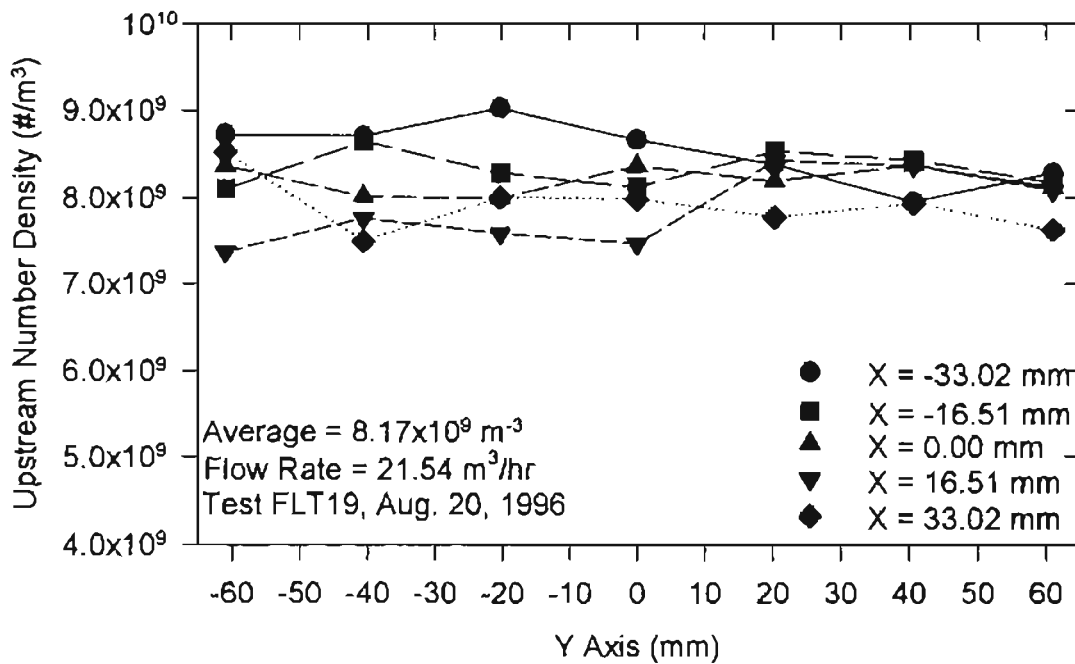


Figure 5.10 Local Upstream Number Densities for Flat Filter ($21.54 m^3/hr$).

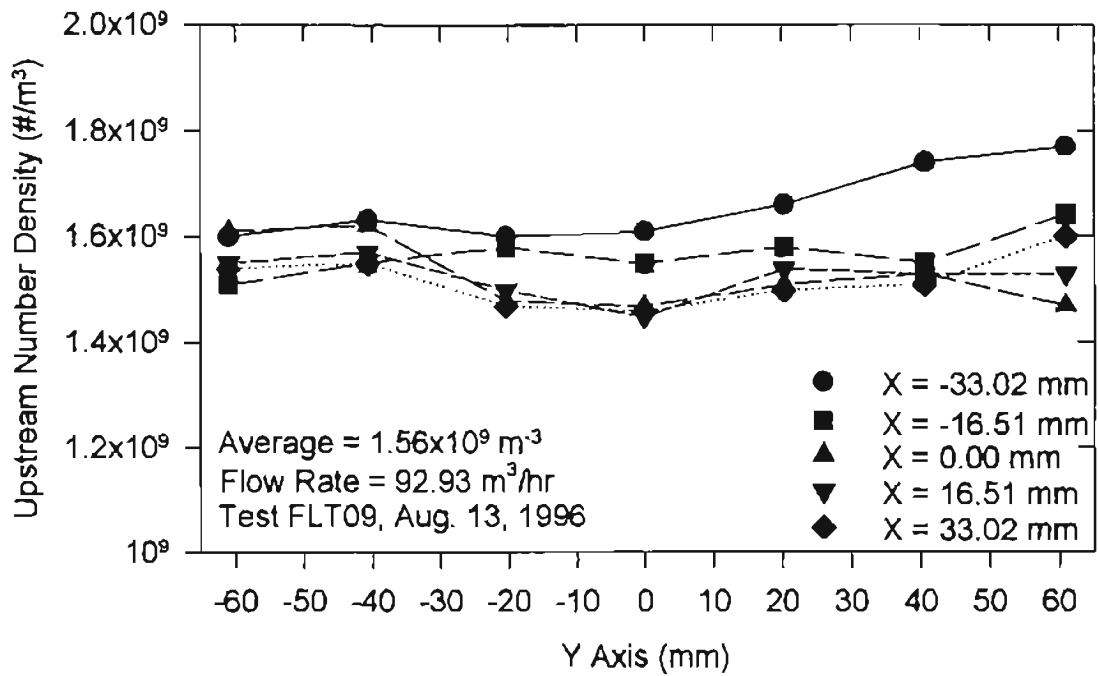


Figure 5.11 Local Upstream Number Densities for Flat Filter ($92.93 \text{ m}^3/\text{hr}$).

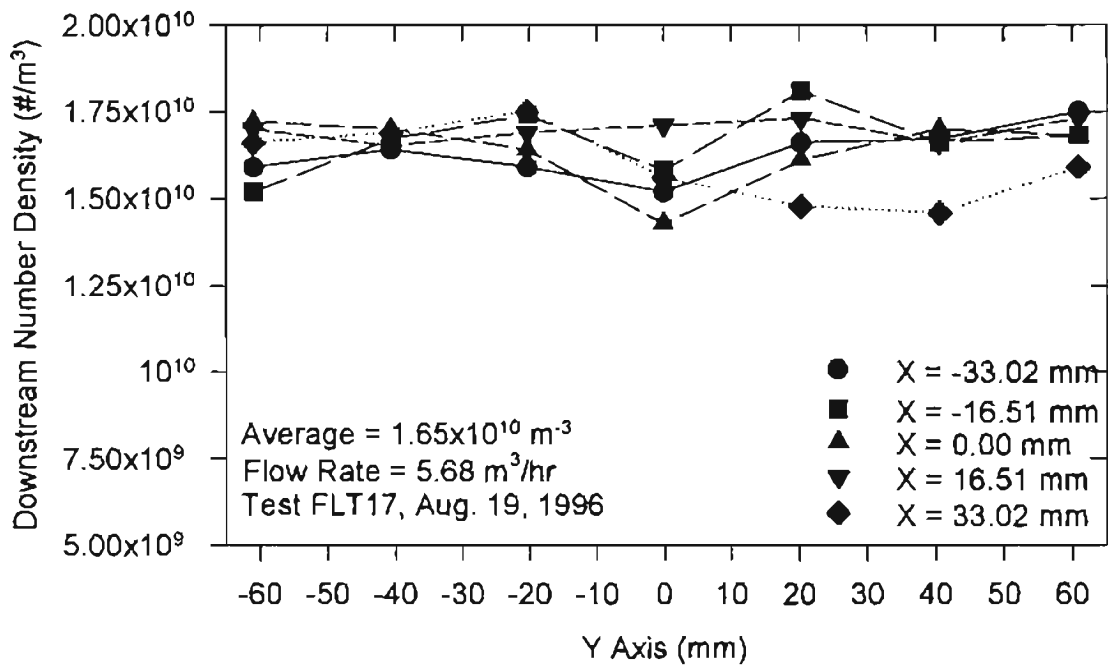


Figure 5.12 Local Downstream Number Densities for Flat Filter ($5.68 \text{ m}^3/\text{hr}$).

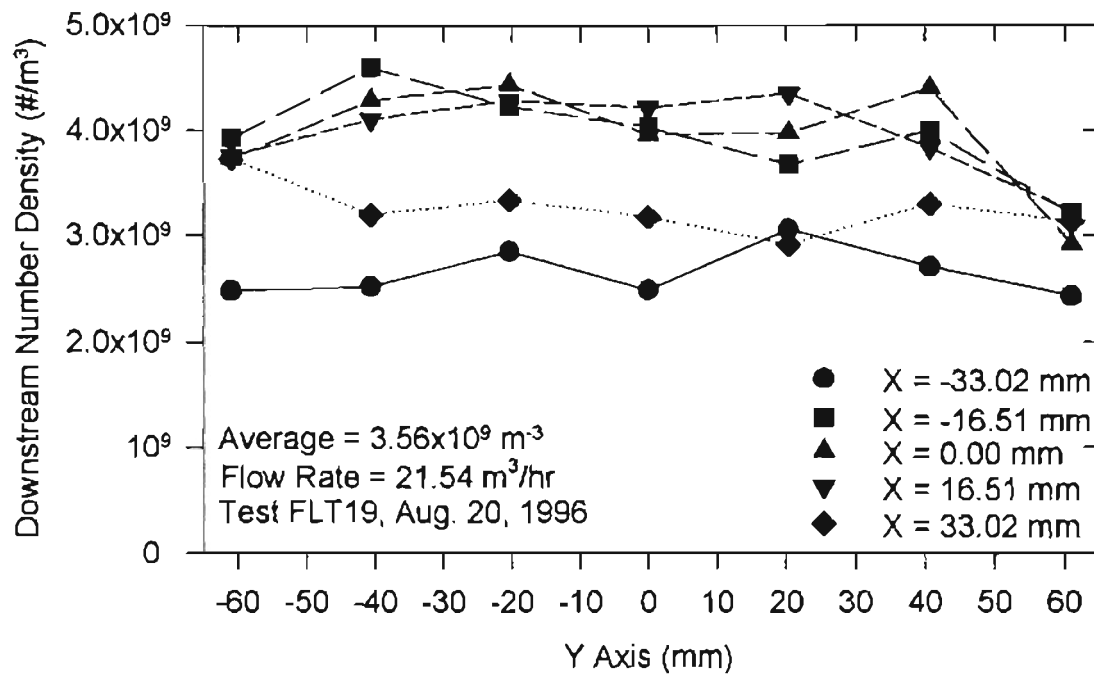


Figure 5.13 Local Downstream Number Densities for Flat Filter ($21.54 m^3/hr$).

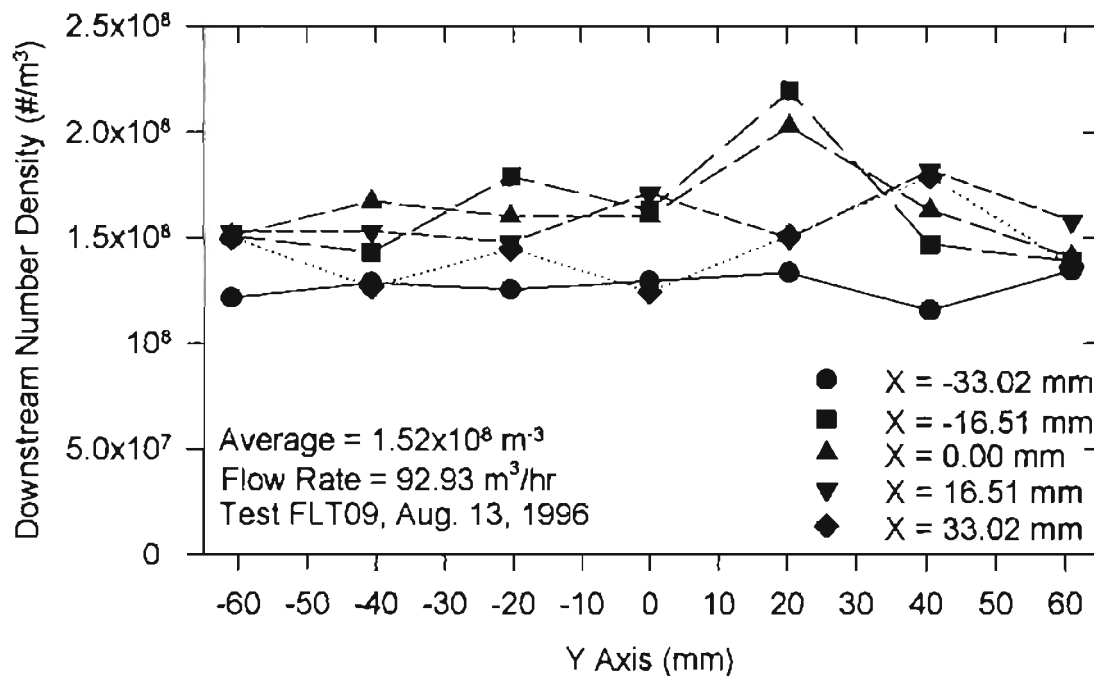


Figure 5.14 Local Downstream Number Densities for Flat Filter ($92.93 m^3/hr$).

Figure 5.13 indicates that the two edge rows on the grid have lower number densities than the rest of the filter. This may be due to the typical measurement procedure described earlier. The central grid locations on the downstream side were measured with a clean filter while the edge rows were measured with the same filter loaded. The extent of the filter clogging can be predicted by a combination of flow velocity (flow rate), number of samples counted, and the solution concentration used. The solution concentration and number of samples counted were varied to ensure that the time taken to count the samples was minimized. The problem of filter clogging is most severe at lower flow rates where the number densities are higher and deposit more particles on the filter.

5.2.3 Pressure Drop Measurements

Pressure drop values for the tests were recorded at four time intervals - start of the test, start of the downstream measurements, end of the downstream measurements, and end of the test. These values are shown in Table 5.1 which also shows the pressure drop change for the entire test and the more important change between the start of the test and the end of measurement on the downstream plane. Initial pressure drop values indicate (Fig. 5.15) that pressure drop rises with flow rate. Figure 5.15 shows a trend similar to the one shown in Figs. 2.19 and 2.20 [Walker and Ptak, 1996]. A comparison with the pressure drop measurements of Tebbutt [1995] is shown in Fig. F-1; and agreement with his data is good for low flow rates (less than $60 \text{ m}^3/\text{hr}$), but deviates for high flow rates (greater than $60 \text{ m}^3/\text{hr}$). The change in pressure drop will be discussed in the next section along with efficiency.

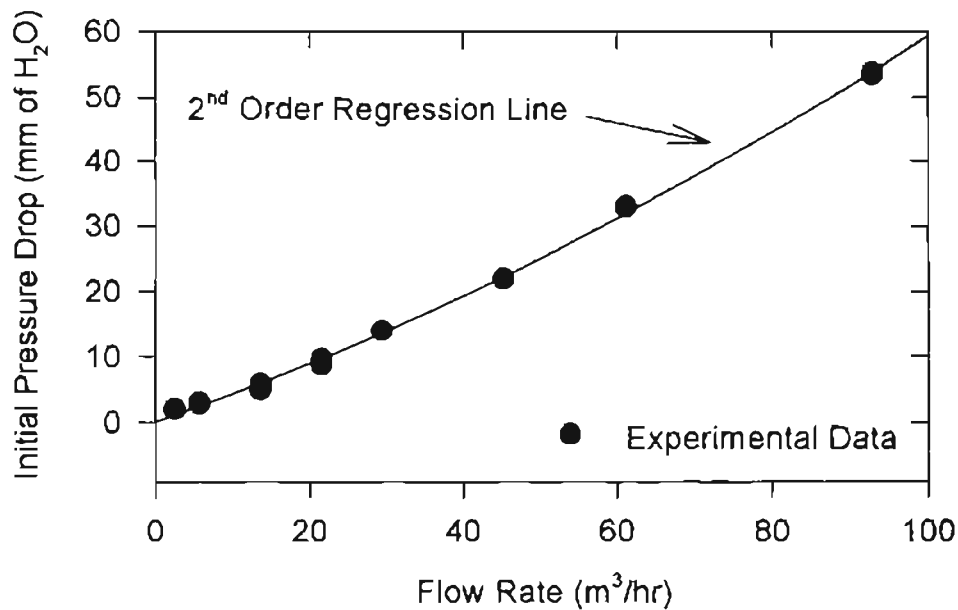


Figure 5.15 Pressure Drop Variation with Flow Rate.

5.2.4 Filter Efficiency and the Influence of Pressure Drop Change

Figures 5.16, 5.17 and 5.18 show the local efficiency plots for the three sample flow rates of 5.68, 21.54 and 92.93 m³/hr. The local efficiency values are very closely banded for the flow rate of 92.93 m³/hr (Fig. 5.18) while at the lower flow rate of 5.68 m³/hr (Fig. 5.16), the band stretches from 10 to 30%. For the intermediate flow rate of 21.54 m³/hr, the band is expected to be between the ones for 5.68 and 92.93 m³/hr and can be confirmed from the local efficiency plots of test FLT20 (Appendix D) which has a lower pressure drop change indicating measurements over a cleaner filter. The bandwidth of the efficiency values depends on the average value as explained in section 4.2. Higher average values should have a tighter bandwidth and vice versa. Figure 5.17 shows a wider band primarily because of the two edge rows which were measured last on the downstream side (see section 5.2.2 and Fig. 5.13).

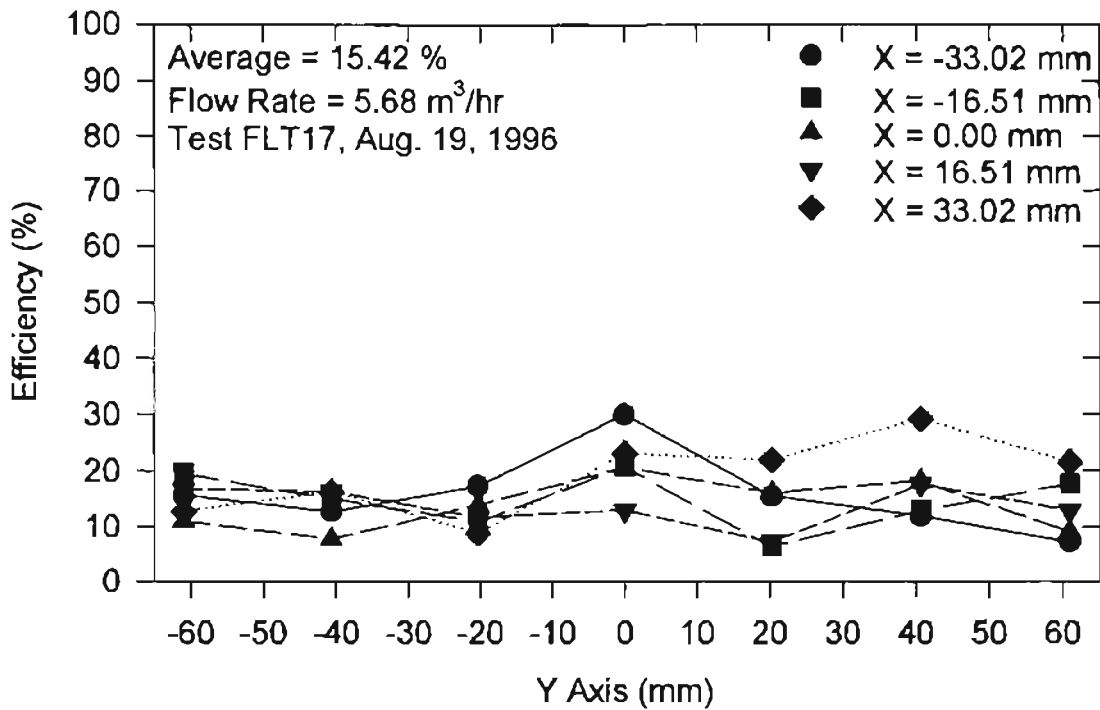


Figure 5.16 Local Efficiency for Flat Filter (5.68 m³/hr).

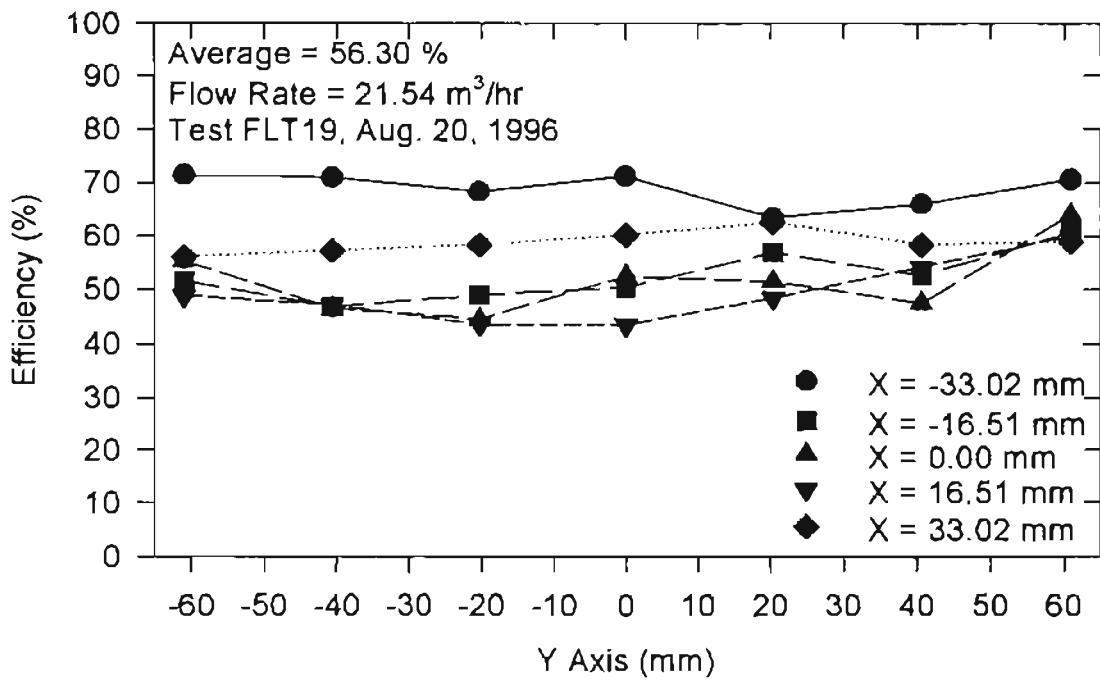


Figure 5.17 Local Efficiency for Flat Filter (21.54 m³/hr).

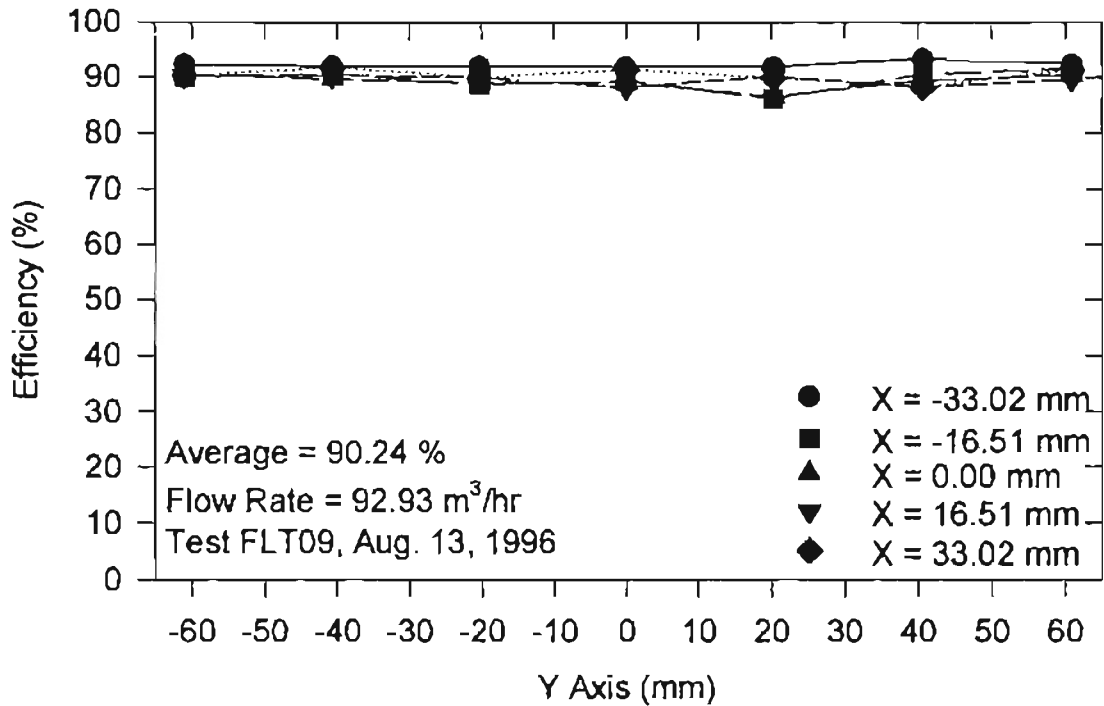


Figure 5.18 Local Efficiency for Flat Filter (92.93 m³/hr).

The overall efficiency plot is shown in Fig. 5.19. It shows the overall average efficiency for each test versus the corrected flow rate of the test. The lines on the plot are fourth order regression curve fits and are drawn to indicate a trend in the efficiency values. The numbers around the experimental points are the pressure drop changes during the measurement of the downstream plane. The data shows a trend similar to that observed in the literature [Davies, 1973 and Sabnis, 1994]. A plot of local efficiency versus local upstream velocity shown in Fig. F-2 displays the same trend.

For the flow rates of 21.54 and 45.34 m³/hr, the efficiency points look scattered over a wide band. This is not experimental or other error but can be explained by taking a closer look at the pressure drop change values. The higher the pressure drop change, the

higher is the efficiency as the filter gets clogged due to particle deposition. A look at the downstream number densities (Table 5.1) for these flow rates clearly demonstrates a drop in values with increasing pressure drop changes. Two efficiency points on Fig. 5.19 for these flow rates were obtained by repeating the downstream measurement at the end of the first test. These points are marked on Fig. 5.19, and the higher efficiency points are those for the repeat measurements. A fourth order regression line for the lowest efficiency values at each flow rate is also drawn on Fig. 5.19. It shows the trend for relatively clean filter measurements.

There is no definition of a clean filter available in literature either in terms of loading or pressure drop change. Yeh [1972] made filter efficiency measurements with aerosols and discarded filters if the pressure drop change exceeded 10% of the initial pressure drop change. Most experimental measurements assume 254 mm of water (or 10" of water) as the terminal pressure drop for filter efficiency measurements, or in other words, this is the pressure drop for a dirty filter. The results in this study for the repeated downstream side indicate that even for small pressure drop changes of about 5 mm of water, the efficiency can change by almost 30 percentage points (21.54 m³/hr case).

Initial pressure drop is proportional to the flow rate as shown in Fig. 5.15. Thus, the lower flow rates have a lower initial pressure drop, while the higher flow rates have a higher initial pressure drop. Therefore, to attain a given value of pressure drop (not pressure drop change), the filter loading required at the lower flow rates will be more than that required for the higher flow rates. The author would like to suggest that defining a dirty filter in terms of an absolute terminal pressure drop is arbitrary. This terminal value

needs to be defined as a percentage of the initial pressure drop. The author would suggest that a pressure drop change of 10% of the initial value seems reasonable. Table 5.3 shows the percentage changes for the data obtained in this study. For the flow rate of 5.68 m³/hr, this 10% criteria is satisfied, while the remaining data shown shaded in Table 5.3 would meet a slightly higher criteria of a 20% change in pressure drop. The high 54.05% and 113.79% changes for tests FLT21 and FLT13 can be explained by the fact that these tests had the same upstream measurements as tests FLT20 and FLT12, respectively, but the downstream measurements were repeated at the end of the upstream measurements.

The percentage changes in pressure drop and the efficiencies for tests FLT11 and FLT12 compare well but these are over the 20% criteria indicating that the two tests took too long for the efficiencies to be seen as clean filter measurements. The same is true for tests FLT18 and FLT19; however, test FLT20, at the same flow rate of 21.54 m³/hr, has a 10.81% change and represents a clean filter measurement under the criteria specified above. This can also be seen from the fact that test FLT20 has the lowest overall efficiency among the four tests for this flow rate of 21.54 m³/hr.

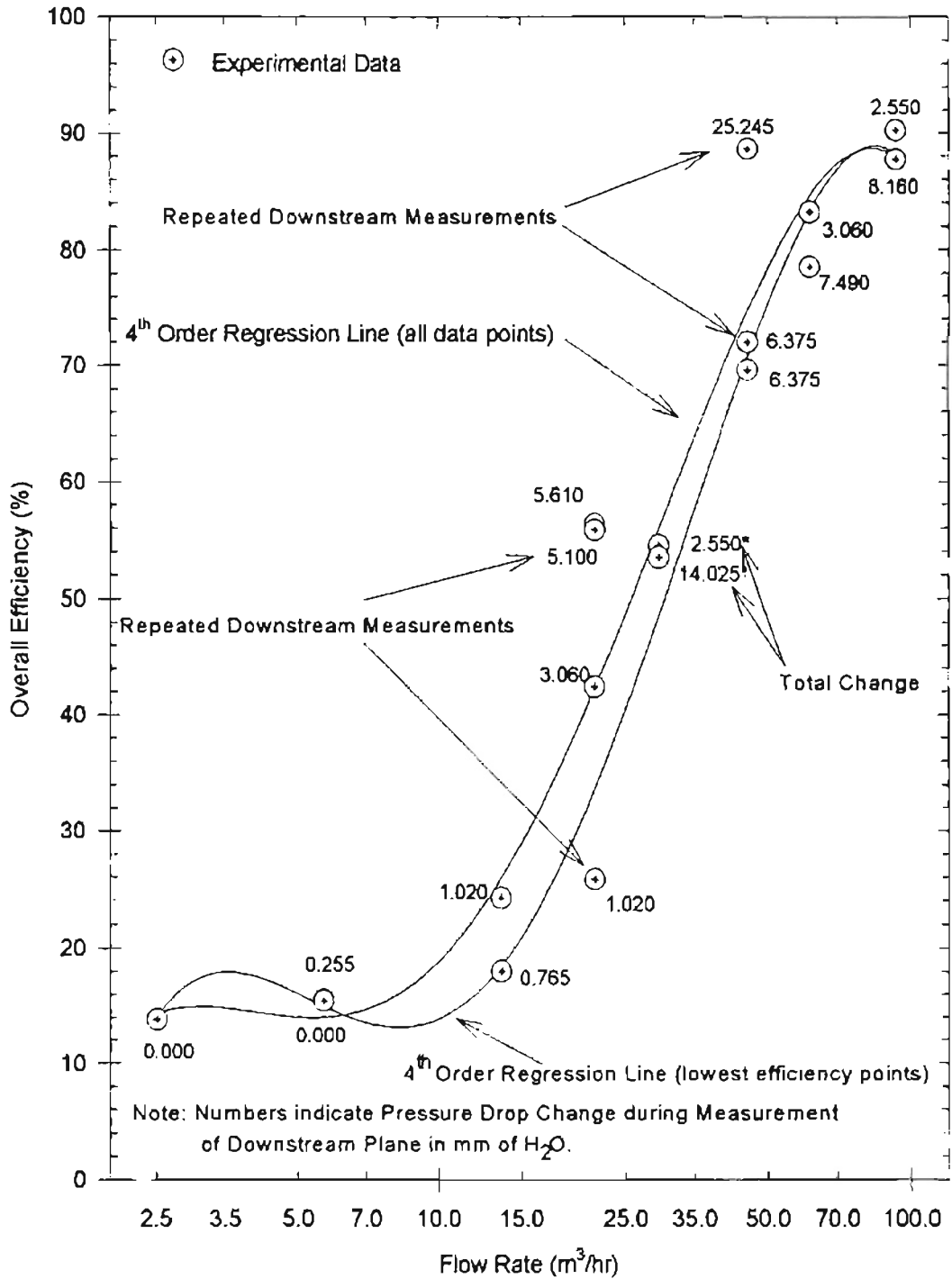


Figure 5.19 Overall Efficiency versus Flow Rate.

Table 5.3 Percentage of Pressure Drop Change for Present Study

No.	Test Name	Flow Rate (m ³ /hr)	Initial Pressure Drop (mm of H ₂ O)	Change in Pressure Drop for Downstream (mm of H ₂ O)	Percentage Pressure Drop Change (%)	Efficiency (%)
1	FLT22	2.51	2.040	0.000	0.00	13.78
2	FLT16	5.68	3.060	0.255	8.33	15.56
3	FLT17	5.68	2.805	0.000	0.00	15.42
4	FLT14	13.61	5.865	1.020	17.39	24.24
5	FLT15	13.61	4.845	0.765	15.79	18.00
6	FLT18	21.54	8.670	3.060	35.29	42.38
7	FLT19	21.54	9.690	5.610	57.89	56.30
8	FLT20	21.54	9.435	1.020	10.81	25.83
9	FLT21	21.54	9.435	5.100	54.05	55.80
10	FLT02	29.48	14.025	N/A	N/A	54.50
11	FLT03	29.48	14.025	N/A	N/A	53.46
12	FLT11	45.34	21.930	6.375	29.07	69.54
13	FLT12	45.34	22.185	6.375	28.74	71.97
14	FLT13	45.34	22.185	25.245	113.79	88.60
15	FLT04	61.20	33.150	7.490	22.59	78.54
16	FLT05	61.20	32.895	3.060	9.30	83.19
17	FLT09	92.93	53.550	2.550	4.76	90.24
18	FLT10	92.93	53.805	8.160	15.17	87.71

Note: Shaded values meet 20% pressure drop criteria.

N/A: Not Available (pressure drop at beginning and end of downstream measurement not recorded).

5.3 Stokes Number Analysis

Comparison of filtration efficiencies has also been done on the basis of Stokes number defined in Eq. (2-4). The overall efficiencies are plotted versus the Stokes number in Fig. 5.20 (also see Table 5.2). Since the flow velocity calculated from the corrected flow rate differs from the measured value (Table 5.2), there will be two Stokes number values. Stokes number values for the present study range from 0.00865 to 0.15456 (based on measured average velocities). Efficiencies with both of these values of Stokes number have been plotted in Fig. 5.20 and are very close to each other, indicating that the velocity

difference translates into a very small Stokes number difference. In the present study, the only parameter varied in Eq. (2-4) is the flow velocity; thus the Stokes number plot with calculated velocity looks similar to the flow rate plot. Fourth order regression curve fits have also been drawn to indicate the trend. The efficiency remains nearly constant at the lower Stokes numbers (or flow rates) and then rises sharply for Stokes numbers ranging from 0.015 to 0.1 before flattening out again. Classical theory suggests that efficiency shows a dip at the lower Stokes number range and a peak at the higher Stokes number range. The flow and instrumentation setup restricted the study of efficiency values for flow rates (or Stokes number) outside of the range reported in this study.

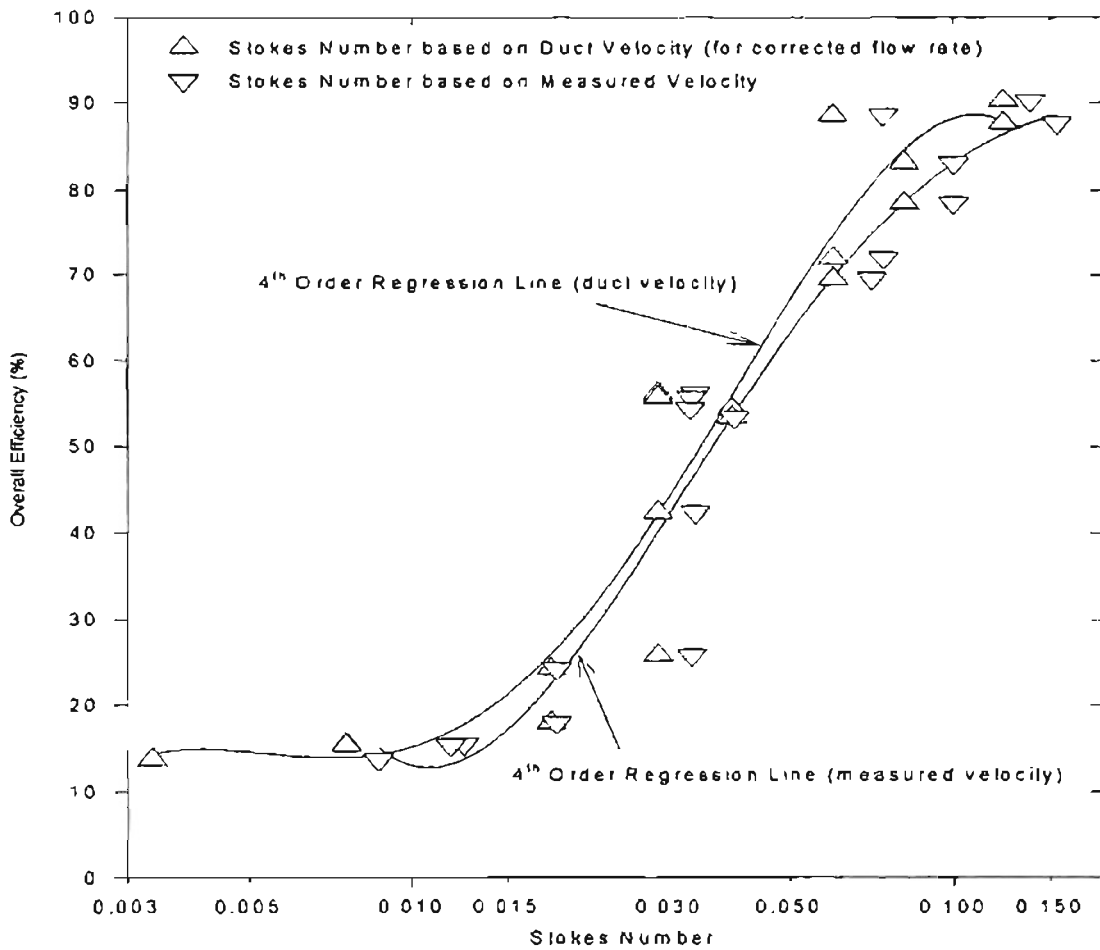


Figure 5.20 Overall Efficiency versus Stokes Number.

5.4 Comparison of Results

In this section, the results obtained in this study will be compared to those of Williams [1996], Jadbabaei [1997], Lee [1977] and some other researchers. A comparison with the data of Williams [1996] is shown in Fig. 5.21. It shows that the trend observed by Williams was similar to the present study. However, for lower Stokes number values, his efficiency values were higher than those of the present study. Efficiency values for higher Stokes numbers indicate a better match. The pressure drop values reported by Williams show higher percentage rises in pressure drop change for the lower Stokes number than the present study. This could explain the higher efficiencies that he observed at the lower Stokes number. Williams [1996] conducted only one test for each of the six flow rate values (8.8, 17.5, 26.2, 42.5, 68, 102.0 m³/hr) and showed no correlation of pressure drop change to efficiency. Also, he had problems in reliability and repeatability of his results. Therefore, the comparison with his results may be suspect.

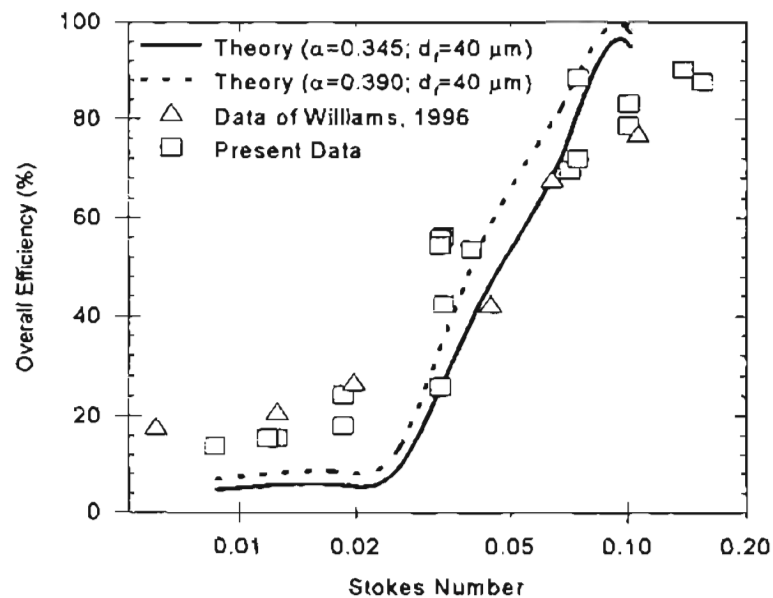


Figure 5.21 Comparison of Present Data with the Data of Williams [1996] and the Theory of Duran [1995].

Figure 5.21 also shows a comparison of the present data with the theoretical model of Duran [1995]. The flat lines at the lower Stokes number region are because of interception which is the primary filtration mechanism at these low flow rates and is independent of flow velocity. In the lower Stokes number region the theoretical efficiency values are lower than the experimental ones.

Figure 5.22 shows a comparison of the present data with the results of Lee [1977]. Typical values of Lee's data have been extracted for comparison (explained in section 2.5 and Fig. 2.7). The results show good agreement with the efficiency values for Dacron B filter media ($\alpha = 0.271$). The filter media used in the present study had an α of approximately 0.345 (as calculated by Williams [1996] and Natarajan [1995]).

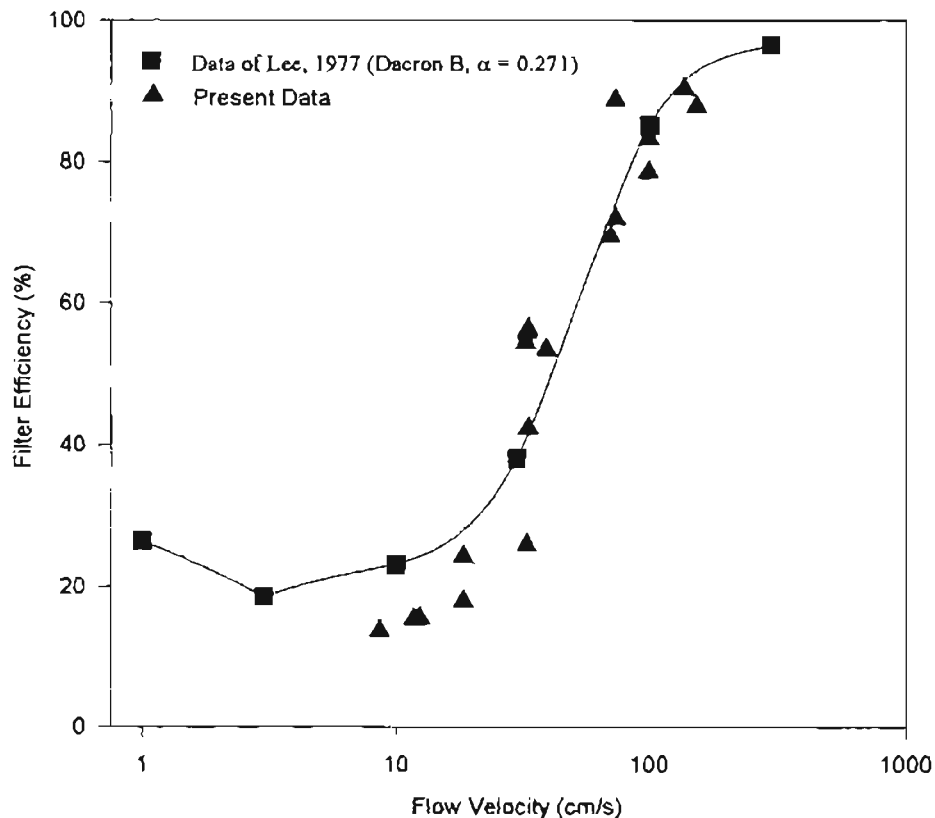


Figure 5.22 Comparison of Present Data with Lee [1977].

A comparison of the present data with the pleated filter results of Jadbabaei [1997] is shown in Fig. 5.23. The Stokes number for the pleated filters has been calculated on the basis of duct velocity, i.e., the velocity inside the housing. The trends of the efficiency measurements are similar but the data appears shifted. For the flat media used in the present study, the duct velocity and the face velocity are the same but, for the pleated filters used by Jadbabaei [1997], the face velocity is the velocity obtained by uniformly distributing the flow rate over the entire unfolded filter. Keeping in mind that the pleats were 3 cm high and there were 320 pleats/meter, the ratio of duct velocity to face velocity would be 19.25.

Since all of the parameters required for calculating the Stokes number, except velocity, were the same, one would expect the efficiency data points to be shifted to the higher Stokes number side by a Stokes number which is 19.25 times the Stokes number for the pleated filter. This was not observed as shown in Fig. 5.23. However, if the pleated filter data points were shifted to the higher Stokes number side by a factor of four, there is some agreement with the flat filter results of the present study. Thus, the author would want to conclude that the ratio of duct velocity to effective face velocity is about 4 and not 19.25 as calculated by uniformly distributing the flow over the unfolded filter.

A probable explanation for this can be based on the fact that, for small pleat angles (or high pleat count), there is a sharp velocity gradient over the pleat, with higher velocities near the base of the pleat [Tebbutt, 1995]. The higher the pleat count, the sharper is the velocity gradient. This velocity gradient also results in an increased viscous drag causing an increase in the pressure drop across the filter as shown in Fig. 2.25.

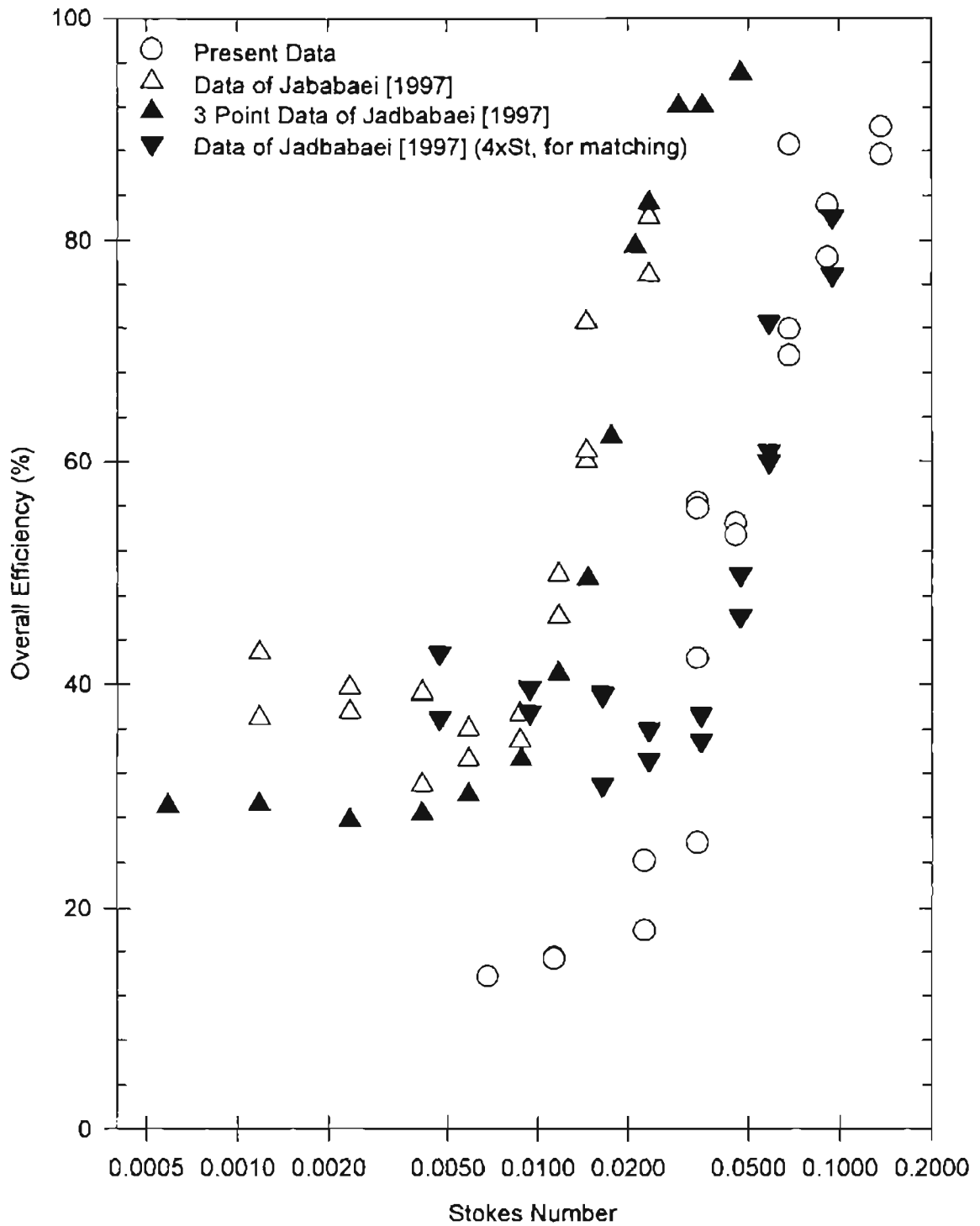


Figure 5.23 Comparison of Present Data with Pleated Filter Results of Jadbabaei [1997].

The velocity gradient yields an integrated average velocity value equal to 4 times the face velocity (and not 19.25 times as) obtained by unfolding the filter and distributing the flow evenly. Moreover, efficiency of any filter media is a function of the flow velocity. Therefore, a velocity gradient would result in an efficiency gradient over the pleat. The efficiency gradient for the pleated filter used by Jadbabaei [1997] would result in an overall efficiency value which would be equal to an efficiency value obtained if the face velocity were multiplied by 4.

Another observation which can be made from Fig. 5.23 is that the filter efficiencies at lower flow rates (or Stokes number) are lower for flat media than pleated filters. This can be explained by the fact that, at these lower flow rates, the particle kinetic energy is low, and the flat media provides a relatively straighter path for the particle to pass through, than in the case of pleated filters. Thus, pleated filters would show higher filter efficiencies at the lower flow rates.

CHAPTER VI

SUMMARY, CONCLUSIONS AND RECOMMENDATIONS

6.1 Summary of Results

The present study was done on the filter media used in the manufacture of the Purolator A13192 pleated automotive filter. The following is a summary of the results found in the present study:

1. Temperature was the most important factor influencing the instrumentation. A rise in the temperature caused a fall in the laser power due to misalignment of the optics which resulted in inaccurate number density measurements. The present study was able to overcome this difficulty by controlling the temperature around the optical setup to within $\pm 0.5^{\circ}\text{C}$.
2. The high voltage and threshold settings on the DSA software were determined to be the most critical parameters for number density measurements. Their values should be set in accordance with the flow rate for each test. The data rate should be monitored and the high voltage and threshold set such that the highest data rate with a data validation of around 80-95% is achieved.
3. The consistency of the atomizer as a seeding mechanism was verified by making accurate and repeated open flow measurements. The sampling rate varied between $\pm 5\%$.

4. Tests with no filter inside the housing gave efficiency values close to zero (-0.39% and -0.22% for two such tests), displaying the capability of the system to make accurate measurements. A repeated number (three) of such tests gave confidence in the repeatability of the system ($\pm 5\%$).
5. The upstream velocities and number densities for the small angle diffuser housing showed a flat profile which was expected for a uniform flow field. The downstream velocities and number densities did not show a flat profile but were banded together.
6. The local efficiency values were also banded together and did not show any large variations for a particular flow rate (as observed by Williams [1996]). The band was about 5% at higher flow rates ($92.93 \text{ m}^3/\text{hr}$) and about 20% for lower flow rates ($5.68 \text{ m}^3/\text{hr}$). At some flow rates the band was wider due to the edge rows (as explained in section 5.2.4).
7. The initial pressure drop measurement was proportional to the flow rate (see Fig. 5.15), and the change in pressure drop during the measurement at the downstream plane affected the downstream number density values which consequently affected the efficiency. A higher pressure drop change indicated a clogged filter with higher efficiency. A pressure drop change of more than 10% from the initial value indicated a plugged filter with higher efficiency.
8. The efficiency values increased from about 13% to 90% with increasing Stokes numbers between 0.003 to 0.150 (or flow rates from 2.51 to $92.93 \text{ m}^3/\text{hr}$) (see Fig. 5.20). The data from the present study matched that of Lee [1977]. There was a reasonable agreement with the results of Williams [1996].

9. Comparison with the pleated filter results of Jadbabaei [1997] indicated that the face velocities should be ratioed by about 4 and not 19.25, as calculated from theory which unfolds the pleats and uniformly distributes the flow.

6.2 Conclusions

The present study examined the filtration efficiency of flat sheet filter media and compared the experimental results to the pleated filter efficiency results of Jadbabaei [1997]. The following major conclusions are drawn:

1. Local filtration efficiency of flat sheet filters is uniform if the filter is exposed to a uniform flow field. A single point measurement of efficiency can replace local measurements over the entire filter for such a uniform flow field. Flow fields in actual automotive housings are more complex and would need local measurements.
2. The trends in efficiency values (for 1 μm particles) indicate that, for low flow rates, the efficiencies are low and relatively constant with flow rate. For intermediate flow rates (from 10 to 60 m^3/hr) the efficiency values rise sharply before flattening out at the higher flow rates.
3. Change in pressure drop of a filter is critical as it affects the efficiency of the filter. In any study examining the characteristics of filter media, the pressure drop change during particle concentration measurement should not increase by more than 10% of the initial value to ensure clean filter measurements.
4. The ratio of the face velocities of flat and pleated filters is not the ratio of their areas but is a more complex relationship determined by the flow field immediately over the

pleat surfaces.

6.3 Recommendations for Future Work

The author would like to make the following suggestions for future work in this area:

1. Although the author feels that the consistency of the measurements has been tested extensively during the present study, the methods used to maintain temperature around the optical system need to be reviewed. The bypass used to adjust flow rate on the Purolator test stand blower should be connected to the external environment and prevented from exhausting the conditioned room air. Also, to prevent the optical system from misalignment, it should be mounted on a breadboard made from a low thermal expansion material.
2. More extensive testing needs to be done to confirm the influence of pressure drop change on efficiency. A rigorous effort to quantify this effect is required. Number density measurements at the downstream plane need to be repeated during the same test while recording the pressure drop changes. A number of such tests over a range of flow rates (or Stokes number) would yield a variation of efficiency with pressure drop (or loading). The author would expect the efficiency to rise to about 90-95% for all flow rates for some pressure drop before mechanisms like reentrainment cause reduction in efficiency. However, with the current system, the number density measurements at extremely low concentrations (downstream plane at high efficiencies) would be difficult.

3. Particles of sizes other than $0.966\ \mu\text{m}$ should be used in order to obtain a larger variation in Stokes number and to allow comparison with existing theories and experiments. For larger particle sizes, higher solution concentrations need to be fed from the atomizer to maintain a particle concentration which can be readily detected by the LDV system. For smaller particle sizes, the back scattered signal from the particles has a very low amplitude and may be difficult to distinguish from the background noise. Also, different particle sizes may pose new problems with regard to clogging. The author is unsure about the nature of these problems.
4. Flow rates beyond the range examined in this study need to be investigated to obtain a complete efficiency variation with Stokes number. Lower flow rates may be generated using a different blower and seeding arrangement (feed dry glass beads as seeding from a dust feeder). The upper limit of flow rates in the present study was assumed to be a safe flow rate for the filter media to handle without rupturing. The strength of the filter media needs to be verified to run higher flow rates on it.
5. Electrostatic charges on fibers and particles can affect the filtration efficiency. These charges need to be measured and recorded. Also, their affect on efficiency values needs to be studied. Since the electrostatic effects are more predominant at lower flow velocities, the impact of these on the current results may be more significant at the lower flow rate values.
6. Measurement of local filtration efficiencies in housings resembling actual automotive housing can show the influence of flow fields on efficiency values. Actual housings have complex shapes, and the scope of these measurements may be limited by the

access of the LDV probe volume and the distortion of the probe volume caused by the different path lengths traveled by the laser beams through the inclined housing walls. Modified housings with straighter walls could be constructed for this type of testing. One such design conceived by the author is shown in Fig. 6.1. The design has an inlet and an outlet similar to housings used in some automobiles but has flat front and rear faces for easy access by the probe volume.

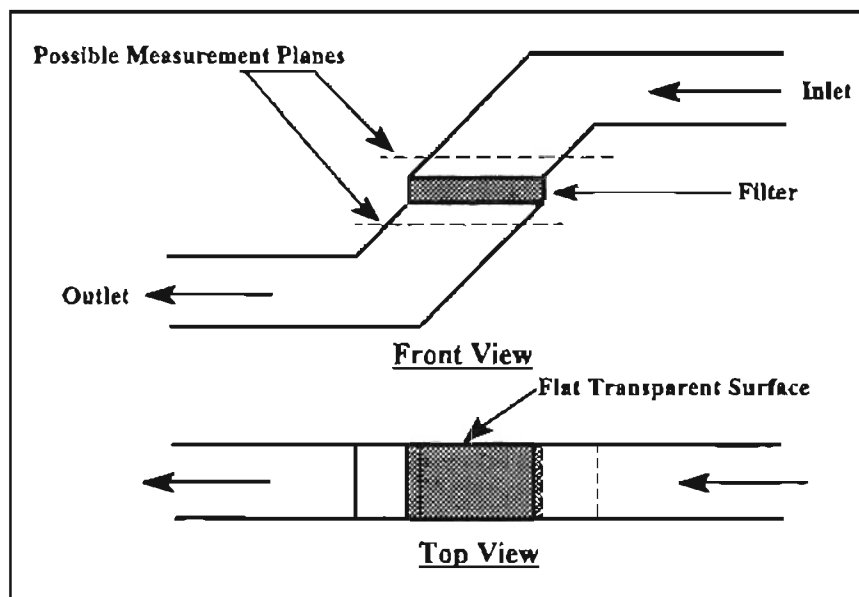


Figure 6.1 Possible Housing Design for Efficiency Measurements.

7. The correlation between pleated and flat filter efficiencies obtained in the present study was specific to one particular filter media. Testing on other types of filter media would help to obtain a more universal correlation. Also, testing with different pleat spacings and pleat heights would add to the universal nature of this correlation. Pleated filters for a variety of media and different pleat spacing and pleat height may not be commercially available and would have to be constructed in-house.

REFERENCES

- Aerometrics (1992), Doppler Signal Analyzer for Phase Doppler Particle Applications User's Manual, Sunnyvale, CA, draft 2.
- American Society for Testing and Materials (1989), "ASTM F 1215-89, Standard Test Method for Determining the Initial Efficiency of a Flatsheet Filter Medium in an Airflow Using Latex Spheres," Annual Book of ASTM Standards, Vol. 14.02, Philadelphia, PA.
- Anand, S., Jadbabaei, F. M., and Dougherty, R. L. (1997), "Comparison of Filtration Efficiency Measurements for Pleated and Flat Sheet Filters," to be presented at the 1997 SAE International Congress and Exposition, Feb. 24-27, Detroit, MI
- Benedict, R. P. (1984), Fundamentals of Temperature, Pressure, and Flow Measurements, Third Edition, Wiley-Interscience, New York.
- Brown, R. C. (1993), Air Filtration: An Integrated Approach to the Theory and Applications of Fibrous Filters, Pergamon Press, Oxford.
- Chen, Da-Ren, Pui, D. Y. H., and Tang Y. M. (1996), "Filter Pleating Design for Cabin Air Filtration," SAE Technical Paper #960941, Aspects of Automotive Filtration (SP-1165), SAE, Inc., Warrendale, PA.
- Davies, C. N. (1973), Air Filtration, Academic Press, New York.
- Drain, L. E. (1980), The Laser Doppler Technique, John Wiley and Sons, London, U. K..
- Duran, R. (1995), "Improvement of Flow Uniformity and Modeling of Filtration Efficiencies for Automotive Air Filter Test Housings," M. S. Thesis, School of Mechanical and Aerospace Engineering, Oklahoma State University, Stillwater, Oklahoma.
- Ensor, D. S., Krafthefer, B. C., and Ottney, T. C. (1994), "Changing Requirements for Air Filtration Test Standards," *ASHRAE Journal*, June, pp. 52-60.
- Gustavsson, J. (1996), "Cabin Air Filters: Performances and Requirements," SAE Technical Paper #960941, Aspects of Automotive Filtration (SP-1165), SAE, Inc., Warrendale, PA.

- Hsieh, Ker-Ching, Wu, T., Connors, P., and Tang, Y. M. (1996), "Performance Enhanced Electret Media," SAE Technical Paper #960534, Aspects of Automotive Filtration (SP-1165), SAE, Inc., Warrendale, PA.
- Jadbabaei, F. M. (1997), "Filtration Efficiency Measurements on Pleated Filters," M. S. Thesis (to be published), School of Mechanical and Aerospace Engineering, Oklahoma State University, Stillwater, Oklahoma.
- Jaroszczuk, T. (1987), "Experimental Study of Nonwoven Filter Performance Using Second Order Orthogonal Design," *Particulate Science and Technology*, Vol. 5, Hemisphere Publishing Corporation, pp. 271-287.
- Jaroszczuk, T., and Wake, J. (1991), "Critical Aerosol Velocity in Nonwoven Filtration," TAPPI Proceedings, Nonwoven Conference, pp. 125-135.
- Jaroszczuk, T., Ptak, T. J., Fallon, S. L., and Wake, J. (1993a), "Particulate and Odor Control Systems in Car Ventilation Systems," SAE Technical Paper #940321, SAE, Inc., Warrendale, PA.
- Jaroszczuk, T., Wake, J., and Connor, M. J. (1993b), "Factors Affecting the Performance of Engine Air Filters," American Society of Mechanical Engineers, Energy Sources Technology Conference and Exhibition, Houston, Texas.
- Kline, S. J., and McClintock, F. A. (1953), "Describing Uncertainties in Single-Sample Experiments," *Mechanical Engineering*, January, pp. 3-8.
- Landahl, H. D., and Hermann, R. G. (1949), "Sampling of Liquid Aerosols by Wires, Cylinders, and Slides, and the Efficiency of Impaction of the Droplets," *Journal of Colloidal Science*, Vol. 4, pp. 103-136.
- Lee, K. W. (1977), "Filtration of Submicron Aerosols by Fibrous Filters," Ph.D. Thesis, University of Minnesota, Minnesota, August, 1977.
- Lee, K. W., and Liu, B. Y. H. (1982a), "Experimental Study of Aerosol Filtration by Fibrous Filters," *Aerosol Science and Technology*, Vol. 1, Elsevier Science Publishing Co., Amsterdam, pp. 25-76.
- Lee, K. W., and Liu, B. Y. H. (1982b), "Theoretical Study of Aerosol Filtration by Fibrous Filters," *Aerosol Science and Technology*, Vol. 1, Elsevier Science Publishing Co., Amsterdam, pp. 147-161.
- Lee, S. E. (1996), "In-Vehicle Performance of New and Used Automotive Cabin Air Filters," SAE Technical Paper #960541, Aspects of Automotive Filtration (SP-1165), SAE, Inc., Warrendale, PA.

Liang, F. (1994), "Particle Counting and Sizing with LDV for Automotive Air Filters," Ph.D. Qualifying Exam Report, School of Mechanical and Aerospace Engineering, Oklahoma State University, Stillwater, Oklahoma.

Liang, F. (1997), "Particle Counting and Sizing with LDV for Automotive Air Filters," Ph.D. Thesis, School of Mechanical and Aerospace Engineering, Oklahoma State University, Stillwater, Oklahoma.

Liang, F., Natarajan, B., Tian, Y., and Dougherty, R. L. (1995), "Local Efficiency Measurements Applicable to Both Automotive Engine and Cabin Filtration," *Particulate Science and Technology*, Taylor and Francis Publishers, Vol. 12, No. 4, April, pp. 333-350.

Löffler, I. F. (1970), "Separation Efficiency and Pressure Loss of Filter Materials of Different Structure, at Differing Conditions," *Staub-Reinhalt. Luft*, Vol. 30, No. 12, December, pp. 27-31.

McLaughlin, C., McComber, P., and Gakwaya, A. (1986), "Numerical Calculation of Particle Collection by a Row of Cylinders in a Viscous Fluid," *Canadian Journal of Chemical Engineering*, Vol. 64, April, pp. 205-210.

Natarajan, B. (1995), "Local Efficiency Measurements of Automotive Air Filters Using Laser Doppler Velocimetry," M. S. Thesis, School of Mechanical and Aerospace Engineering, Oklahoma State University, Stillwater, Oklahoma.

Natarajan, B., Liang, F., Williams, J. C., and Dougherty, R. L. (1995a), "Local Efficiency Measurements Flat Filter Media: Application to Automotive Cabin and Engine Air Filters," presented at the American Filtration and Separation Society Meeting, April 24-36, Nashville, Tennessee.

Natarajan, B., Williams, J. C., Tian, S. Y., Liang, F., and Dougherty, R. L. (1995b), "Local Efficiency Measurements of Pleated Panel Air Filter Used in Automotive Engines," AIAA/ASME Oklahoma Symposium XV, Oklahoma State University, Stillwater, OK., Feb.

Nicholson, R. M., and Weisert, L. E. (1986), "A Review of the Use of SAE Standard J726 in Heavy Duty Engine Air Cleaner Testing," *Fluid Filtration: Gas*, Vol. I, ASTM STP 975, American Society for Testing and Materials, Philadelphia, pp. 266-274.

Ptak, T. J., and Jaroszczyk, T. (1990), "Theoretical-Experimental Aerosol Filtration Model for Fibrous Filters at Intermediate Reynolds Numbers," Proceedings of the Fifth World Filtration Congress, Nice, France, pp. 566-572.

Ptak, T. J., Wake, J., and Jaroszczyk, T. (1994), "An Experimental Evaluation of the Factors Influencing the Performance of Car Interior Air Filters," SAE Technical Paper #930014, SAE, Inc., Warrendale, PA.

Reinhart, C. O., and Weisert, L. E. (1983), "Measurement of Engine Air Cleaner Efficiency Using Airborne Particle Size Analysis," SAE Technical Paper 831262, International Off-Highway Meeting and Exposition, Milwaukee, Wisconsin, Sept.

Rodman, C. A., and Lessmann, R. C. (1988), "Automotive Nonwoven Filter Media: Their Constructions and Filter Mechanisms," *Tappi Journal*, Apr., pp. 161-168.

Sabnis, R. D. (1993), "Effects of Non-Uniform Air Flow Through Filters on Filtration Efficiency," M. S. Thesis, School of Mechanical and Aerospace Engineering, Oklahoma State University, Stillwater, Oklahoma.

Sabnis, R. D., Cai, Q., and Chambers, F. W. (1994), "Diagnosis of the Flow Fields in a Housing for Automotive Air Filter Performance Testing," presented at the AIAA 32nd Aerospace Sciences Meeting, Jan. 10-13, Reno, Nevada.

Society of Automotive Engineers (1987), "SAE J726 Air Cleaner Test Code - SAE Recommended Practice," SAE, Inc., Warrendale, PA.

Society of Automotive Engineers (1993), "SAE J1669 Passenger Compartment Air Filter Test Code - SAE Recommended Practice," Proposed Draft, SAE, Inc., Warrendale, PA.

Stenhouse, J. I. T. (1975), "Filtration of Air by Fibrous Filters," *Filtration and Separation*, May/June, pp. 268-274.

Stinson, J. A., Meyers, M. N., Jaroszczyk, T., and Verdegan, B. M. (1989), "Temporal Changes in Oil and Air Filter Performance Due to Dust Deposition," *Filtration and Separation*, Sept./Oct., pp. 368-371.

Tebbutt, C. B. (1995), "CFD Model of Flow Through Air Filter Pleats," M. S. Thesis, School of Mechanical and Aerospace Engineering, Oklahoma State University, Stillwater, Oklahoma.

Tian, Y. (1995), "TSTEP - Three Dimensional Traverse Software," performed as part of the OCAST Applied Research Project on Automotive Air Filtration, Oklahoma State University, Stillwater, Oklahoma.

Wake, J., and Jaroszczyk, T. (1991), "Experimental Study of Dust Filtration in Surface-Type Nonwovens," *Particulate Science and Technology*, Vol. 9, Hemisphere Publishing Corporation, pp. 31-44.

Walker, M., and Ptak, T. J. (1996), "Particulate Filter Performance in the North American Environment," SAE Technical Paper #960940, Aspects of Automotive Filtration (SP-1165), SAE, Inc., Warrendale, PA.

Williams, J. C. (1996), "In-Situ Measurements of Local Efficiency for Flat Automotive Air Filter Media," M. S. Report, School of Mechanical and Aerospace Engineering, Oklahoma State University, Stillwater, Oklahoma.

Yeh, H. C. (1972), "A Fundamental Study of Aerosol Filtration by Fibrous Filters," Ph.D. Thesis, University of Minnesota, Minnesota, March.

Yeh, H. C., and Liu, B. Y. H. (1974), "Aerosol Filtration by Fibrous Filters - I. Theoretical," *Aerosol Science*, Vol. 5, Pergamon Press, Great Britain, pp. 191-204.

APPENDIXES

APPENDIX A

LIST OF EQUIPMENT

1. Watt Argon Ion laser: Coherent, Model Innova 70-A, Serial No. P/S 92K-1758
2. Remote control for the laser: Coherent, Model I-70, Serial No. 92411171
3. Fiber drive: Aerometrics, Inc., Model FBD1240, Serial No. 026
4. Bragg cell: IntraAction, Inc., Model ME-40H, Serial No. 3247
5. Photomultiplier Tubes: Aerometrics, Inc., Model RCM2200L, Serial No. 029
6. Doppler Signal Analyzer: Aerometrics, Inc., Model DSA3220, Serial No. 044
7. Computer and Monitor: Impression 3, IBM compatible 80486 DX2, 66 MHz
8. Computer for Traverse System and MS-Excel Data Acquisition Files: Gateway 2000, IBM compatible, 80486 DX2, 33 MHz
9. Laser Transceiver: Aerometrics, Inc., Model XRV1212, Serial No. 001
10. Three Stepper Motors (Sanyo Denki, Type: 103-850-11)
11. Oscilloscope: Hewlett Packard, Model 54501A
12. Plexiglas Test Housings: SAE J1669 Small Angle Diffuser Housing
13. Pleated Test Filter: Purolator, Inc., A13192 (formerly AF3192)
14. TSI Mass Flow Sensor: TSI, Model 2018, Serial No. 30644

15. Atomizer: TSI Model 9306, six-jet atomizer
16. SAE J726 Air Stand, Purolator Products, Inc.
17. Rival Compact Heater, Model T114
18. Stepper Motor Drives, Model CMD-40
19. 24 V DC - 6 A Power Supply (Acme Electronics)
20. Connector 3 for Digital Output, Model PCLD-780
21. Ultrasonic Humidifier: Pollenex, Model SH55R

APPENDIX B

SWEPT VOLUME TECHNIQUE

The Swept Volume Technique was developed by Liang [1997] to determine the number density value from the number of particles counted (N_i), their average measured velocity (v_i), the length of time taken to count these particles, and the area of the probe (A) swept to form the volume. The method assumes that all of the particles crossing the probe volume have a velocity equal to the average velocity of all samples measured at a location. Thus, number density is given as

$$n_i = \frac{N_i}{v_i t_i A} \quad (\text{B-1})$$

The probe area is $3.2 \times 10^{-11} \text{ m}^2$ [Liang, 1997]. Figure B-1 shows the concept of swept volume.

This technique has been shown to fail at very low velocities [Jadbabaei, 1997]. A look at Eq. (B-1) indicates that, for very low velocities like those measured near the walls of the housing, the number density tends to an erroneously large value. Jadbabaei [1997] explains this observation from a physical point of view and discusses a number of different modifications to overcome this difficulty. Jadbabaei [1997] indicates that in regions where there is a recirculating flow, the average velocity of the particles is close to zero, but the velocity distribution is comprised of both positive and negative velocity values. This

technique assumes that the velocity is unidirectional, which is not the case in many situations (for example a recirculating flow). Jadbabaei [1997] suggests the use of root mean squared velocity or absolute value average velocity but is unable to justify their use. For the present study, the flow field was uniform in the measurement grid which justifies the use of the swept volume technique.

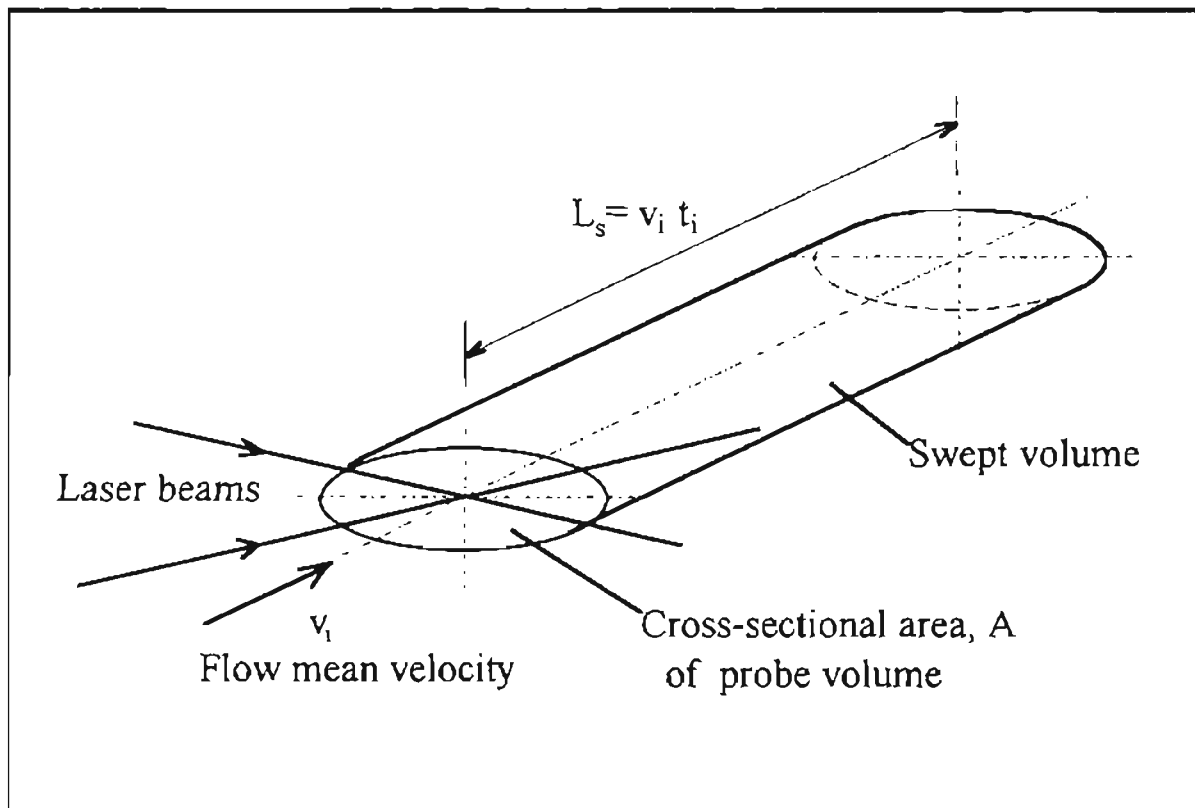


Figure B-1 Swept Volume Technique [Liang, 1997].

APPENDIX C

TSI FLOW METER CALIBRATION

The flow rate was monitored in the present study using a TSI Model 2018 flow meter. To ensure that the flow rate measurements made by the flow meter were accurate, the flow meter was calibrated. The calibration procedure involved the use of a 1” diameter ASME flow nozzle. The flow nozzle (at flow inlet) and the TSI flow meter were connected in series to the Purolator test stand blower so that the same flow passed through both of them. An inclined manometer and a pressure transducer were connected across the flow nozzle to measure pressure drop across the nozzle and hence determine the flow through it. The pressure transducer was connected to a computer for data acquisition purposes. Corrections for temperature and atmospheric pressure were also incorporated into the calibration process. The pressure drop values measured by the manometer and the pressure transducer along with the flow rates indicated by the TSI flow meter were recorded at a number of points by varying the flow rate from the test stand. The results are presented in Fig. C-1.

The ideal mass flow rate was calculated on the assumption of isentropic flow as

$$\dot{m}_{ideal} = \frac{A_2 p_1}{T_1^{1/\gamma}} \left\{ \left(\frac{p_2}{p_1} \right)^{1/\gamma} \left[1 - \left(\frac{p_2}{p_1} \right)^{(\gamma-1)/\gamma} \right] \right\}^{1/2} \left[\left(\frac{1}{R} \right) \left(\frac{2\gamma}{\gamma-1} \right) \right]^{1/2} \quad (C-1)$$

where A_2 is the throat area, p_2 is the throat static pressure, p_1 is the total pressure, T_1 is the total temperature, γ is the ratio of specific heats and R is gas constant. An initial value of the discharge coefficient, C_d was assumed and the actual volumetric flow rate calculated as

$$Q_{actual} = \frac{C_d \dot{m}_{ideal}}{\rho} \quad (C-2)$$

where ρ is the density of air. Since the nozzle diameter is known, the Reynolds number can be calculated. From the Reynolds number the new value of C_d is calculated using an empirical relation. One such relation given by Benedict [1984] is

$$C_d = 0.19436 + 0.152884(\ln Re) + 0.0097785(\ln Re)^2 + 0.00020903(\ln Re)^3 \quad (C-3)$$

This was compared with the assumed value of C_d and iterated until the solution converged. The converged value of C_d was used to obtain the actual flow rate (Q_{nozzle} in Fig. C-1).

The TSI indicates flow rates which are linearly related to those measured by the flow nozzle but shows an offset of about 1.418 cfm. Thus, the TSI flow meter indicates flow rates slightly higher than those measured by the flow nozzle. This would cause the results of the present study to shift by a very small amount to the lower Stokes number (or flow rate) side. The overall results presented in Chapter 5 have been modified in accordance with this calibration.

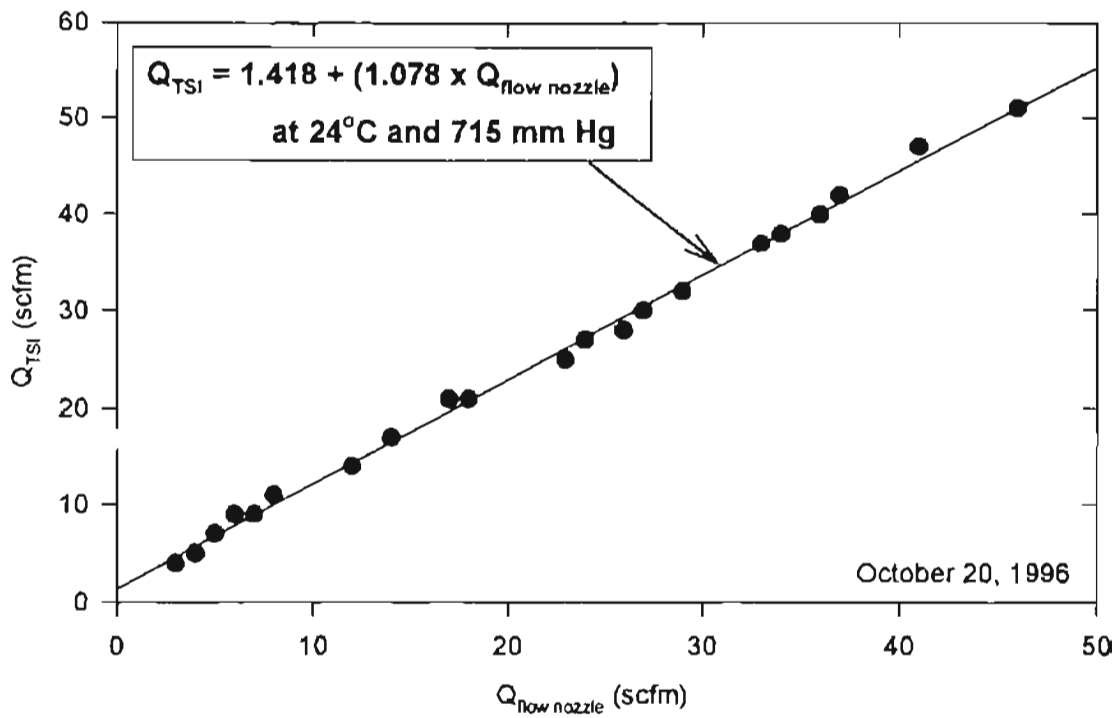


Figure C-1 Results of the TSI Flow Meter Calibration.

APPENDIX D

OTHER RESULTS

Some of the test results have been shown and discussed in Chapter 5. The other test results are presented in this appendix. The results presented here are the upstream and downstream local velocity measurements, the upstream and downstream local number densities, and the local efficiencies for each of the tests. The velocities, number densities, and efficiencies have been arranged in ascending order of flow rates. The figures have been reduced in size in an attempt to save space. Tests FLT13 and FLT21 are special in that they had repeated downstream measurements over the same filter used in tests FLT12 and FLT20. Hence, they do not have independent upstream velocity and number density plots.

The data for all the plots presented here can be found on the Gateway 2000 computer in the Purolator laboratory under FLT series files in the c:\users\flt directory. The FLT series files are classified as FLTUP[test number] and FLTDWN[test number] for upstream and downstream plane measurements. The calculated efficiencies can also be found in the upstream plane files.

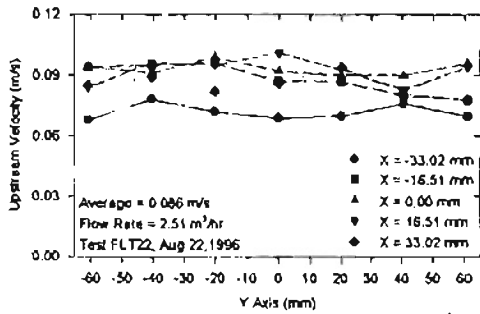


Figure D-1: Local Upstream Velocity (2.51 m³/hr, FLT22)

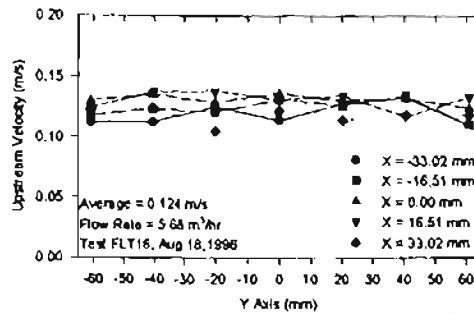


Figure D-2: Local Upstream Velocity (5.68 m³/hr, FLT16)

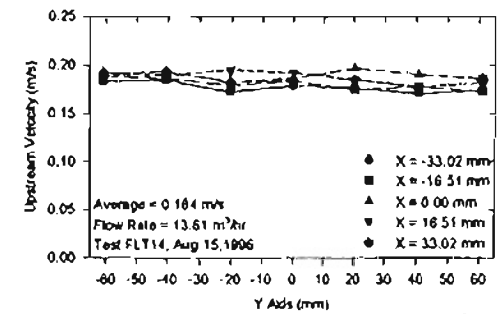


Figure D-3: Local Upstream Velocity (13.61 m³/hr, FLT14)

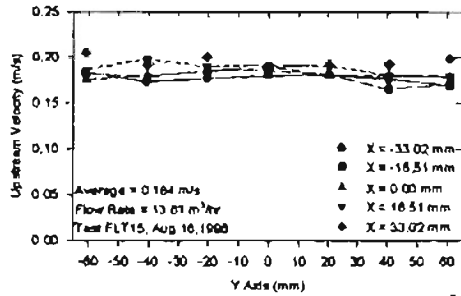


Figure D-4: Local Upstream Velocity (13.61 m³/hr, FLT15)

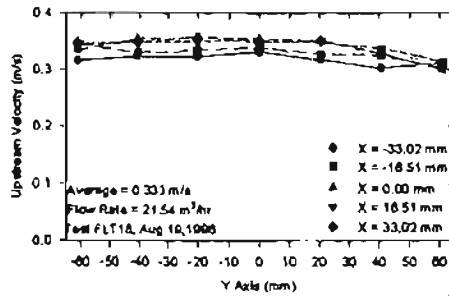


Figure D-5: Local Upstream Velocity (21.54 m³/hr, FLT18)

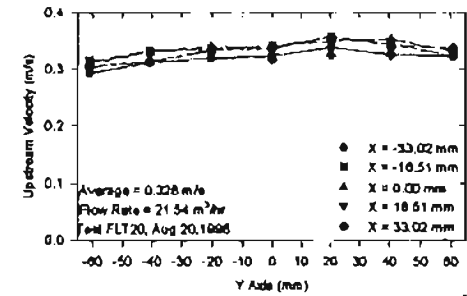


Figure D-6: Local Upstream Velocity (21.54 m³/hr, FLT20 and FLT21)

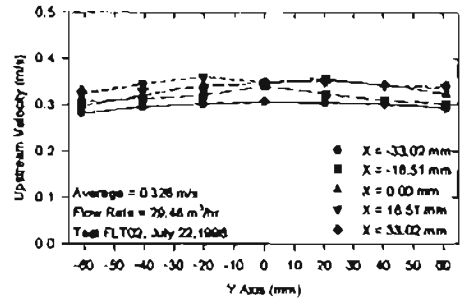


Figure D-7: Local Upstream Velocity (29.48 m³/hr, FLT02)

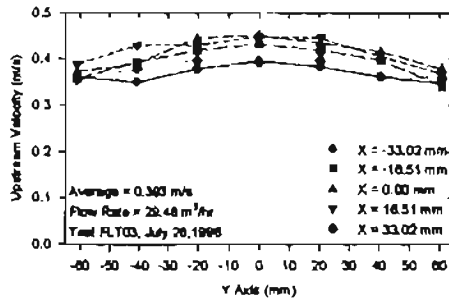


Figure D-8: Local Upstream Velocity (29.48 m³/hr, FLT03)

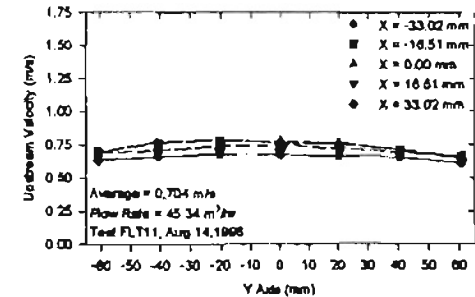


Figure D-9: Local Upstream Velocity (45.34 m³/hr, FLT11)

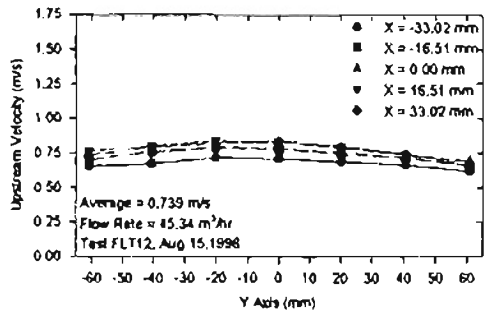


Figure D-10: Local Upstream Velocity ($45.34 \text{ m}^3/\text{hr}$, FLT12 and FLT13)

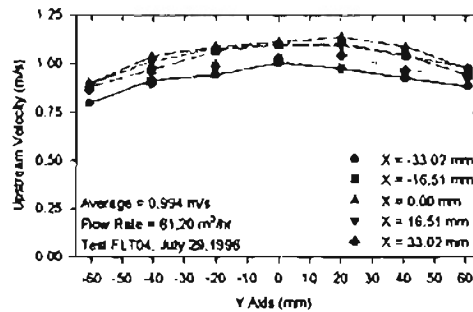


Figure D-11: Local Upstream Velocity ($61.20 \text{ m}^3/\text{hr}$, FLT04)

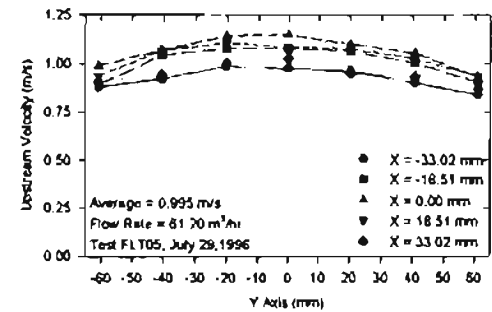


Figure D-12: Local Upstream Velocity ($61.20 \text{ m}^3/\text{hr}$, FLT05)

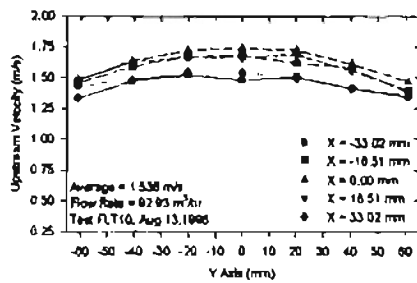


Figure D-13: Local Upstream Velocity ($92.93 \text{ m}^3/\text{hr}$, FLT10)

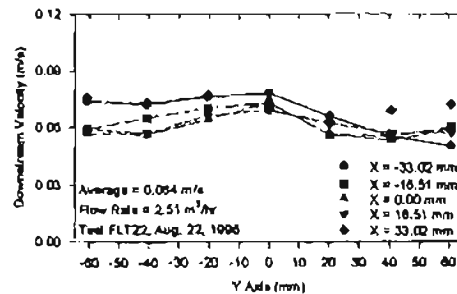


Figure D-14: Local Downstream Velocity ($2.51 \text{ m}^3/\text{hr}$, FLT22)

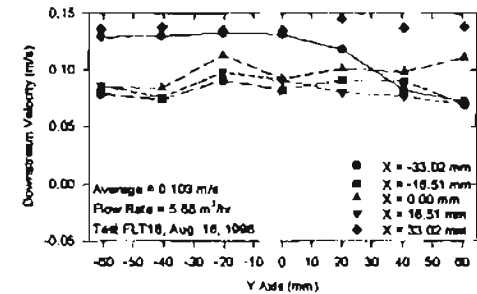


Figure D-15: Local Downstream Velocity ($5.68 \text{ m}^3/\text{hr}$, FLT16)

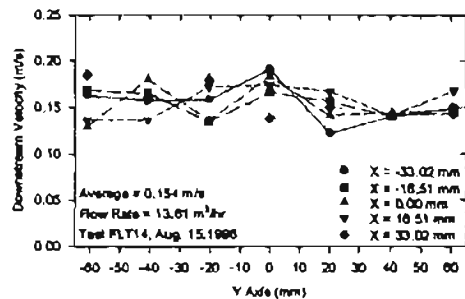


Figure D-16: Local Downstream Velocity ($13.61 \text{ m}^3/\text{hr}$, FLT14)

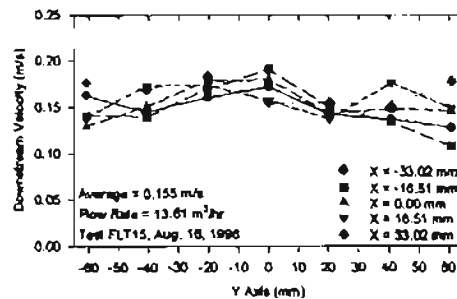


Figure D-17: Local Downstream Velocity ($13.61 \text{ m}^3/\text{hr}$, FLT15)

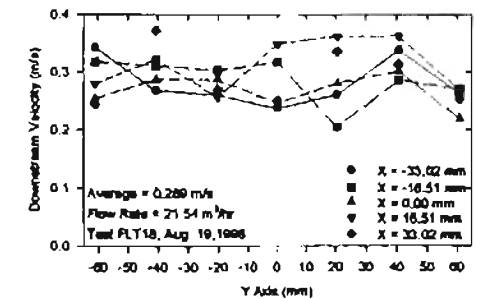


Figure D-18: Local Downstream Velocity ($21.54 \text{ m}^3/\text{hr}$, FLT18)

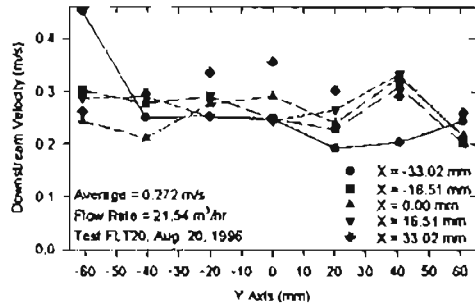


Figure D-19: Local Downstream Velocity (21.54 m³/hr, FLT20)

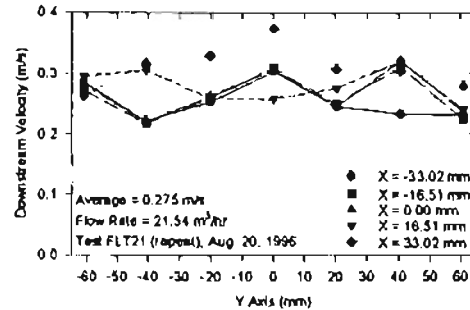


Figure D-20: Local Downstream Velocity (21.54 m³/hr, FLT21)

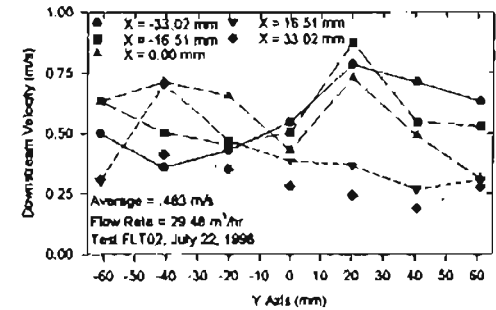


Figure D-21: Local Downstream Velocity (29.48 m³/hr, FLT02)

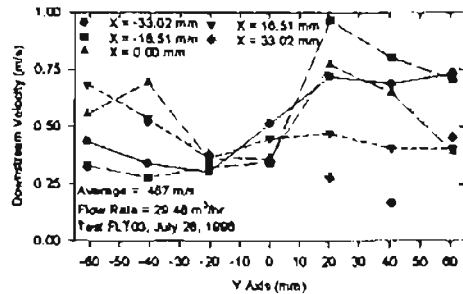


Figure D-22: Local Downstream Velocity (29.48 m³/hr, FLT03)

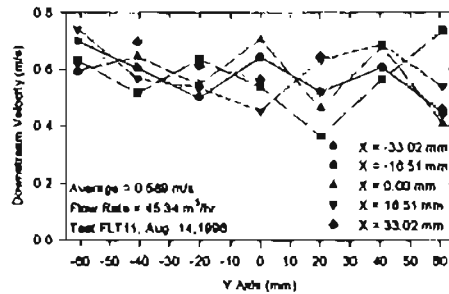


Figure D-23: Local Downstream Velocity (45.34 m³/hr, FLT11)

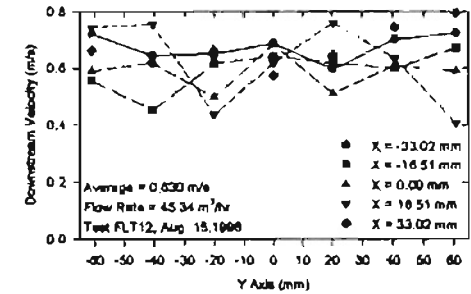


Figure D-24: Local Downstream Velocity (45.34 m³/hr, FLT12)

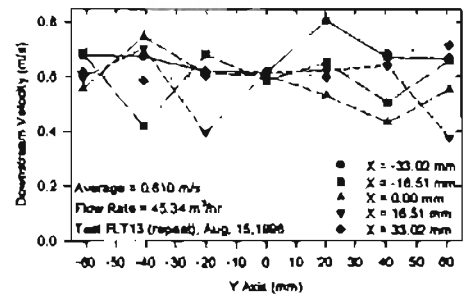


Figure D-25: Local Downstream Velocity (45.34 m³/hr, FLT13)

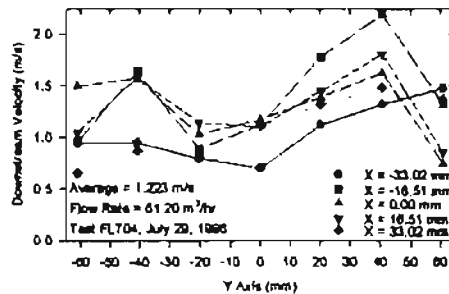


Figure D-26: Local Downstream Velocity (61.20 m³/hr, FLT04)

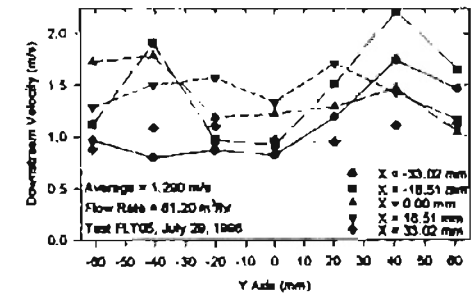


Figure D-27: Local Downstream Velocity (61.20 m³/hr, FLT05)

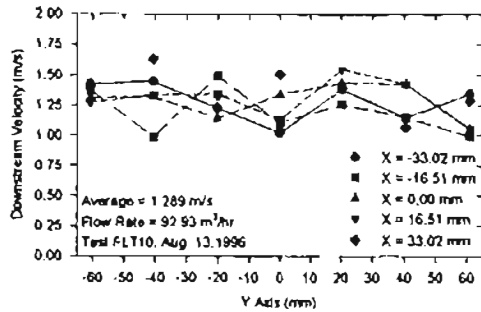


Figure D-28: Local Downstream Velocity (92.93 m³/hr, FLT10).

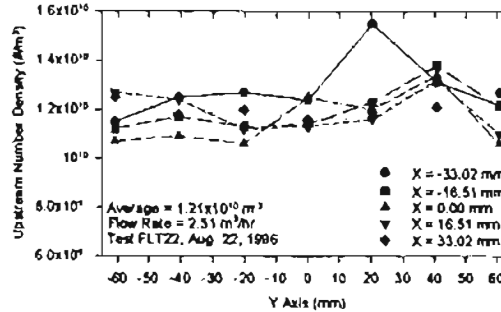


Figure D-29: Local Upstream Number Density (2.51 m³/hr, FLT22).

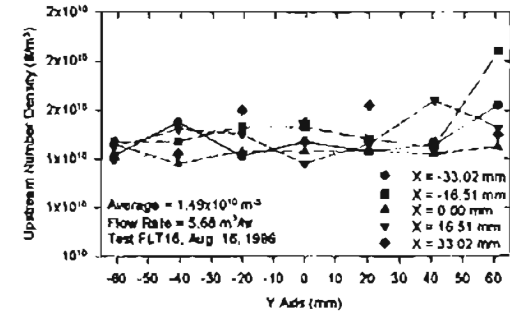


Figure D-30: Local Upstream Number Density (5.68 m³/hr, FLT16).

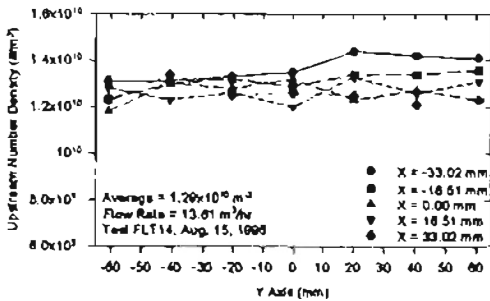


Figure D-31: Local Upstream Number Density (13.61 m³/hr, FLT14).

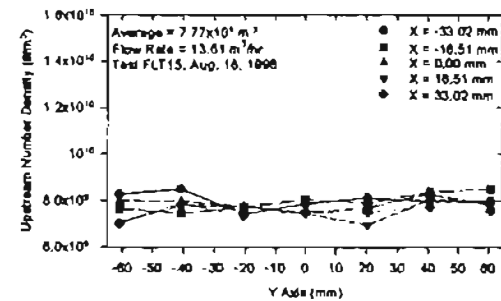


Figure D-32: Local Upstream Number Density (13.61 m³/hr, FLT15).

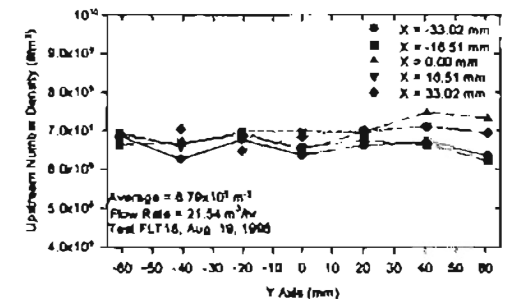


Figure D-33: Local Upstream Number Density (21.54 m³/hr, FLT18).

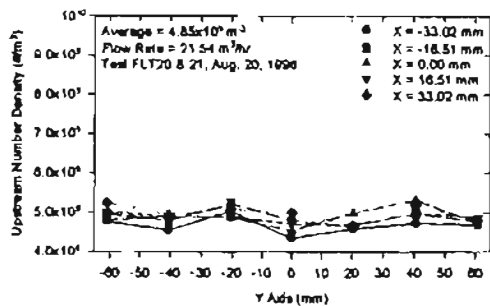


Figure D-34: Local Upstream Number Density (21.54 m³/hr, FLT20 and FLT21).

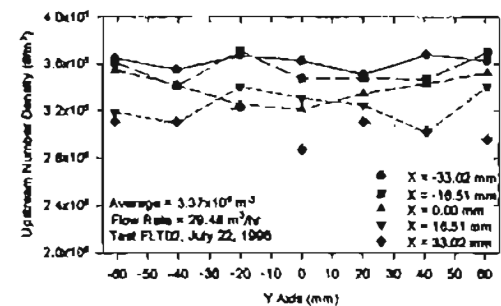


Figure D-35: Local Upstream Number Density (29.48 m³/hr, FLT02).

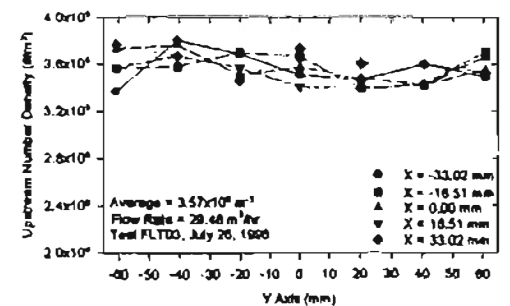


Figure D-36: Local Upstream Number Density (29.48 m³/hr, FLT03).

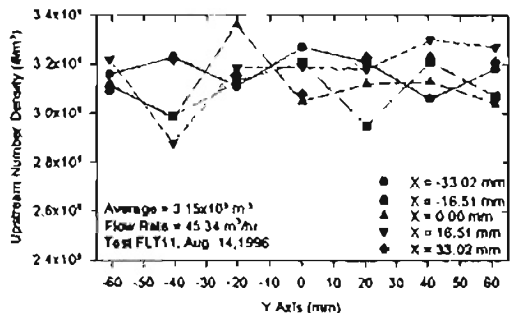


Figure D-37: Local Upstream Number Density ($45.34 \text{ m}^3/\text{hr}$, FLT11).

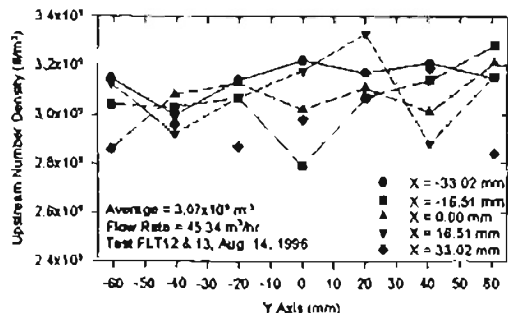


Figure D-38: Local Upstream Number Density ($45.34 \text{ m}^3/\text{hr}$, FLT12 and FLT13).

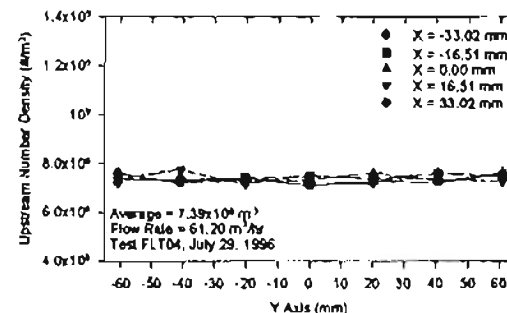


Figure D-39: Local Upstream Number Density ($61.20 \text{ m}^3/\text{hr}$, FLT04).

FLT

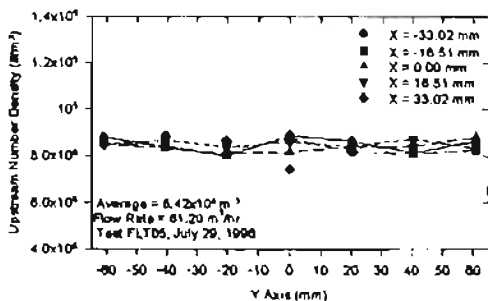


Figure D-40: Local Upstream Number Density ($61.20 \text{ m}^3/\text{hr}$, FLT05).

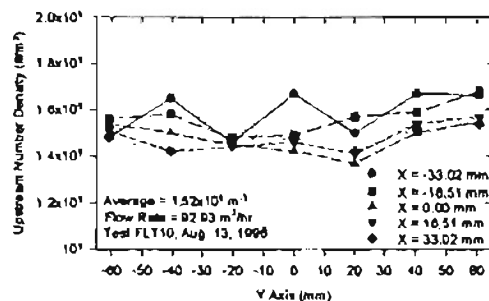


Figure D-41: Local Upstream Number Density ($92.93 \text{ m}^3/\text{hr}$, FLT10).

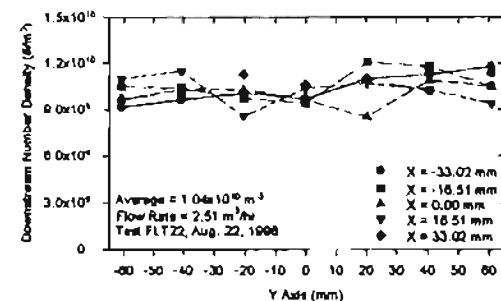


Figure D-42: Local Downstream Number Density ($2.51 \text{ m}^3/\text{hr}$, FLT22).

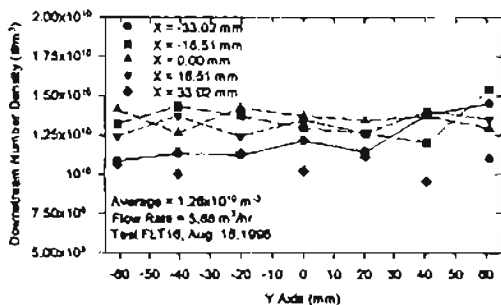


Figure D-43: Local Downstream Number Density ($5.68 \text{ m}^3/\text{hr}$, FLT16).

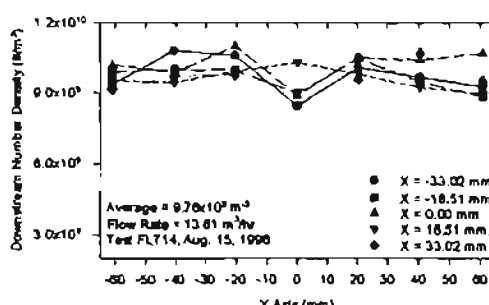


Figure D-44: Local Downstream Number Density ($13.61 \text{ m}^3/\text{hr}$, FLT14).

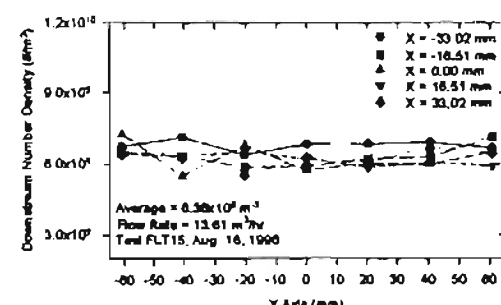


Figure D-45: Local Downstream Number Density ($13.61 \text{ m}^3/\text{hr}$, FLT15).

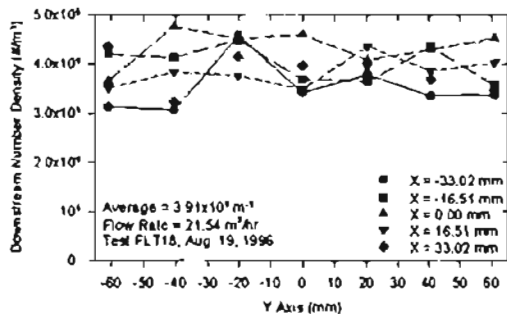


Figure D-46: Local Downstream Number Density ($21.54 \text{ m}^3/\text{hr}$, FLT18).

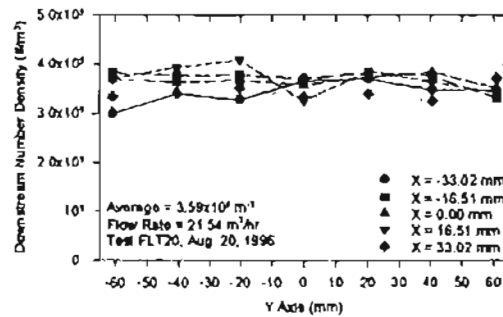


Figure D-47: Local Downstream Number Density ($21.54 \text{ m}^3/\text{hr}$, FLT20).

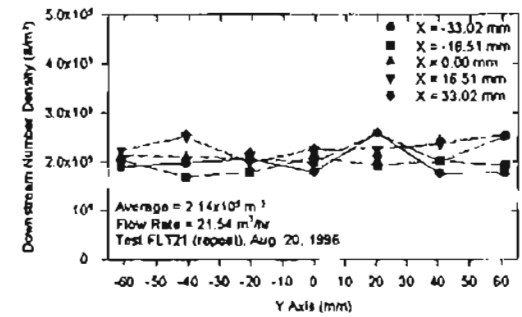


Figure D-48: Local Downstream Number Density ($21.54 \text{ m}^3/\text{hr}$, FLT21).

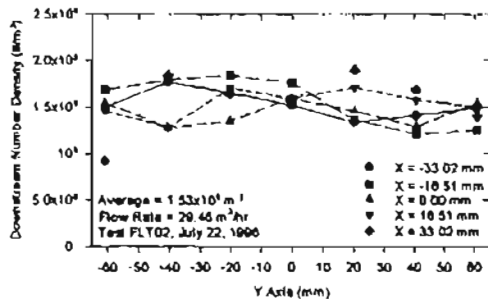


Figure D-49: Local Downstream Number Density ($29.48 \text{ m}^3/\text{hr}$, FLT02).

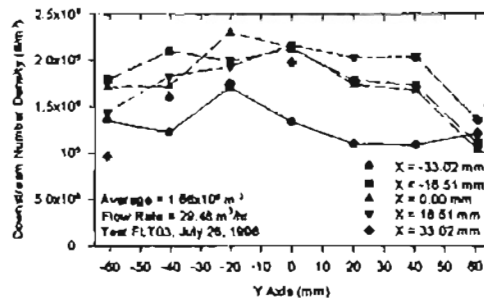


Figure D-50: Local Downstream Number Density ($29.48 \text{ m}^3/\text{hr}$, FLT03).

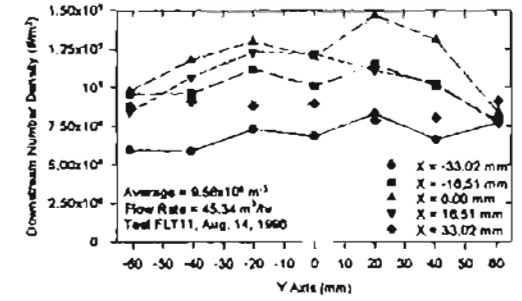


Figure D-51: Local Downstream Number Density ($45.34 \text{ m}^3/\text{hr}$, FLT11).

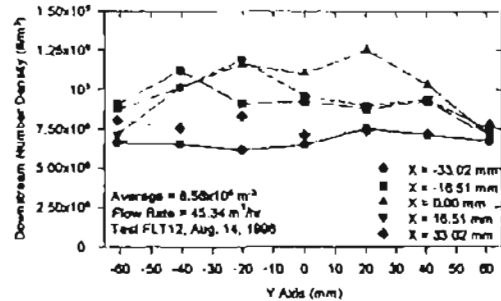


Figure D-52: Local Downstream Number Density ($45.34 \text{ m}^3/\text{hr}$, FLT12).

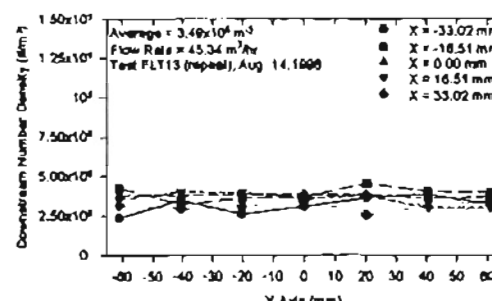


Figure D-53: Local Downstream Number Density ($45.34 \text{ m}^3/\text{hr}$, FLT13).

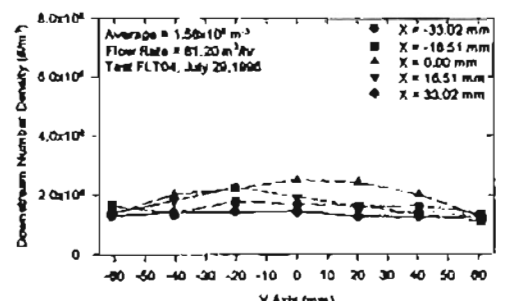


Figure D-54: Local Downstream Number Density ($61.20 \text{ m}^3/\text{hr}$, FLT04).

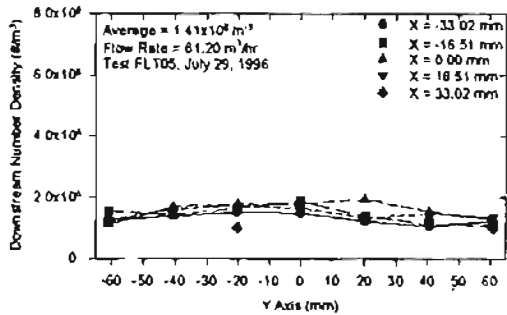


Figure D-55: Local Downstream Number Density (61.20 m³/hr, FLT05).

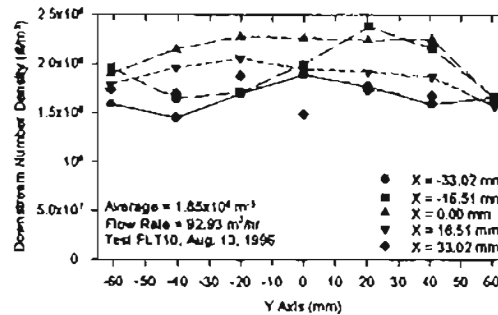


Figure D-56: Local Downstream Number Density (92.93 m³/hr, FLT10).

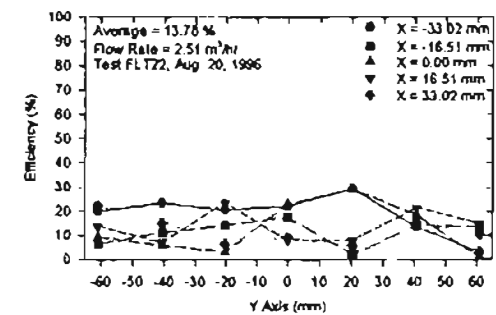


Figure D-57: Local Filtration Efficiency (2.51 m³/hr, FLT22).

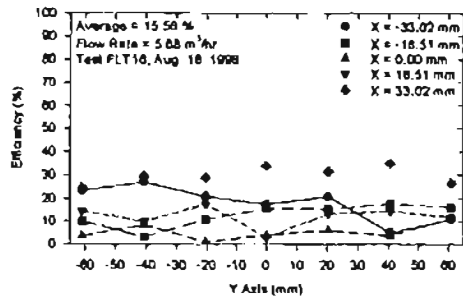


Figure D-58: Local Filtration Efficiency (5.68 m³/hr, FLT16).

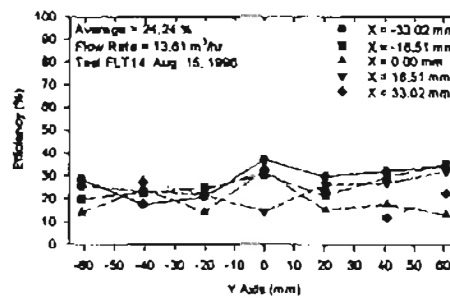


Figure D-59: Local Filtration Efficiency (13.61 m³/hr, FLT14).

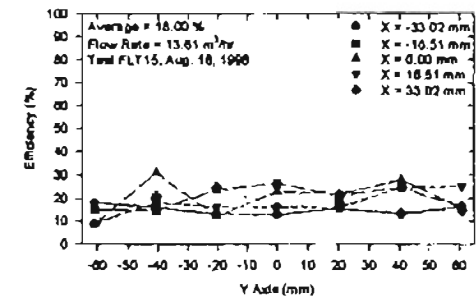


Figure D-60: Local Filtration Efficiency (13.61 m³/hr, FLT15).

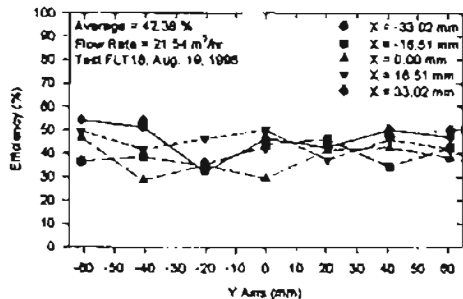


Figure D-61: Local Filtration Efficiency (21.54 m³/hr, FLT18).

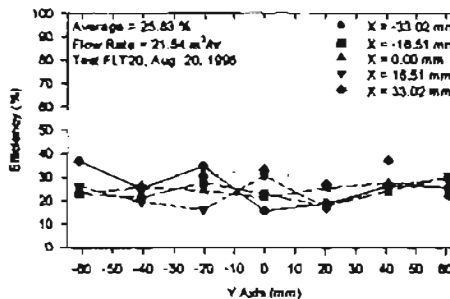


Figure D-62: Local Filtration Efficiency (21.54 m³/hr, FLT20).

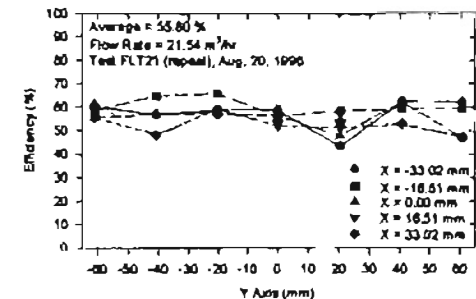


Figure D-63: Local Filtration Efficiency (21.54 m³/hr, FLT21).

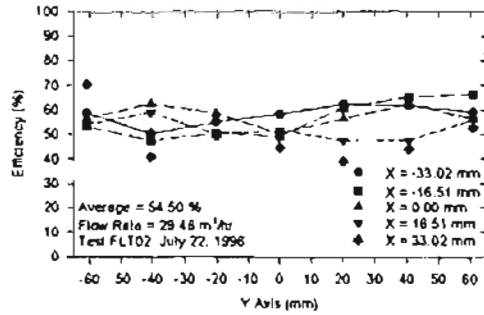


Figure D-64: Local Filtration Efficiency (29.48 m³/hr, FLT02).

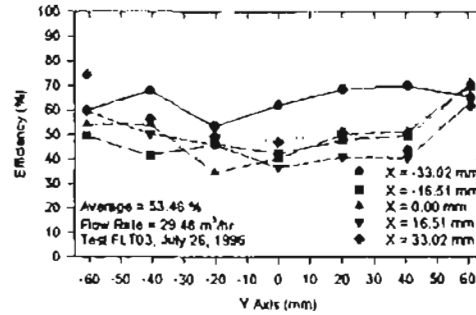


Figure D-65: Local Filtration Efficiency (29.48 m³/hr, FLT03).

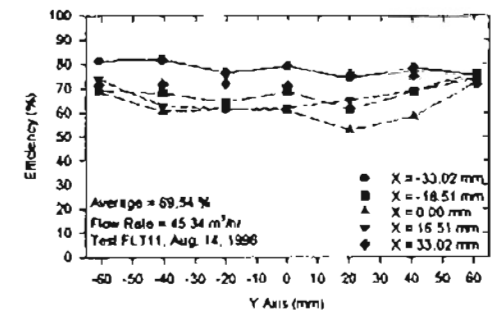


Figure D-66: Local Filtration Efficiency (45.34 m³/hr, FLT11).

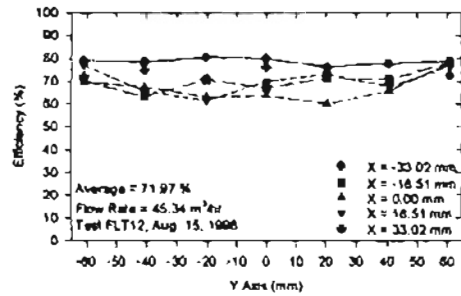


Figure D-67: Local Filtration Efficiency (45.34 m³/hr, FLT12).

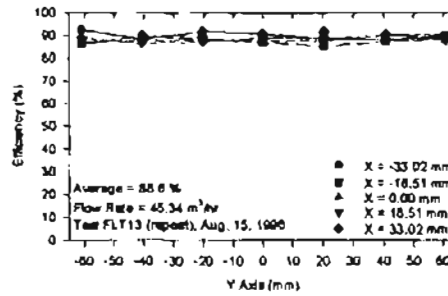


Figure D-68: Local Filtration Efficiency (45.34 m³/hr, FLT13).

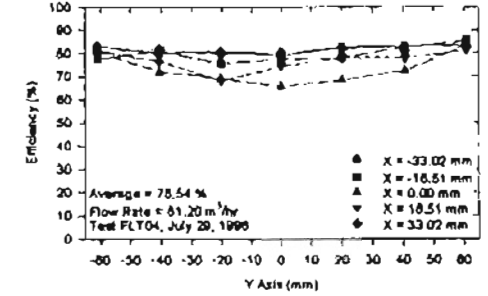


Figure D-69: Local Filtration Efficiency (61.20 m³/hr, FLT04).

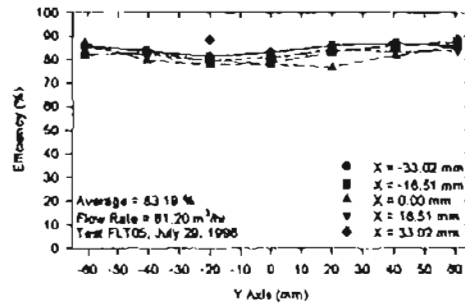


Figure D-70: Local Filtration Efficiency (61.20 m³/hr, FLT05).

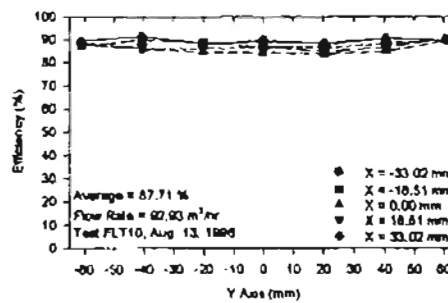


Figure D-71: Local Filtration Efficiency (92.93 m³/hr, FLT10).

APPENDIX E

ERROR ANALYSIS

The error in efficiency explained in section 4.2 is based on a simple analysis considering the worst errors in number density values. A more sophisticated approach to this error analysis can be obtained from Kline and McClintock [1953]. It is based on the assumption of a random error in number density measurements. A brief description of this analysis is provided next.

The efficiency as defined in Eq. (3-1) is given by

$$\eta = 1 - \frac{n_d}{n_u} \quad (\text{E-1})$$

where n_d and n_u are the downstream and upstream number densities. If e_u and e_d were the variations (not fractional but actual) in the upstream and downstream number densities, then the error in efficiency is given by

$$\frac{d\eta}{\eta} = \left[\left(\frac{\partial \eta}{\partial n_u} e_u \right)^2 + \left(\frac{\partial \eta}{\partial n_d} e_d \right)^2 \right]^{1/2} = \left[\left(\frac{n_d}{n_u^2} e_u \right)^2 + \left(-\frac{1}{n_u} e_d \right)^2 \right]^{1/2} \quad (\text{E-2})$$

$$\frac{d\eta}{\eta} = \left\{ \left[\left(\frac{n_d}{n_u} \right) \left(\frac{e_u}{n_u} \right) \right]^2 + \left[- \left(\frac{n_d}{n_u} \right) \left(\frac{e_d}{n_d} \right) \right]^2 \right\}^{1/2} \quad (\text{E-3})$$

where e_u/n_u and e_d/n_d are the fractional error values in the upstream and downstream number densities. If these errors were the same and equal to a constant (say c_e), then

$$\frac{d\eta}{\eta} = \frac{n_d}{n_u} \left[(c_e)^2 + (c_e)^2 \right]^{1/2} = \sqrt{2}(c_e)R_{nd} \quad (\text{E-4})$$

would give the error in the efficiency.

Number density is determined from Eq. (3-2) as

$$n = \frac{N}{v t A} \quad (\text{E-5})$$

The error in number density due to errors in N , v , t and A can be determined as

$$\frac{dn}{n} = \frac{1}{n} \left[\left(\frac{\partial n}{\partial N} dN \right)^2 + \left(\frac{\partial n}{\partial v} dv \right)^2 + \left(\frac{\partial n}{\partial t} dt \right)^2 + \left(\frac{\partial n}{\partial A} dA \right)^2 \right]^{1/2} \quad (\text{E-6})$$

$$\frac{dn}{n} = \left[\left(\frac{dN}{N} \right)^2 + \left(-\frac{dv}{v} \right)^2 + \left(-\frac{dt}{t} \right)^2 + \left(-\frac{dA}{A} \right)^2 \right]^{1/2} \quad (\text{E-7})$$

If the errors in N , v , t and A were 5%, 2%, 2% and 2% (errors for N , v , t were observed while making experimental measurements while the error for A is assumed as a reasonable value for the LDV system), then the error in number density would be

$$\frac{dn}{n} = \left[(0.05)^2 + (-0.02)^2 + (-0.02)^2 + (-0.02)^2 \right]^{1/2} = 0.0608 \text{ or } 6.08\% \quad (\text{E-8})$$

If this error was used in Eq. (E-4), then the error in efficiency would be

$$\frac{d\eta}{\eta} = (0.0860)R_{nd} \quad (\text{E-9})$$

Thus, errors of 5%, 2%, 2% and 2% in number count, velocity, time and probe cross-sectional area would result in an efficiency error as given by Eq. (E-9).

APPENDIX F

PRESSURE DROP AND EFFICIENCY PLOTS

Figure F-1 compares the pressure drop in the present study with that of the experimental pressure drop obtained by Tebbutt [1995] for the same media but in a different setup. Tebbutt [1995] measured the pressure drop immediately across the filter media while, for the present study, the pressure drop was measured across the housing, thereby including the pressure drop due to the housing. The comparison is reasonable at the lower flow rates but deviates significantly at the higher flow rates. Figure F-2 plots all of the 35 local efficiency measurements for four different flow rates versus the average upstream velocity. The plot shows that the local measurements follow a trend similar to that shown in Fig. 5.19.

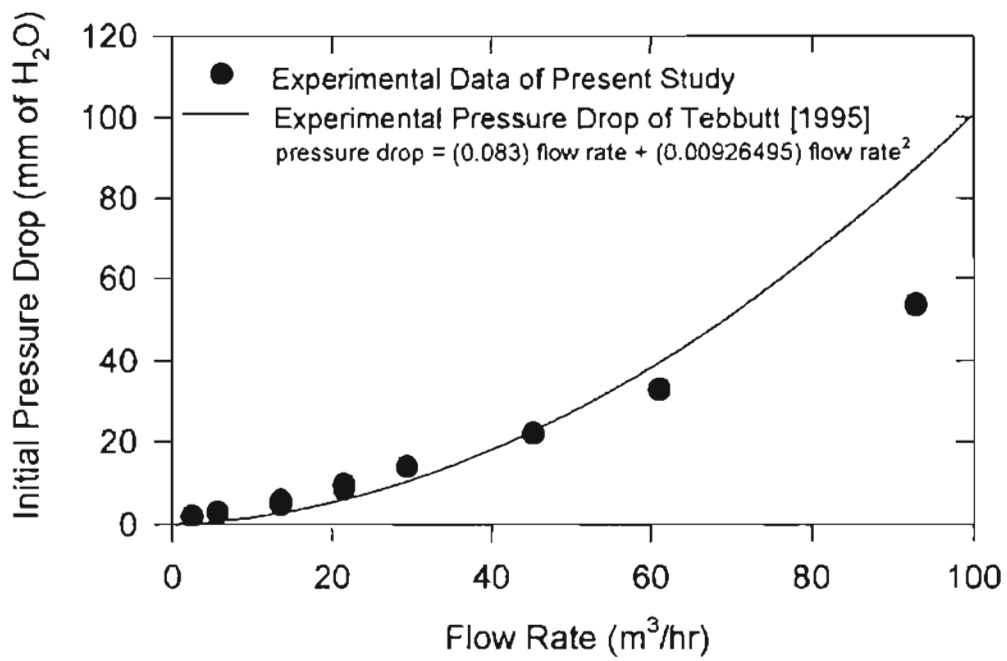


Figure F-1 Comparison of Pressure Drop with Tebbutt [1995].

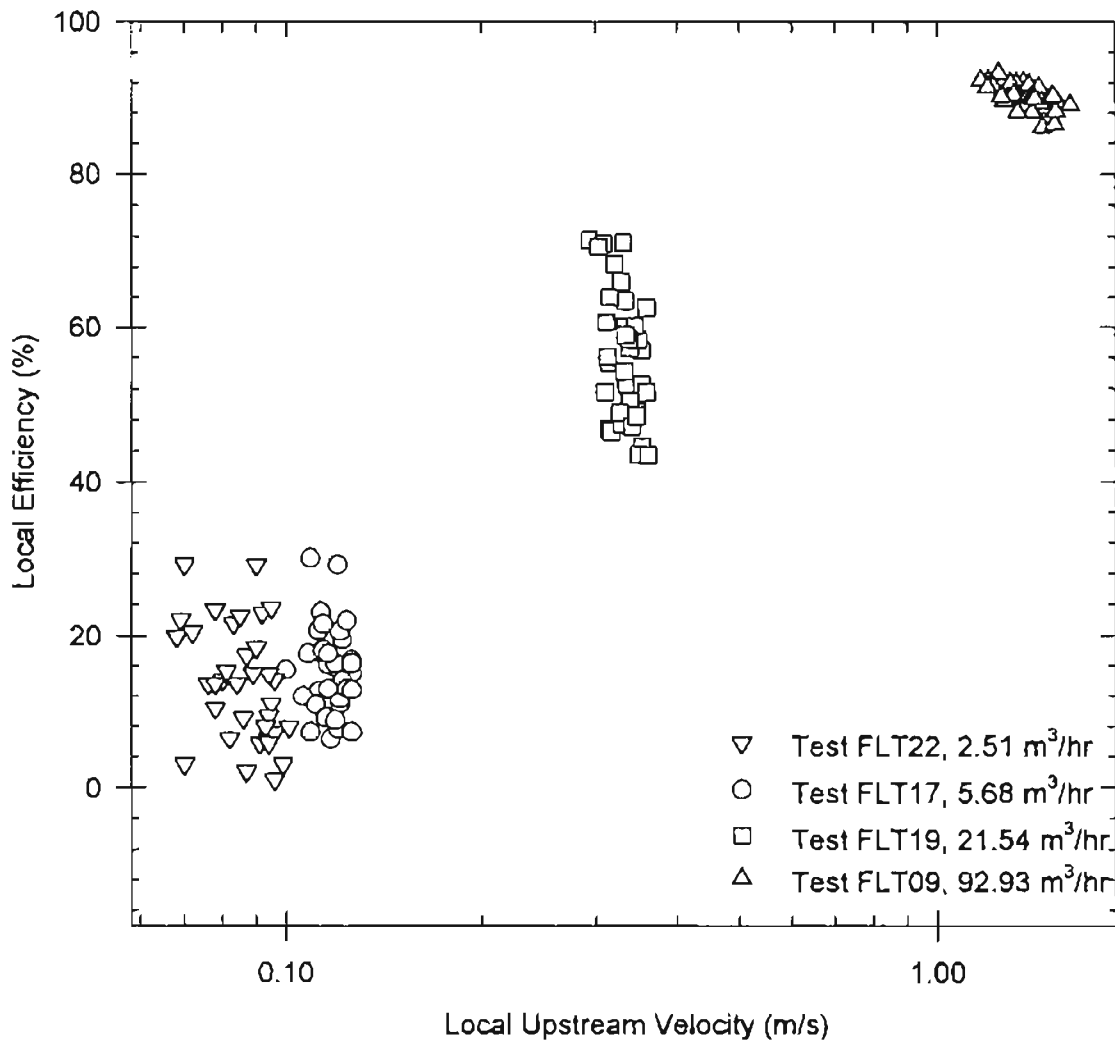


Figure F-2 Local Efficiency vs. Local Velocity Plot.

VITA

Sachin Anand

Candidate for the Degree of
Master of Science

Thesis: FILTRATION EFFICIENCY MEASUREMENTS ON FLAT SHEET FILTERS.

Major Field: Mechanical Engineering.

Biographical:

Personal Data: Born in Amritsar, Punjab, India, on October 25, 1972, the son of Vijay Kumar and Sharda Anand.

Educational: Graduated from Delhi Public School, New Delhi, India in April 1990; received Bachelor of Engineering degree in Mechanical Engineering from Delhi College of Engineering, Delhi, India in June 1994. Completed the requirements for the Master of Science degree with a major in Mechanical Engineering at Oklahoma State University in December 1996.

Experience: Employed by Oklahoma State University as a graduate research assistant from August 1995 to October 1996 and as a graduate teaching assistant during Spring 1995; worked as an intern with Dyna Aircon Limited from December 1993 to June 1994 and as a summer intern with Tata Engineering and Locomotive Company from June 1993 to August 1993.

Professional Memberships: Student Member, American Society of Mechanical Engineers.